MASTER'S THESIS

Estimating the relative density in calcareous sands with the Karlsruhe Interpretation Method

Author
Johannes Reinisch, BSc.

Supervisors
Ass.Prof. Dipl.-Ing. Dr.techn. Franz Tschuchnigg
Dipl.-Ing. Dr.techn. Robert Thurner

15. Januar 2018

Declaration of Authorship

I, Johannes Reinisch, declare that this thesis titled, "Estimating the relative density in calcareous sand with the Karlsruhe Interpretation Method" and the work presented in it are my own. I confirm that:

- This work was done wholly or mainly while in candidature for a research degree at this University.
- Where any part of this thesis has previously been submitted for a degree or any other qualification at this University or any other institution, this has been clearly stated.
- Where I have consulted the published work of others, this is always clearly attributed.
- Where I have quoted from the work of others, the source is always given. With the exception of such quotations, this thesis is entirely my own work.
- I have acknowledged all main sources of help.
- Where the thesis is based on work done by myself jointly with others, I have made clear exactly what was done by others and what I have contributed myself.

Signed:

Date:

"*This thesis is proof that raising your hand in the right moment can change your life.*"

Abstract

Johannes Reinisch

Estimating the relative density in calcareous sand with the Karlsruhe Interpretation Method

The thesis at hand describes the challenges that arise during quality control of deep vibro-compaction works on land reclamation projects realized in the Middle East. The aim of deep vibro-compaction is to densify the fill to a certain relative density and thereby assure certain minimal criteria related to the soil behavior such as stiffness and resistance against liquefaction. For quality control of the compaction works, the achieved relative density throughout the hydraulic fill can be measured indirectly by performing Cone Penetration Tests (CPT). The targeted relative density is linked to a cone resistance curve calculated with well-known and established correlation methods like Schmertmann or Baldi.

In the Middle East, deposits of carbonate sands consisting of varying amounts of fragmented sea-shells and corals are widely-spread and often dredged from the seabed to be used as hydraulic fill material for reclamation projects. Due to their mineralogy and grain shape, these sands often show a high tendency towards grain crushing. Therefore, commonly used empirical correlations between the cone resistance q_c and the relative density D_r are no longer valid because carbonate sands produce significantly lower q_c-values than silica sands under similar conditions. This can lead to unattainable target q_c-values demanded by the client requiring the contractor to re-compact even though in reality the soil has already been compacted to the required relative density.

In sands that contain a high carbonate content, an alternative to applying traditional correlation methods to derive the q_c-requirement is the use of the semi-empirical Karlsruhe Interpretation Method (KIM). This thesis explains the general procedure when applying the KIM from the required laboratory tests, the calibration of the hypoplastic model to the spherical cavity expansion simulations with a focus on the specific characteristics of carbonate sands. It is shown that the carbonate content of the soil influences the soil properties significantly and it is further discussed how the results obtained with the KIM are affected by an increasing carbonate content. Finally a case study of the application of the KIM on a land reclamation project in the UAE is presented.

Zusammenfassung

Johannes Reinisch

Estimating the relative density in calcareous sand with the Karlsruhe Interpretation Method

Die vorliegende Masterarbeit beschreibt die Schwierigkeiten in der Qualitätskontrolle von Rütteldruckverdichtungsarbeiten in Landgewinnungsprojekten im Mittleren Osten. Das Ziel der Rütteldruckverdichtung ist es den aufgeschütteten Sand zu einer gewissen Lagerungsdichte zu verdichten und damit eine gewisse Steifigkeit und den Widerstand gegen eine eventuelle Bodenverflüssigung zu gewährleisten. Die Qualitätskontrolle der Verdichtungsmaßnahmen erfolgt mittels Drucksondierung (CPT). Dabei wird der Verdichtungserfolg indirekt ermittelt indem der bei der Drucksondierung gemessene Spitzenwiderstand q_c mit Hilfe von bekannten Korrelationsmethoden in die bezogene Lagerungsdichte D_r umgerechnet wird.

Im Mittleren Osten ist kalkreicher Sand mit einem hohen Gehalt an Muscheln und Korallen und deren Fragmenten weit verbreitet und wird oft als Baumaterial für Landgewinnungsprojekte verwendet. Aufgrund der Mineralogie und Kornform kommt es in diesen Sanden viel eher zur Kornzertrümmerung als in Quarzsanden. Bisher verwendete Korrelationsmethoden sind daher nur bedingt gültig, da der Spitzenwiderstand auch unter gleichen Bedingungen in kalkhaltigem Sand nicht so hohe Werte erreicht wie in Quarzsanden. Das kann dazu führen, dass der vom Bauherrn vorgegebene Zielwert des Spitzenwiderstandes nicht oder nur unter großem Verdichtungsaufwand erreicht werden kann und der Bauunternehmer zusätzliche Verdichtungsmaßnahmen durchführen muss, obwohl die geforderte Lagerungsdichte des Bodens bereits erreicht wurde.

Eine Alternative zur Anwendung der bekannten Interpretationsmethoden zur Berechnung des Mindestspitzendrucks ist die semi-empirische Karlsruhe Interpretation Method (KIM). Mit einem Fokus auf die spezifischen Eigenschaften von karbonathaltigen Sanden werden in der vorliegenden Arbeit die grundlegenden Aspekte der KIM, von den nötigen Laborversuchen über die Kalibrierung des hypoplastischen Stoffgesetzes bis zur Durchführung der Simulation der sphärischen Hohlraumaufweitung, beschrieben. Es zeigt sich, dass der Karbonatgehalt signifikanten Einfluss auf die Bodeneigenschaften und, in weiterer Folge, auch auf die Ergebnisse der KIM hat. Zum Abschluss wird eine Fallstudie über die Anwendung der KIM bei einem Landgewinnungsprojekt in den Vereinigten Arabischen Emiraten präsentiert.

Acknowledgements

I would first and foremost like to thank the initiator of this thesis and my supervisor Robert Thurner, Technical Director at KELLER Middle East, who gave me the great opportunity to work on my thesis at the KELLER office in Dubai. Mr. Thurner was always open and supportive whenever I had questions about my research or writing or life in the United Arab Emirates in general. He consistently allowed this paper to be my own work, but steered me in the right the direction whenever he thought I needed it and his enthusiasm and work-ethic were a great source of inspiration.

I would also like to thank my supervisor from my university Franz Tschuchnigg of the Institute of Soil Mechanics and Foundation Engineering at the University of Technology in Graz, Austria. Mr. Tschuchnigg provided immeasurable long-distance academic guidance, support and interest in this topic and I am gratefully indebted to him for his very valuable comments on this thesis.

I would also like to acknowledge Houman Soleimani Fard, Design and Estimation Engineer at KELLER Middle East, for his constructive feedback and advice and for sharing invaluable insights toward the topic of foundation engineering.

A very special gratitude goes out to everyone at the KELLER office in Dubai. It was fantastic to have the opportunity to work with you and spend the majority of my research time in your office. Every single one contributed to the successful completion of this thesis.

Finally, I must express my very profound gratitude to my Mother, my siblings, my common-law wife and my friends for providing me with unfailing love and support and continuous encouragement throughout my years of study and through the process of researching and writing this thesis. This accomplishment would not have been possible without them. Thank you.

Thank you for all your encouragement!

Contents

List of Figures

List of Tables

List of Abbreviations

MDD	**M**aximum **D**ry **D**ensity
CPT	**C**one **P**enetration **T**est
SCF	**S**hell **C**orrection **F**actor
KIM	**K**arlsruhe **I**nterpretation **M**ethod
SCE	**S**pherical **C**avity **E**xpansion
CCT	**C**alibration **C**hamber **T**est
PSD	**P**article **S**ize **D**istribution
FE	**F**inite **E**lement
1D-HPCT	**1**-**D**imensional **H**igh-**P**ressure **C**ompression **T**est
UAE	**U**nited **A**rab **E**mirates
DMD	**D**ubai **M**unicipality **D**atum

This is for my Mother and my
Father, to who I owe it all.

1 Motivation and background

The objective of this chapter is to provide an understanding of the topic, an introduction to the problem, as well as the scientific and practical relevance of the findings to the KELLER Grundbau GmbH. An overview will be given over the structure of this thesis and the approach to the topic will be explained.

1.1 Problem

The quality control of the compaction of reclaimed land is correlated to the density of the fill. The future behavior of the fill material is linked to a certain level of densification which will guarantee that particular minimal requirements related to the soil behavior (e.g. shear strength and stiffness) are obtained. The final goal of the densification is to limit eventual settlements of the construction for which the land has been reclaimed by increasing the stiffness modulus of the sand.

Densification requirements are translated into technical parameters like the relative density D_r or the maximum dry density MDD which can be measured directly by the sand replacement method or cutter cylinder or indirectly with a correlation between the cone resistance q_c obtained from a Cone Penetration Test and the relative density D_r. Schmertmann [1] and Jamiolkowski [2], among others, developed such correlations which are now widely used for the quality control for compaction measures in the industry. These equations use empirically determined coefficients derived from calibration chamber tests performed on a wide range of different silica sands and are therefore not able to replicate the particular characteristics of the sand found on a specific site. Another issue is the origin of the sands used for land reclamation projects in the UAE. As almost all the material used in such projects consists at least partially of calcareous sand, it is questionable if these correlations are able to reflect the actual quality of the densification in these sands.

Calcareous sands are made up from varying amounts of skeletal remains of marine organisms and show a high tendency towards grain crushing if subjected to pressure. Almeida et al. [3] and Nutt [4] have shown that, compared to silica sands, calcareous sands produce significantly lower q_c-values even if the soil is in a similar state. This raises the question whether the commonly used correlations between q_c and D_r (i.e. Schmertmann or Jamiolkowski) are still valid in carbonate sands. To overcome this issue, a so called shell correction factor (SCF) has been developed, which is supposed to accommodate the effect of crushing grains during cone penetration testing. The SCF is the ratio of the cone penetration resistance q_c of a crushable material and that of a

reference silica material and translates the measured calcareous cone resistance values into silica q_c values. Unfortunately, in practice, it has come to the point where the SCF-value is a result of negotiation between two parties with contradictory interests. The contractor on one hand aims for the highest SCF-value, which would reduce the cone resistance requirement and therefore, the amount of compaction. On the other hand, the consultant or client targets the lowest possible value in order to force the contractor to perform the highest level of compaction.

1.2 Approach to the problem

A possible solution to the problem stated in the previous paragraphs could be the application of the Karlsruhe Interpretation Method (KIM) in projects in which the sand shows a high carbonate content. The KIM was developed by Cudmani in 2001 [5] and is a semi-empirical method based on the numerical solution of a spherical cavity expansion problem. For these simulations, it is necessary to calibrate a hypoplastic constitutive equation which realistically models the behavior of a granular cohesionless material such as sand. One primary advantage of the KIM is its ability to be derived from sand samples taken from the actual site which allows for a realistic, site-specific representation of the material. A deeper insight into the theoretical background of the Karlsruhe Interpretation Method will be given in Chapter 4 of this thesis.

KELLER has retrieved sand samples from eight different projects over the past years and sent them to a geotechnical laboratory to have the necessary parameters for the KIM determined. Based on this collection of parameters, it was tried to find out which parameters influence the result of the KIM the most and when the application of the Karlsruhe Interpretation Method is advantageous over other correlation methods. The results of this investigation are presented in Chapter 5 of this thesis.

The PLM project in Dubai, United Arab Emirates served as a case study for the practical application of the Karlsruhe Interpretation Method. KELLER Middle East was appointed as a geotechnical contractor to carry out the necessary ground-improvement works consisting of deep vibro-compaction and surface compaction. During the reclamation of the project site a high amount of sea-shells and coral lumps was observed in the dredged sand which led to the assumption that the fill material must have an increased carbonate content. Sands with a high carbonate content (i.e. calcareous or carbonate sands) tend to produce lower cone resistances due to crushing of the grains and the concern was raised, whether the post-compaction CPTs will be able to achieve the required q_c-values. It was therefore decided to establish a site-specific correlation with the Karlsruhe Interpretation Method. Two sand samples were taken from the site and sent to a geotechnical laboratory for the determination of the parameters for the KIM. A detailed description of the necessary steps and the results is given in Chapter 6.

The goal of this investigation is to find out if the KIM is an adequate method to derive the relative density from CPT-results in calcareous sands and in what circumstances it is advantageous to use the Karlsruhe Interpretation Method.

2 Land reclamation in the United Arab Emirates

The economy of the United Arab Emirates relies heavily on revenues from the oil and natural gas industry but as crude oil is a finite resource, new streams of income had to be found. Dubai's efforts to become a world-class (luxury) tourism destination has dramatically increased the demand for high-value beachfront real estate. Artificially expanding the coastline and creating more residential and recreational property through land reclamation is a viable way to meet that demand. This led to the realization of major land reclamation projects like the Palm Jumeirah or Palm Jebel Ali which have significantly changed the geography of many parts of the country over the last 15 years.

This chapter will briefly explain the process of land reclamation by hydraulic filling and deep vibro-compation, the requirements for the fill material and the necessary equipment for both of these operations.

2.1 Land reclamation by hydraulic filling

Generally, land reclamation describes the process of creating new land by raising the elevation of the seabed or low-lying land, referred to as filling, or by draining water from an area that is surrounded by dikes which is referred to as polder-construction [6]. The following chapters of this thesis will only focus on land reclamation by hydraulic filling because it is the main way of creating new land in the United Arab Emirates.

In many cases, the reclamation of new land is the first part of a larger project like the construction of an airport, extension of a port or the development of a residential or industrial area. In the United Arab Emirates, extensive land reclamation projects have significantly changed the geography of the coast line of many parts of the country. Palm Jumeirah and Palm Jebel Ali, both artificial islands constructed off the coast of Dubai, are among the world's largest and most famous land reclamation projects.

2.1.1 Development of a land reclamation project

Even though the scale of land reclamation projects has vastly increased over the past 30 years, it is not a recent invention. First proof of land reclamation were found in the tidal areas of the Wadden Sea in the north of Germany and The Netherlands dating back around 2000 years. To provide safe ground during storm surges, high tides and

sea or river flooding, inhabitants of this area built settlements on man-made dwelling mounds called "terpen" or "wierden" [6].

In the 16th century, a new method of reclaiming land was developed in The Netherlands. By building a dike around a shallow watery area and draining the enclosed water from the low-lying land with pumps driven by windmills, a so-called "polder" was constructed [6]. Polders are areas of land reclaimed from a body of water, such as a lake or the sea and usually lie below the surrounding water level. This requires constant drainage of the inflowing water by pumps to prevent the water table within the polder from rising too high. These pumps were powered by windmills, many of which can still be seen across The Netherlands.

The reclamation of new land by hydraulic filling was first made possible with the large-scale application of modern centrifugal pumps [6]. One of the first major reclamation works carried out this way was the construction of a new industrial area in the Bay of Abidjan in the Ivory Coast in the 1960s [7]. Since then, urbanization and economic development arising from a strong growth of the world's population over the past decades have fueled an increasing demand for new land, in particular in densely populated areas along coasts. Figure 2.1 depicts the volume of reclamation works over the past 30 years and clearly shows an increase of the size of reclamation projects.

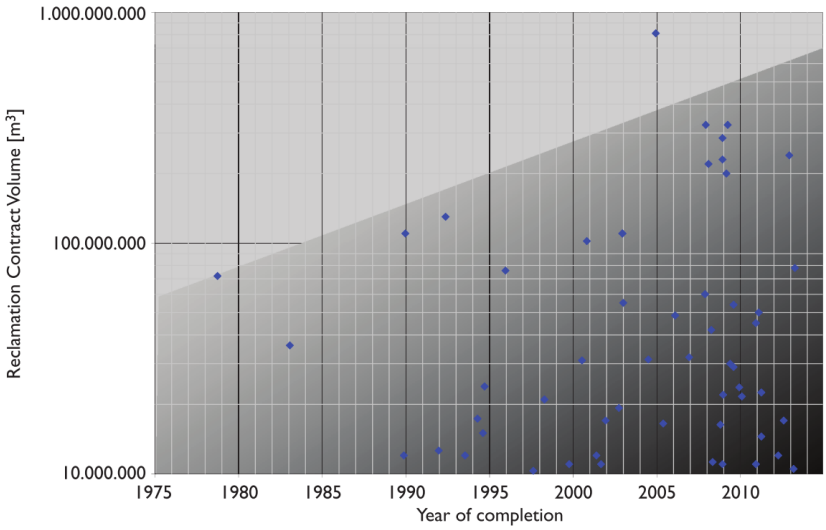

FIGURE 2.1: Trend of reclamation contract volumes over the past 30 years [6]

The development of reclamation projects can generally be divided in three necessary phases. In the project's initial phase, the scope of the project is defined, financing is secured, resources are identified and the feasibility of the project is assessed [6]. The search for suitable fill material in the vicinity of the planned reclamation site including initial geotechnical investigations of the proposed fill material as well as the assessment of other boundary conditions such as subsoil characteristics, water depths and hydraulic, morphological and meteorological conditions (e.g. waves, currents, wind) at the proposed reclamation site are carried out in this phase [6]. These investigations provide valuable data for the second phase.

In the design phase, the second phase of every project, the project's requirements and boundary conditions are translated into detailed technical specifications. The starting point of every design is always the intended use of the reclaimed land. Maximum values of the allowable settlements of the planned structures (e.g. buildings, roads, storage areas, runways) on the reclaimed land and sufficient safety against liquefaction lead to performance requirements of the fill mass. From these requirements, minimum values of basic properties like strength, stiffness, density and permeability of the fill mass are derived and technical specifications are set.

The construction phase is the last phase of every project and involves the actual hydraulic filling operations according to the technical specifications determined in the design phase. Creating new land by means of hydraulic filling can be divided in the following three consecutive activities:

1. Dredging of suitable fill material from a borrow area
2. Transport of fill material from the borrow area to the reclamation site
3. Placement of fill material in the reclamation area

The following chapter will focus on the construction phase and give a quick overview of the commonly used equipment and fill material. Explaining all phases in detail would go beyond the scope of this thesis. For a more in-depth description of the various aspects of land reclamation by hydraulic filling, reference is made to the *Hydraulic Fill Manual* by van't Hoff J. and van der Kolff A.N. [6].

2.1.2 Dredging of fill material

Dredging is an underwater excavation technique that is usually carried out to retrieve fill material for land reclamation projects. Suitable fill material may be obtained from a designated borrow area, from maintenance dredging or from capital dredging. A borrow area is an excavation site purely used for the extraction of geologic resources such as rock, sand or gravel to be utilized elsewhere as fill material whereas maintenance dredging describes the process of deepening or maintaining waterways or channels threatened to become too shallow for navigation due to the natural sedimentation of sand and mud. Capital dredging is usually carried out to create a new harbor, berth or waterway or to deepen an existing channel in order to allow larger ships to navigate through that channel.

Dredging can be divided into the two main categories, suction and mechanical dredging. Suction dredging uses the erosive action of water to loosen the material on the seafloor. The sand-water mixture is then pumped through a suction pipe to the surface whereas in mechanical dredging, the material is cut and retrieved in a grab or a bucket. Since most large scale land reclamation projects are carried out with suction dredges [6], three of the most commonly used types of suction dredges will be described in the following paragraphs.

Plain Suction Dredger (PSD)

The Plain Suction Dredger uses the erosive force of water jets attached to the suction mouth to loosen the material which makes it well-suited for the dredging of sand. The eroded material is mixed with water during the excavation process and pumped through the suction pipe to the surface. From there, it is either discharged onto a barge alongside the dredger or directly fed into a pipeline and pumped towards the reclamation site.

Cutter Suction Dredger (CSD)

The Cutter Suction Dredger is based on a combination of mechanical and suction dredging. A cutter-head at the end of the suction pipe cuts the material on the seafloor and transports it towards the suction mouth where water jets further loosen the dredged material. In the same way as in the PSD, the water-sand mixture is then either pumped onto a barge or directly to the reclamation site through a pipeline.

Cutter Suction Dredgers are often used in areas where the seafloor consists of harder materials like gravel deposits or surface bedrock for which a plain suction dredger would be ineffective [6].

Trailing Suction Hopper Dredger (TSHD)

The Trailing Suction Hopper Dredge also uses a combination of mechanical and suction dredging to loosen the material. When dredging, a suction pipe is lowered to the seafloor and the material is loosened with a combination of cutting it with a draghead attached to the lower end of the suction pipe and the erosive action of water jets. In contrary to the other two types of dredges, the TSHD is self-propelled and pulls the draghead across the ocean floor to retrieve the material. The material is then pumped into the TSHD's hopper and stored there instead of being discharged right away. Once the hopper is filled with dredged sand, the vessel moves to the reclamation area and unloads the material by opening doors in the bottom of the vessel, by so-called rainbowing or by pumping it through a discharge pipeline. TSHDs can be used to dredge sand, silt or clayey material.

Figure 2.2 shows the three dredge types described in the previous paragraphs.

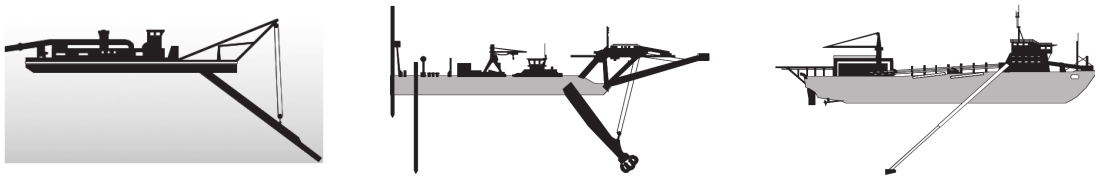

(A) (B) (C)

FIGURE 2.2: A Plain Suction Dredge (A), a Cutter Suction Dredge (B) and a Trailing Suction Hopper Dredge (C) [6]

2.1.3 Transport and placement of fill material

Certain characteristics and geotechnical properties of the fill mass such as density, grain size distribution, shear strength and compressibility are, to some extent, dependent on the applied placement method. The dredged fill material can be transported to the reclamation site by barges or, which is the more common method, by hydraulic transport through a pipeline [6]. During dredging, soil and water form a slurry which is pumped through a floating pipeline to the required location. If the dredged material is transported on a barge or in a TSHD's hopper, there are several different options to unload the vessel and place the fill at the reclamation site. The loaded fill material can be dumped by opening bottom doors or splitting the vessel's hull, the barge can connect to a discharge pipeline or the fill slurry can be rainbowed through a nozzle at the bow of the vessel (Figure 2.3).

FIGURE 2.3: Placement of fill by rainbowing it from a Trailing Suction Hopper Dredge [6]

Underwater placement of the fill is usually undertaken by TSHDs and barges which, after sailing to the reclamation site, open bottom doors or split their hulls allowing the sand-water mixture to fall through the water column down to the seabed.

The most common method of placing the fill is by pumping it through a floating pipeline that is connected to a PSD, a CSD, a TSHD or a barge. At the beginning of a reclamation project, the discharge end of the pipeline can be submerged to minimize the distance of the fill material falling through the water or positioned on a floating pontoon just above water. Later, when the fill mass has reached the surface of the water, the area in front of the discharge pipeline is leveled with bulldozers until it is raised and the pipeline can be routed over the newly created land. The bulldozers also perform an initial compaction of the fill while leveling the area.

Rainbowing the fill material to its designated location is often utilized if the water depth is too shallow and does not allow barges or TSHDs to sail to the reclamation site. It is used for beach replenishements but can also be used to create islands in open water. The range of rainbowing depends on the capacity of the dredger's pumps, the flow rate and the concentration of the sand water slurry and may be as large as 150 m [6].

Discharging the fill under water can lead to certain problems. While the fill sinks to the seafloor, the surrounding water will dilute the mixture reducing its concentration and increasing the area on the seafloor covered by the dumped material. Depending on the water depth at the reclamation site, the different grain fractions of the fill might segregate more or less. This way, even though the material in the borrow area might be a non-cohesive sand, the segregation of fines during the dredging, transport and placement process might form a soft cohesive soil at the reclamation area [6]. The segregated fines can accumulate in the fill mass, forming layers and lenses or even dominate whole parts of the reclamation area which can cause problems during the compaction of the reclamation fill later. Especially dredging and discharging of carbonate sands, which are prone to grain crushing, might result in a significant volume of soft cohesive materials at the reclamation area [6].

The resulting relative density D_r of the hydraulic fill after the placement strongly depends on the placement method. Table 2.1 sums up typical ranges of relative density for the different placement methods. It becomes clear that especially the fill mass under water doesn't attain suitable values of the relative density and require compaction measures to be undertaken in order to guarantee a certain resistance to excessive settlements and liquefaction.

TABLE 2.1: Typical values of the relative density D_r after placement depending on the placement method [6]

placement method	*relative density* D_r [%]
dumping from barge or TSHD (under water)	30 - 50
free flow through pipeline (under water)	20 - 45
free flow through pipeline (above water)	60 - 70
rainbowing (under water)	40 - 60
rainbowing (above water)	60 - 80

2.1.4 Carbonate sand as fill material

In principle, most cohesive soils such as clay or silt, non-cohesive soils such as sand and gravel and even rocks can be used as fill material. However, fine to medium quartz sands are preferred [6]. Should this kind of sand not be available or occur in insufficient quantities, lesser quality material, such as carbonate sand, silt or clay has to be used as fill. The intrinsic properties of these materials determine the ease of excavation and its behavior during transport to the reclamation area and will also influence the properties of the fill mass after placement. Therefore, the properties of the proposed material should be known in an early stage of a project as they will define several important aspects like the dredging equipment, method of fill placement and method of ground improvement. The soil investigation program for the quality assessment of a potential borrow area may include drilling of boreholes, vibrocoring and in-situ tests like Standard Penetration Tests or Cone Penetration Tests.

In the United Arab Emirates most of the fill material for the reclamation projects is carbonate sand with a high amounts of sea-shells and coral lumps dredged from the seabed. The properties of carbonate sands may deviate significantly from those of the more commonly used quartz sands and therefore show a different behavior during and after the reclamation process. The differences of the behavior between carbonate and quartz sands result in the crushability and angularity of the carbonate grains, the high initial void ratio of the carbonate fill mass after deposition and the cementation between the particles. A more detailed description of the properties of carbonate sand will be given in Chapter 3.3.

Although some of the properties of carbonate sands differ from the more commonly used quartz sand, carbonate sands can still be used satisfactorily as fill material if their deviating parameters are taken into account during the design phase. Some engineering problems that occur during the use of carbonate sand as fill material will be explained in the following paragraphs.

Degradation of sand particles

Due to the crushability of carbonate sand grains, the fill mass might show a higher fines content after deposition and therefore a different particle size distribution than the original in-situ one determined during the soil investigation of the borrow area before the start of the dredging operations [6]. This is caused by high impact stresses of the cutter teeth, the impellers of the pumps and abrasion along the pipeline wall during the discharge to the reclamation site.

The magnitude of the degradation depends on various parameters of the fill material like the carbonate content, original grain size distribution and particle shape but is also influenced by the type of dredger in use, the number of pumps, the length of the pipeline and the pumping velocity.

Hydraulic transport

Carbonate sands often contain high amounts of (fragmented) sea-shells which, in contrary to quartz sand grains, are not spherical shaped but more flaky and curvy. This shape influences the behavior of sand-water suspension during the hydraulic transport through a discharge pipeline. During transport the particles will most likely expose their smallest cross-sectional area perpendicular to the water flow which lowers the critical velocity of the sand-water mixture in the pipeline [6]. Should the velocity fall below that critical value, the sand particles will settle and the discharge pipe might clog up rapidly bringing the flow of fill material to a standstill. This problem may be aggravated by the tendency of the flow velocity to decrease with the accumulation of a bed load in the pipeline [6].

On the other hand, Miedema and Ramsdell [8] were able to show that the necessary erosion velocity to force settled particles into a suspension again, is higher for the disk-shaped sand particles of carbonate sands than for quartz sands. According to Miedema and Ramsdell [8], sea-shells will most likely lay flat after settling down with their convex side turned upward and protect themselves and underlying sediment against erosion.

2.2 Vibro-compaction of reclaimed land

Once the land reclamation is complete, the newly created land requires ground improvement measures to be undertaken in order to meet the design criteria. The goals of ground improvement are derived from the ultimate and serviceability limit state (ULS and SLS) of the design and usually involve [9]:

- increasing the density and shear strength of the fill mass to attain a positive effect on stability problems (ULS)
- reducing the compressibility for a positive effect on deformations (SLS)
- reduction/increase of permeability to reduce water flow and/or to accelerate consolidation (SLS)
- improving the homogeneity of the fill to equalize deformation (ULS/SLS)
- reducing the liquefaction potential by increasing the density of the fill (ULS/SLS)

The state of compaction, which is usually described in relative density and effective stress, strongly influences the engineering properties of a granular fill mass [6]. While there are various ground improvement techniques available for compacting a reclaimed fill mass and meeting the requirements listed above, this thesis will solely focus on soil compaction by means of deep vibratory compaction.

2.2.1 Historical development of vibro-compaction

During the first years of the 1930s in Germany, the Johann Keller GmbH was experimenting with a novel way to densify granular soils such as sand and gravel. This new technique involved placing a strong vibrator on the ground surface and pumping water through a pipe ending in the lower layers of the sand. The combination of introducing water into the ground and strong dynamic loads induced by the surface vibrator caused extensive reduction of internal friction, full saturation of the sand and a rearrangement of the sand grains with a minimized void ratio [9]. The results were very promising in laboratory tests but practical application of the new method was still rather complicated. To compact sufficiently thick layers of sand, powerful surface vibrators and complex watering systems had to be installed. But even the strongest vibrators of the time did not reach deeper into the ground than 2.5 m.

For the construction of the new congress hall in Nuremberg in 1936, a sand layer with a depth of 16 m had to be compacted. To overcome the shallow reach of the surface vibrators, the Johann Keller GmbH improved their densification method by building cylindrical vibrators and lowering them to the desired depth through a predrilled borehole. At the construction site of the new congress hall, the vibrator was suspended from a 23 m high wooden gantry and lowered into the borehole to the deepest layer of the sand to be compacted. The borehole was supported by a casing which was pulled up until the vibrator was fully surrounded by sand. From this position, the vibrator was switched on and pulled simultaneously with the casing. Thereby, the sand was densified over the whole depth with very promising results raising the

allowable bearing capacity from 250 to 450 kPa [9]. However, the method was very time consuming and the vibrator, which was still a prototype at that time, caused considerable repair expenses.

Learning from the problems of the Nuremberg-site, the Keller Company made a decisive improvement to the vibrator which eventually lead to the breakthrough of this compaction technique. By attaching a water-pipe on the side and a nozzle at the front end of the vibrator, it was possible to pump water directly to the tip which, together with the vibrations, caused liquefaction of the surrounding sand. This enabled the vibrator to sink into the ground to the required depth under its own weight making the time-consuming pre-drilling of the borehole unnecessary [9]. The same principle is still employed today by companies providing deep vibratory compaction works around the world.

After time, the slow-moving gantries that carried the vibrators and could only be moved on tracks, were replaced by crawler cranes. Together with other modern equipment, this reduced site installation costs and increased production rates considerably. Even though design principles of modern depth vibrators have changed only little since their invention, the vibrators were continuously improved with advancements in technology leading to the modern depth vibrator depicted in Figure 2.4.

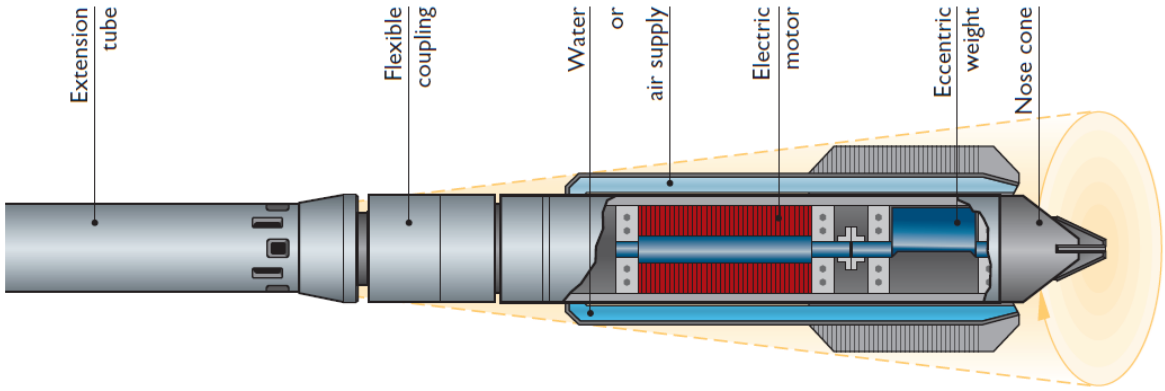

FIGURE 2.4: Cross-section through a modern depth vibrator [10]

A related ground improvement technique that should be mentioned here is the vibro-replacement method. Vibro-replacement is applied in cohesive soils and granular soils with high fines content where vibro-compaction would have little to no compaction effect [9]. A vibrator is penetrated into the ground to the desired depth with the aid of either water-jets (wet top-feed method) or pressurized air (dry bottom-feed method). This creates a cylindrical hole which is then filled with coarse gravel or crushed rock. Depending on which of the two methods is applied, the stone backfill either falls to the bottom of the hole through the annular space created between the vibrator and the adjacent soil (wet top-feed) or is fed through a pipe within the vibrator itself (dry bottom-feed). In both methods, the vibrator is retracted in steps up and down allowing the aggregate to fall in front of the vibrator's tip. Due to the horizontal forces induced by the vibrator, the backfill material is compacted and forced into the surrounding soil mass which creates a column of very compact stone aggregate up to ground level.

These stone columns improve the grounds bearing capacity because their stiffness is higher than the stiffness of the surrounding soil.

Curves of the grain size distribution are the primary indicator for the appropriate choice of vibratory technique. Sands and gravel with a fines content lower than 10% - 15 % can generally be compacted by vibro-compaction [9]. This limitation is usually already considered in the search for a borrow area with suitable fill material. Without introducing a coarser material that replaces the in-situ soil, an acceptable compaction result cannot be expected for a fines content in excess of 15% [9]. In these cases the vibro-replacement technique is a viable option. Figure 2.5 shows the limitations of the vibro-compaction technique in terms of grain size distribution.

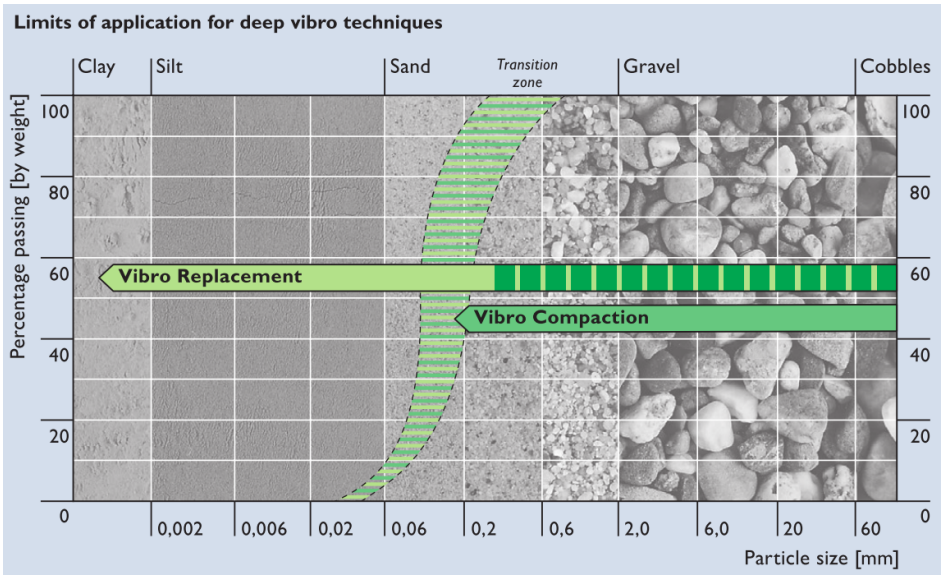

FIGURE 2.5: Range of application of deep vibratory methods [10]

2.2.2 Modern depth vibrators

A modern depth vibrator, as shown in Figure 2.4, is basically a cylindrical steel tube with a diameter ranging from 0.3 m and almost 0.5 m with a pointed tip. These vibrators contain an eccentric weight at the bottom which is mounted on a vertical shaft connected to an electrical motor situated within the upper part of the body. Typically, modern vibrators have a length ranging from 3 m up to 4.5 m and weigh between 1500 kg to around 4500 kg. Sand can be most effectively compacted by vibrating frequencies close to its natural frequency [9]. For this reason, the working frequency of common vibrators lies between 25 Hz and 60 Hz and is produced by the eccentric weight rotating around its vertical axis. This induces a centrifugal force in the surrounding soil ranging between 150 kN for smaller machines and above 700 kN for the strongest vibrators. Figure 2.6 depicts the mechanical principle of vibrators used for vibro-compaction and shows that the centrifugal force F depends on the mass M of the eccentric weight, the rotational speed ω and the eccentricity e of the weight.

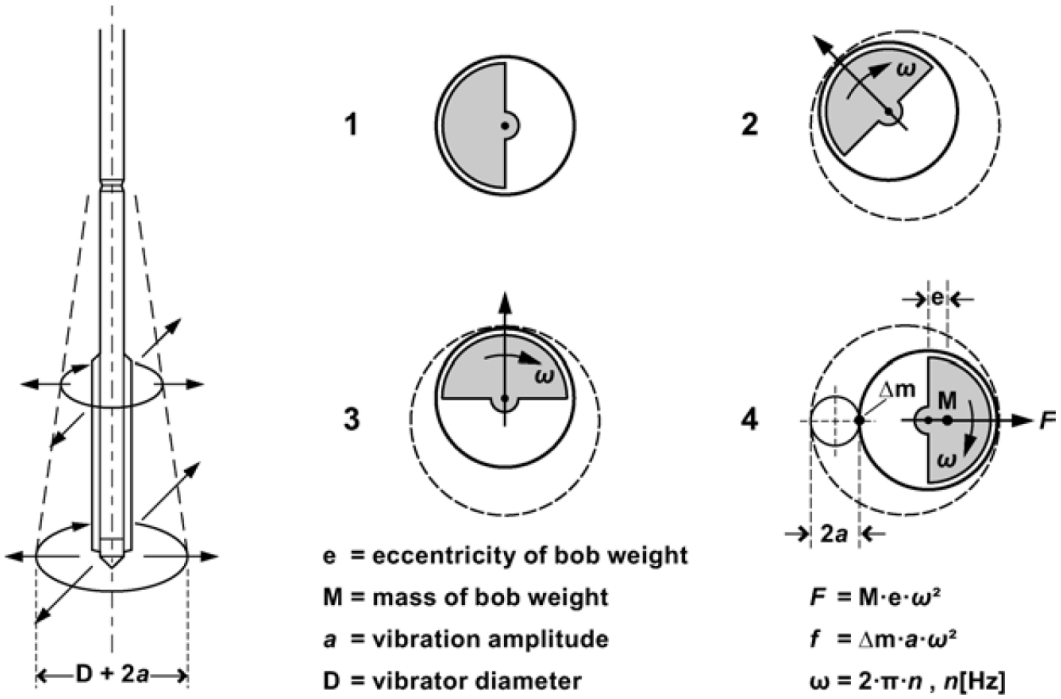

FIGURE 2.6: Operating principle of vibrators used for vibro-compaction and resulting forces [9]

2.2.3 The compaction process

During the vibro-compaction process, granular soils in a loose to medium dense state are densified by rearranging the particles under the influence of vibrations. The vibration process is usually accompanied by water jetting which temporarily reduces the inter-granular forces between the soil particles. This allows the grains to move into a more compact structure and leads to a reduction of the soil's void ratio (Figure 2.7), therefore increasing the density, stiffness and shear strength [6], [9].

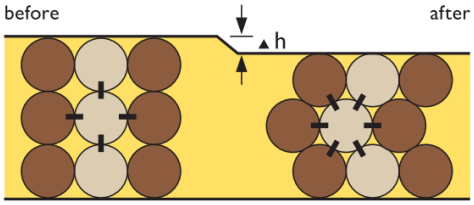

FIGURE 2.7: The soil's void ratio before and after vibro-compaction [10]

The compaction process consists of four steps that are carried out consecutively and are depicted in Figure 2.8. In the first step, the penetration phase, the water jets at the tip of the oscillating vibrator are turned to full pressure. The water saturates the soil around the probe and the strong vibrations induce an excess pore-water pressure. If the rate with which the pore-water pressure increases exceeds the rate of dissipation, the effective pressure acting between the particles is overcome and the soil liquefies [9]. Additionally, loosened sand is transported to the surface through the annulus between

the vibrator and the adjacent soil by the water flow. This assists penetration to the designated depth under the weight of the vibrator and its extension tubes.

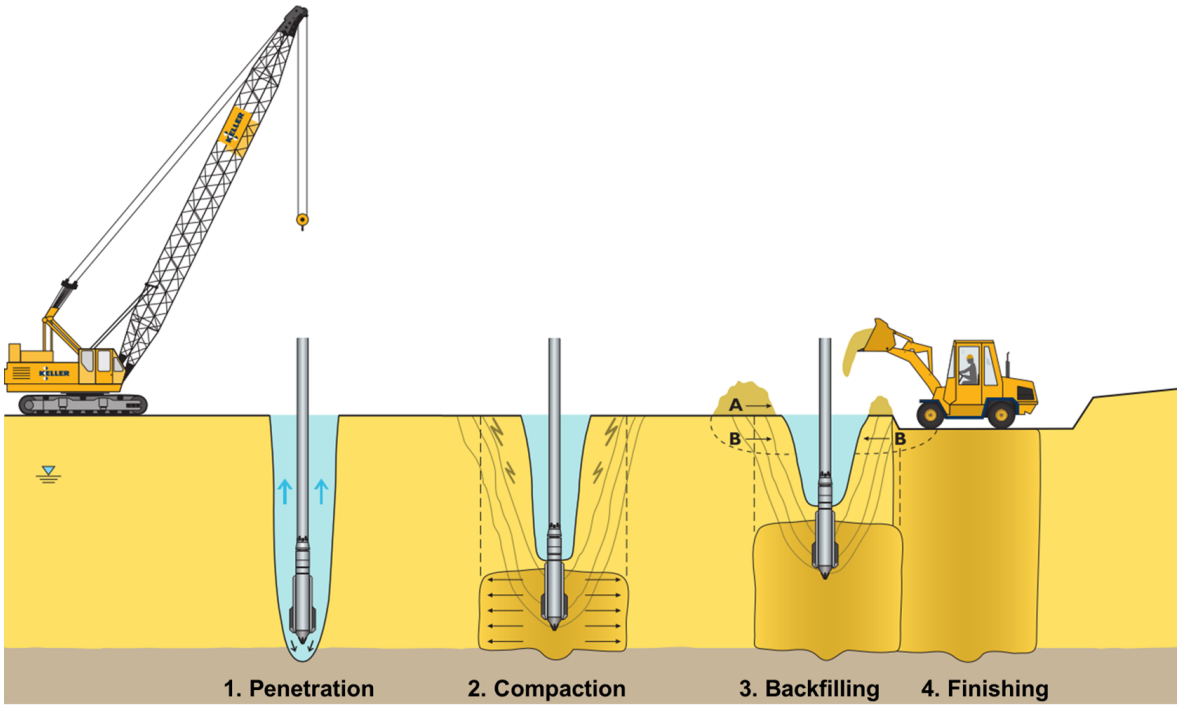

FIGURE 2.8: The process of vibro-compaction (adapted after [10])

In the second phase, once the vibrator reaches the design depth, water acting as a penetration aid is usually switched off or reduced considerably. The soil is compacted by slowly withdrawing the vibrator from the ground in prescribed stages of 0.3 to 1 m and halting the machine at each step along the way for either a predefined amount of time (approximately 30 to 90 seconds) or until the power consumption of the vibrator indicates sufficient compaction [9]. The time intervals for compaction depend on the soil properties, the required degree of compaction and the characteristics of the vibrator used.

The densification process causes a reduction of the pore volume in the soil surrounding the vibrator and leads to the formation of compaction craters on the surface. In phase 3 of the compaction process, these craters are either backfilled with material taken from the site or soil provided from somewhere else. This step is usually carried out simulataneously with the compaction while the vibrator is still in the ground. The resulting degree of volume reduction depends on the initial density of the material, the soil properties and the achieved degree of compaction. Typical values for the post-compaction settlements of the treated soil layer range between 5% and 10% of its untreated thickness [6].

In the last phase, after the compaction is completed, the ground surface is leveled and prepared for the subsequent construction works. Due to low overburden pressure, vibro-compaction is usually less effective in the top 2 m of the treated soil layer [9]. The compaction of this layer is carried out by standard surface compactors.

The described compaction process results in a zone of compacted sand with an improved density and a typical diameter of 3 m to 6 m. Depending on a number of variables like the characteristics of the applied vibrator and the soil properties, the effectiveness of vibro-compaction decreases with the distance from the center of the actual compaction point. Therefore, the points are arranged in a regular pattern which usually is either triangular or squared as shown in Figure 2.9. In the center of the chosen compaction pattern lies the weakest point in which the density is expected to be lowest. Since the specified minimum density for a project is also to be reached in the weakest point of the pattern, an additional safety margin is provided because all other areas away from this point are then characterized by a higher density. The spacing between the single points of the compaction grid is determined in a trial field at the actual project site. In this trial field, compaction grids with different spacings, usually ranging between 3 to 5 m [9], are carried out with a subsequent assessment of the achieved density. The respective compaction results are then evaluated by comparing pre- and post-compaction cone penetration test results to the specified criterion.

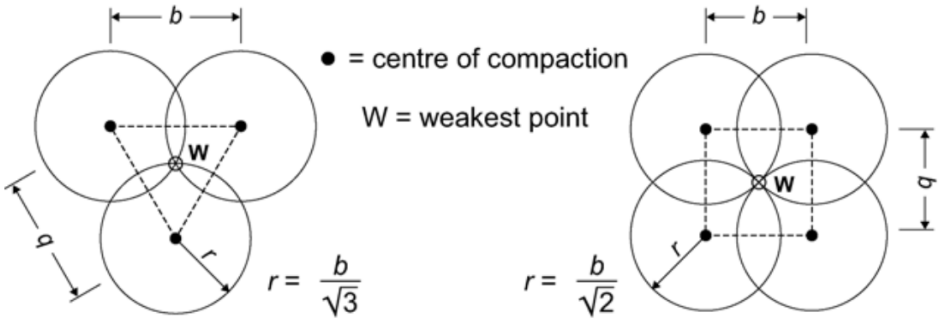

FIGURE 2.9: Triangular and squared compaction patterns [9]

3 Quality control of vibro-compaction

The quality control of the vibro-compaction of reclaimed land is correlated to the density of the fill which is linked to certain minimum requirements of shear strength and stiffness. Densification requirements are translated into technical parameters like the relative density D_r or the maximum dry density MDD which can be measured directly by the sand replacement method or indirectly with a correlation between the cone resistance q_c obtained from a Cone Penetration Test (CPT) and the relative density D_r. These correlations use empirically determined coefficients derived from calibration chamber tests which were performed on a wide range of different silica sands.

This chapter will describe the basic principles of the CPT and CPT interpretation methods like the methods developed by Schmertmann [1] or Jamiolkowski [2] and explain why it is questionable if these correlations are able to reflect the actual quality of the compaction works in calcareous sands.

3.1 Cone penetration testing

The Cone Penetration Test (CPT) is a versatile tool to identify sub-surface soil stratigraphy, measure soil properties and provide information to derive geotechnical parameters of the ground. A typical CPT consists of pushing an instrumented electronic penetrometer vertically into the soil with the help of a series of pushing rods in order to measure the cone resistance q_c and the sleeve friction f_s over depth.

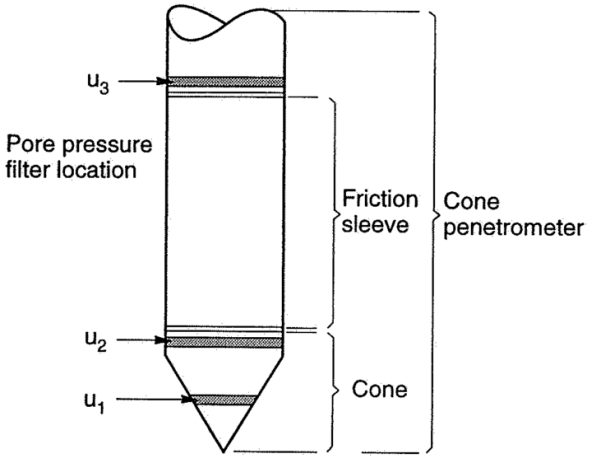

FIGURE 3.1: Schematic depiction of a piezocone [11]

Modern piezocones, like the one shown in Figure 3.1, also incorporate a piezometer for the measurement of the porewater pressure u and are referred to as CPTu.

The CPT(u) delivers continuous measurements over depth of the following three parameters:

- Cone resistance q_c

  The cone resistance q_c is defined as the total force acting on the cone F_c divided by the projected area of the cone A_c. q_c is usually stated in MPa.

- Sleeve friction f_s

  The sleeve friction f_s is defined as the total force acting on the friction sleeve F_s divided by the surface area of the friction sleeve A_s. f_s is usually stated in kPa.

- Porewater pressure u

  The porewater pressure u is measured at one, two or three positions: on the cone (u_l), behind the cone (u_2) and/or behind the friction sleeve (u_3). u is usually stated in kPa.

With the cone resistance q_c and the sleeve friction f_s, the friction ratio R_f can be calculated:

$$R_f = \frac{f_s}{q_c}[\%] \tag{3.1}$$

The friction ratio R_f is then used for one of the main applications of the CPT, soil profiling and determination of soil type. It has been shown that the cone resistance q_c is high in sands and low in clays whereas the sleeve friction f_s is low in sands and high in clays. This information might not allow an accurate prediction of soil properties like the grain size distribution but it can give a good indication of the mechanical characteristics like shear strength, stiffness and compressibility. Robertson [12] proposed to estimate the soil type based on cone resistance q_c and friction ratio R_f and developed Soil Behavior Type (SBT) charts. Figure 3.2 shows the SBT chart for the post-compaction CPT in box AZ28 of the PLM project in Dubai, UAE.

As can be seen in Figure 3.2 and from Table 3.1, the sand at the PLM site mostly classifies as SBT zone 5 (Sand mixtures – silty sand to sandy silt) and 6 (Sands – clean sand to silty sand).

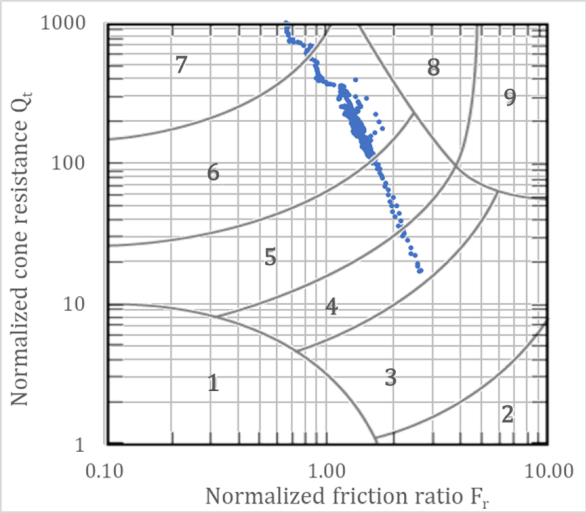

FIGURE 3.2: Soil Behavior Type chart for a post-compaction CPT

TABLE 3.1: CPT Soil Behavior Type (SBT) zones developed by Robertson [12]

zone	*soil behavior type*
1	Sensitive, fine grained
2	Organic soils - clay
3	Clay – silty clay to clay
4	Silt mixtures – clayey silt to silty clay
5	Sand mixtures – silty sand to sandy silt
6	Sands – clean sand to silty sand
7	Gravelly sand to dense sand Very
8	Very stiff sand to clayey sand
9	Very stiff fine grained

3.1.1 Historical development of the CPT

The first cone penetrometer tests for soil investigations were performed by the Dutch engineer P. Barentsen in 1932. Barentsen used a a 35 mm outside diameter gas pipe and a 15 mm steel inner push rod with a cone tip attached to measure tip resistances over depth [13]. The outer pipe and the inner rod were both pushed down by hand and the penetration resistance was measured with a manometer. In 1935, the first manually operated cone penetration machine with a pushing force of 100 kN was developed by the Delft Soil Mechanics Laboratory. This device also used a 35 mm outer pipe to eliminate the skin friction on the inner pushing rod and allowed the measurement of the cone resistance in increments of 150 mm [14].

A significant improvement of the CPT was the addition of the friction sleeve by Begemann in 1953 introducing a second measured parameter. Begemann used the measured

sleeve friction to calculate the friction ratio R_f and proposed to use this value to determine the soil type which was the first CPT-based soil classification system [11].

The shape and dimensions of modern cone penetrometers are based on the electric cone introduced by Fugro in 1965. This cone had several advantages over its mechanical counterpart such as allowing a continuous penetration, which made it faster than the mechanical cone, and continuous measurements for the first time. Electric penetrometers, connected to a field computer at the surface with a cable wired through the hollow push rods, also delivered more reliable measurements of the cone resistance and the sleeve friction and eliminated incorrect readings from gauges [11].

Another big step in the development of the CPT was the introduction of piezocones in 1974. These piezocones incorporated conventional electrical piezometers allowing a measurement of the porewater pressure in addition to the cone resistance and sleeve friction. It was found that these three values combined provided a promising way for soil identification and even an estimation of the overconsolidation of clay deposits [14].

Aside from obvious technological improvements since the 1970s, a number of other sensors such as temperature, electrodes, geophones, stress cells, radio-isotope detectors for density and water content determination have been developed for use in penetrometers over the past years.

3.1.2 Test equipment and procedure

In its basic form, a CPT-system consists of an electrical penetrometer, a hydraulic pushing system with pushing rods and a data acquisition unit [14]. These components are briefly described in the following paragraphs.

FIGURE 3.3: CPT probes with different projected area of the cone A_c.
From bottom: 2 cm^2, 10 cm^2, 15 cm^2 and 40 cm^2 [11]

The standard cone penetrometer is a steel probe with a diameter of 35.7 mm, thus having a projected cross-sectional area of $A_c = 10$ cm^2. It is fitted with a cone that has an apex angle of 60° and a friction sleeve located above the cone with an area of $A_s =$

150 cm^2. Figure 3.3 shows a range of cone sizes with A_c ranging from 2 cm^2 to 40 cm^2. Miniature cone penetrometers are usually used in laboratory tests and in calibration chambers whereas large diameter penetrometers are applied in gravelly soils [13]. The axial force F_c acting on the cone of the penetrometer is measured by an internal load cell and a second load cell separately registers the axial force along the sleeve F_s.

Due to porewater pressures acting on the shoulder area behind the cone and on the ends of the friction sleeve, the measured cone resistance q_c and the sleeve friction f_s have to be corrected. This correction is especially important in soft fine-grained saturated soils, where pore pressures can be large in comparison to the cone resistance [14]. In granular soils, such as the sands used for land reclamation projects in the UAE, no correction is needed because porewater pressures are usually negligible [13]. Carbonate granular soils are the material of interest in this thesis. Therefore, reference is made to *Cone Penetration Testing in Geotechnical Practice* by Lunne, T., Robertson, P.K. and Powell, J.J.M. [14] for a more detailed explanation of necessary corrections of the CPT parameters.

The pushing equipment of a CPT-system consists of pushing rods, a thrust machine and a reaction system (rig). On land, the hydraulic pushing equipment is usually mounted on specially built heavy-duty trucks that are ballasted to a deadweight in the order of 200 kN to act as a counterweight [14]. Figure 3.4 shows the CPT truck that was used on the site described in Chapter 6 of this thesis.

Standard push rods are hollow steel rods with an outer diameter of 35.7 mm in one-meter lengths and tapered threads, allowing them to be screwed together easily. The standard rigs usually store a stack of 30 to 40 1-m-long rods [13]. Hydraulic pushing systems of CPT-rigs are equipped with grips that transfer the downward pushing force into the rods, driving them into the ground at a standard constant rate of 20 mm/s. With large capacity pushing equipment in soft soils, depths of over 100 m have been reached [11]. The penetration depth can be increased by reducing the friction along the push rods with a friction reducer. A friction reducer simply is a section behind the penetrometer with a diameter larger than the following rods opening a larger hole and thereby reducing the soil-rod contact.

3.1.3 CPT as quality control of vibro-compaction works

As was explained in Chapter 2.2.3, the compaction points are usually arranged in a triangular or squared pattern. Since the densification is highest in the soil in the direct vicinity of the compaction point, the achieved degree of compaction will decrease with the increasing distance to this point [9]. This results in a non-homogeneous compaction over the treated area. The CPT is viable tool to carry out the quality control of the vibro-compaction works and verify the required densification of the soil improvement.

The reduction of the pore volume and densification of the ground is accompanied by an increase of the cone resistance measured in the CPT. Quality control of vibro-compaction is usually done by comparing pre- and post-compaction cone resistance values measured in a CPT. Pre-compaction CPTs are carried out on a much wider grid

FIGURE 3.4: CPT rig as it was used on the PLM site in Dubai, UAE

across the site than the post-compaction CPTs. In the project described in Chapter 6, the preliminary CPTs were performed on a grid of 100 x 100 m resulting in one measurement per 10000 m^2. The grid for post-compaction CPTs was set to 25 x 25 m, one set of CPTs every 625 m^2.

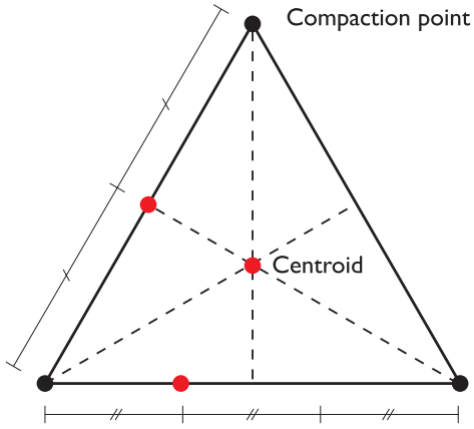

FIGURE 3.5: Possible post-compaction CPT points (red dots) [6]

Figure 3.5 shows possible locations for the post-compaction CPT points. One cone penetration test is situated at 1/3 or 1/2 of the distance between two compaction points and one at the "weakest" point in the center of the triangle. The results of these CPTs are averaged and a rolling mean over a depth increment of 0.5 to 1.0 m is formed to smoothen the curves and minimize the influence of incidental thin layers of less compacted fill in the quality assessment [6]. A rolling mean, also known as moving average, over a depth increment of 50 cm, for example, averages the measured q_c-values of the 25 cm above and the 25 cm below the considered depth. An example of such an averaged q_c-profile and its comparison to pre-compaction q_c-values can be seen in Figure 3.6. The data of these curves comes from the PLM project in Dubai, UAE which will be explained in detail in Chapter 6 of this thesis.

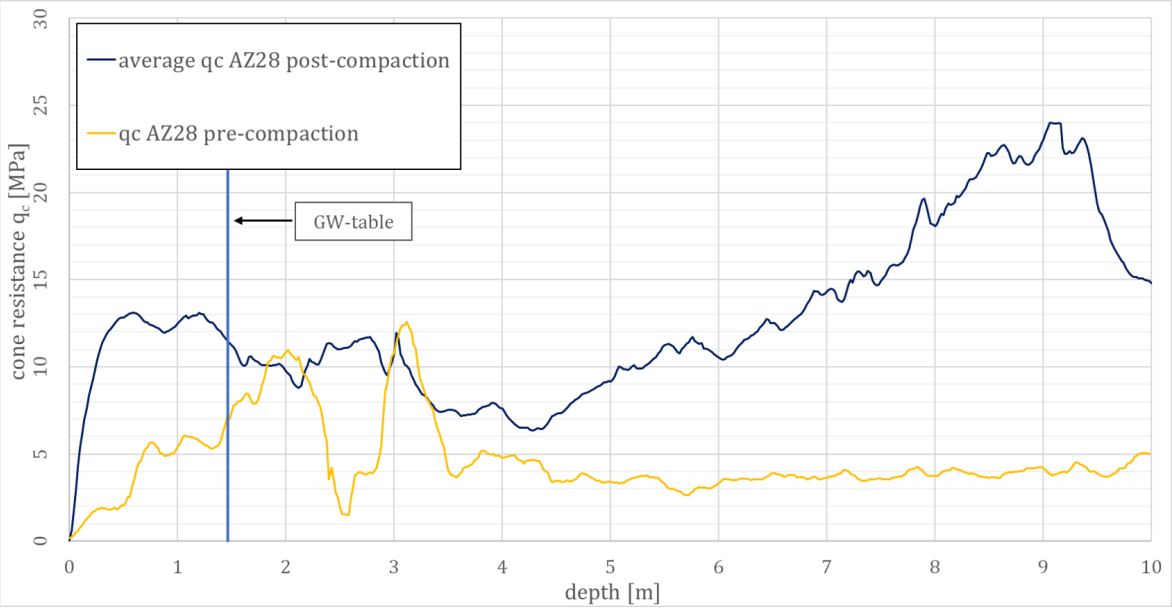

FIGURE 3.6: q_c-curves of post- (blue) and pre-compaction (yellow) CPTs

Compaction requirements are often stated in a minimum value of the relative density D_r. Various correlation methods have been developed with which a cone resistance curve corresponding to a certain relative density can be derived. This synthetic q_c-curve can then be compared to the actual measured CPT values to verify the compaction success.

3.2 CPT interpretation methods

Numerous correlations have been developed to estimate geotechnical parameters such as relative density D_r, the friction angle φ or the effective stress state σ' from CPT results. This thesis will focus only on the interpretation methods connecting q_c-values to the relative density D_r. Researchers like Schmertmann [1], Jamiolkowski [2] or Baldi [15] have proposed correlation methods which allow the assessment of the in-situ relative density D_r on the basis of the measured cone resistance values. These empirical correlation methods are based on the results of calibration chamber tests. The basics of calibration chamber testing and CPT interpretation methods will be described in the upcoming chapters.

3.2.1 Calibration chamber testing

Since retrieving undisturbed samples in a granular soil to determine the in-situ density is very difficult, the interpretation of CPT results relies largely on empirical correlations established with the results of calibration chamber tests. In order to correctly and effectively interpret the results of CPTs, it is important to know about the relationship between cone penetration resistance q_c and the relative density D_r. CPTs performed

in a calibration chamber allow to study this relationship under controlled conditions and establish correlations with which the in-situ relative density D_r can be estimated from q_c-values measured in the field.

A calibration chamber (CC) is a large cylindrical container in which the sand sample is deposited at a known relative density D_r and then consolidated to a certain stress state. Figure 3.7 shows the calibration chamber at the University of Karlsruhe in which Meier performed several calibration chamber tests (CCTs) on a calcareous sand sample from Dubai. Its dimensions are $d = 92$ cm in diameter and $h = 150$ cm in height resulting in a volume of $V = 0.9971$ m^3.

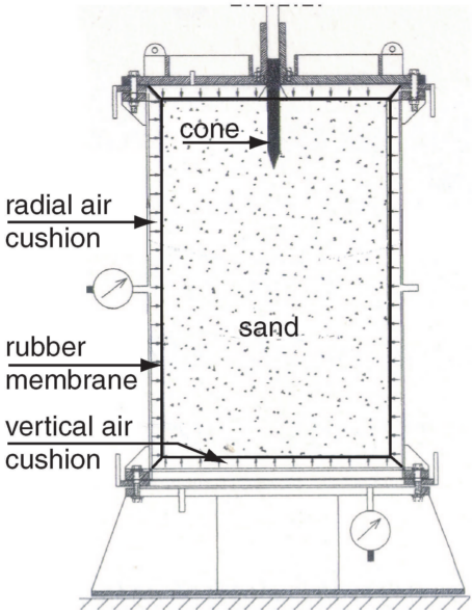

FIGURE 3.7: Cross-section of the calibration chamber at the University of Karlsruhe [16]

For the consolidation of the sample to the desired stress state, the radial and vertical stress σ_r and σ_v can be imposed independently with the aid of air cushions. Once the sample is prepared, a CPT is performed resulting in one value of q_c for the defined relative density D_r and stress. In the case of the calibration chamber shown in Figure 3.7, the CPT is performed with a standard 10 cm^2 cone at a constant penetration rate of 2 cm/s and a force capacity of 400 kN [16]. Performing a considerable amount of CCTs which cover a range of densities and stresses provides the basis for establishing an empirical relationship between the cone resistance q_c, the relative density D_r and the stress state [17].

However, there are certain problems and limitations connected to CCTs. Ghionna and Jamiolkowski [18] summed up the three main issues:

- *aging and cementation*

  The samples in CCTs are reconstituted and do not represent the soil structure that they would show in their natural deposits. The natural soil had time to build up its geological fabric by phenomena like drained creep, early diagenesis

and cementation [18]. Schmertmann [19] has shown that these effects influence the measured cone resistance, soil strength and stiffness significantly.

- *sand type*

  Many correlations have been established on the basis of CCTs performed on uniform, clean, predominantly silica sand samples which could be referred to as "academic" sand. Natural deposits of sands almost always contain a percentage of fines that can not be neglected and seldom are uniform [20]. This is particularly important for more crushable and more compressible and slightly cemented material such as calcareous sands used in a land reclamation project. Wesley [21] performed CCTs on a crushable pumice sand that was four times as compressible as a hard-grained silica sand and showed that the q_c-value measured in the CCT did not fit with previous correlations developed for quartz sand.

- *chamber size and boundary type effects*

  Establishing correlations between certain soil properties and the cone resistance q_c on the basis of calibration chamber results needs to take the effect of limited chamber dimensions into account [20]. These size effects can be examined when the results of CCTs performed on a sample with identical properties but in different CCs vary.

Another disadvantage of calibration chamber tests might be the necessary amount of sample material. The calibration chamber from the University of Karlsruhe (Figure 3.7) has a volume of $V = 0.9971$ m^3, thus a large amount of the investigated material is necessary. Wehr [22] states that for a series of CCTs performed on calcareous sand from Dubai at the University of Karslruhe, three tons of soil samples were used.

For more details on these issues, reference is made to *Cone penetration tests in a virtual calibration chamber*, the PhD-thesis of Butlanska J. [20].

3.2.2 German Standard DIN 4094

The purely empirical equations stated in the DIN 4094-1:2002 allow the calculation of the relative density D_r from measured cone resistance values. The equations were developed based on tests performed in the 1950s and 1960s in Berlin on samples of Berlin sand which is a mixture of quartz and feldspar. As can be seen in Equations 3.2, the only differentiating factor for the equations is the coefficient of uniformity $C_u = d_{60}/d_{10}$ [16]:

$$D_r = -0.33 + 0.73 \cdot \log(q_c) \qquad C_u \leq 3 \text{ and } 3 \leq q_c \leq 30 \tag{3.2}$$

$$D_r = -0.25 + 0.31 \cdot \log(q_c) \qquad C_u \geq 6 \text{ and } 3 \leq q_c \leq 30$$

This interpretation method should be avoided because it neither takes soil properties like compressibility or the hardness of the grains nor the state of stress into account. It is also not applicable for soils with a value of C_u between 3 and 6.

3.2.3 Interpretation method by Schmertmann

The method developed by J. H. Schmertmann is an empirical relationship between the cone resistance q_c and the relative density D_r based on 80 calibration chamber tests on different silica sands [1]:

$$q_c = C_0 \cdot \sigma_v'^{(C_1)} \cdot \exp^{(D_r \cdot C_2)} \tag{3.3}$$

$$D_r = \frac{1}{C_2} \cdot \ln\left(\frac{q_c}{C_0 \cdot \sigma_v'^{(C_1)}}\right) \tag{3.4}$$

The C_i constants take different material parameters into account whereas the stress-state is incorporated by the effective vertical stress σ_v'. Table 3.2 lists various C_i-constants to be used with Schmertmann's equation that were calibrated by other researchers throughout the years.

TABLE 3.2: C_i-values presented by different researchers

correlation		C_0	C_1	C_2
Schmertmann (1976) [1]	silica	12.31	0.71	2.91
Baldi et al. (1986) [15]	silica	157	0.55	2.41
Meier (2007) [16]	silica	9.39	0.85	3.89
	calcareous	14.23	0.67	2.90

The problem with the Schmertmann equation is that it is based only on silica sands. Schmertmann's C_i-values do not account for grain crushing or the lower compressibility of calcareous sands which are the main reasons for the differences between the cone resistance in silica and calcareous sands. The C_i-constants developed by Meier [16] were derived from calibration chamber tests performed on silica Karlsruhe sand and a calcareous sand from Dubai.

The C_i-values obtained by Baldi are based on extensive calibration chamber studies on moderately compressible silica Ticino sand [15].

Note that in order to use Schmertmann's equation together with the listed C_i-values from Schmertmann and Meier, q_c and σ_v' have to be inserted in kgf/cm^2 (1 kPa = 0.01019716 kgf/cm^2) [16]. Baldi's values can be entered directly without converting the q_c and σ_v' to kgf/cm^2. That's why Baldi's C_0-value of 157 seems to be out of scope but actually accommodates the conversion of kPa to kgf/cm^2.

3.2.4 Interpretation method by Jamiolkowski

Jamiolkowski et al. [2] analyzed the data obtained from 484 calibration chamber tests performed with three different silica sands and developed the C_i-parameters listed in Table 3.3.

$$q_c = C_0 \cdot p_a \cdot \left(\frac{\sigma'_v}{p_a}\right)^{C_1} \cdot \exp^{(D_r \cdot C_2)} \tag{3.5}$$

In the equation, p_a is the atmospheric pressure (98.1 kPa) which is entered in the same unit of stress as the vertical effective stress σ'_v.

TABLE 3.3: C_i-values developed by Jamiolkowski et al. [2]

correlation	C_0	C_1	C_2
Jamiolkowski	17.68	0.50	3.10

Just like the Schmertmann equation, Jamiolkowski's coefficients were developed from a database that does not include any calcareous sand.

3.3 Calcareous sand

Calcareous sands are defined as sands predominantly consisting of carbonate minerals, most commonly calcite, and are therefore also frequently referred to as carbonate sands. These sands are widely distributed in the warm and shallow oceans in the world's tropical and subtropical zones between latitude 30° north and 30° south [6].

In general, all sediments containing calcium carbonate ($CaCO_3$) can be described with the adjective *carbonate*. Clark and Walker [23] and Meigh [24] proposed a more detailed classification for carbonate rocks in which they make the following distinction based on the soil's carbonate content:

- a sand is classified as a *carbonate* sand when its carbonate content is above of 90%
- *siliceous carbonate* sand is a sand which has a carbonate content between 50 and 90%
- *calcareous* sand describes deposits with a carbonate content ranging between 10 and 50%

In this thesis, however, the distinction is more general and both, *calcareous* and *carbonate*, are used to describe sands that contain $CaCO_3$.

3.3.1 Origin and mineralogy

If a carbonate sand is formed by the accumulation of skeletal remains of small sea-organisms, such as shells and corals it is referred to as a bioclastic deposit. Carbonate sand can also have a non-organic origin, like the chemical precipitation from water overly saturated with carbonate.

The sands in the UAE mainly contain seashells and coral lumps in varying concentrations. The carbonate content of samples from the projects in the database varies between 9.73 % in the Al Zour LNG sand and 100% in the material used for the land reclamation at the PLM project in Dubai. In literature about calcareous sand the term shell content can sometimes be found. It should be noted that there is a difference between shell and carbonate content. The shell content only describes what percentage of a sand is made up from actual sea-shells or fragments of them whereas the carbonate content considers the complete portion made up from $CaCO_3$, i.e. sea-shells, corals and other skeletal remains. To explain the mechanical behavior of calcareous sands it is necessary to take the whole bioclastic $CaCO_3$-fraction into account. Therefore, the following chapters will explain the engineering properties of calcareous sands in relation to their carbonate content.

It was found that the carbonate content has a major influence on three basic geotechnical parameters: the limit void ratios e_{min} and e_{max} (counted as one), the friction angle φ_c and the grain density ρ_s.

3.3.2 Influence of carbonate content on soil properties

An extensive literature research resulted in a database of 23 different materials with carbonate contents ranging from 0% to 100% and showed that calcareous sands tend to have higher void ratios e_{min} and e_{max}, higher friction angles φ and a higher grain density ρ_s than silica sands. Table A.1 lists all materials found in literature.

Limit void ratios e_{min} and e_{max}

Figure 3.8 shows the relationship between the limit void ratios e_{min} and e_{max} and the carbonate content. Both parameters show an increase with increasing content of $CaCO_3$. It is assumed that this behavior is caused by the angular shape of shells and shell fragments which form strongly interlocking grain skeletons with a higher number of voids. Another contributing factor is the tendency of corals to have porous skeletons made of calcium carbonate.

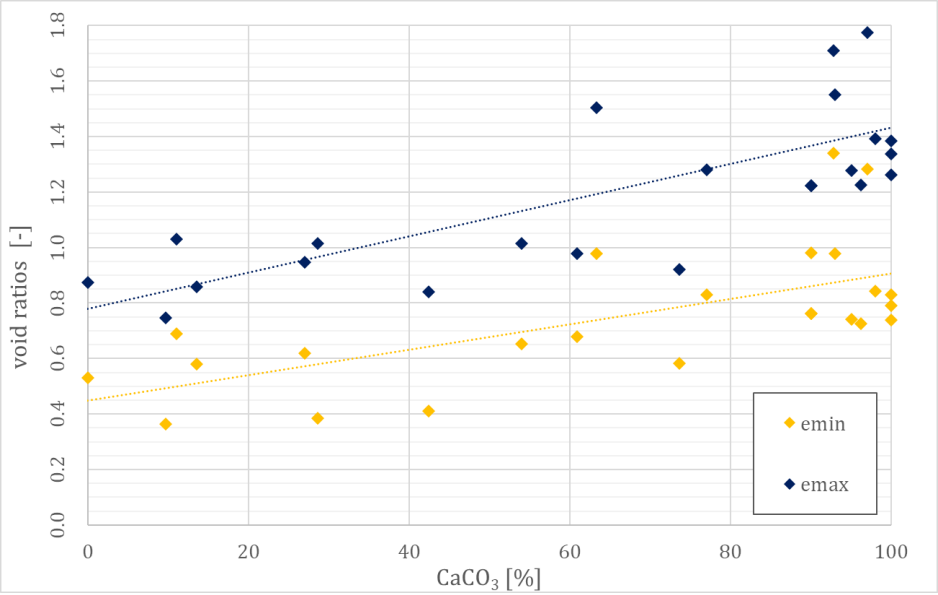

FIGURE 3.8: Relation between carbonate content and limit void ratios e_{min} and e_{max}

Critical friction angle φ_c

Figure 3.9 shows how the critical friction angle φ_c of a soil significantly rises with an increasing $CaCO_3$ content. This behavior is attributed to the interlocking of the grain skeleton due to the angular shape of the shell fragments. Another factor in this behavior is that the calcareous components are younger than the silica components in geological terms. The silica fraction of the soil was subject to environmental influences for a long time, grinding the single particles into a rounded shape over time. The calcareous shell fragments have not undergone this treatment and therefore remain rough and jagged.

Silica sand particles are made up from silicon dioxide (SiO_2), whereas the main mineral in calcareous sand is calcite or aragonite (both $CaCO_3$). While SiO_2 reaches a value of 7 on Mohs' scale of hardness, $CaCO_3$ only has a hardness of 3. It is therefore believed that calcareous sand particles would continue breaking into smaller angular particles rather than become roundly shaped over time.

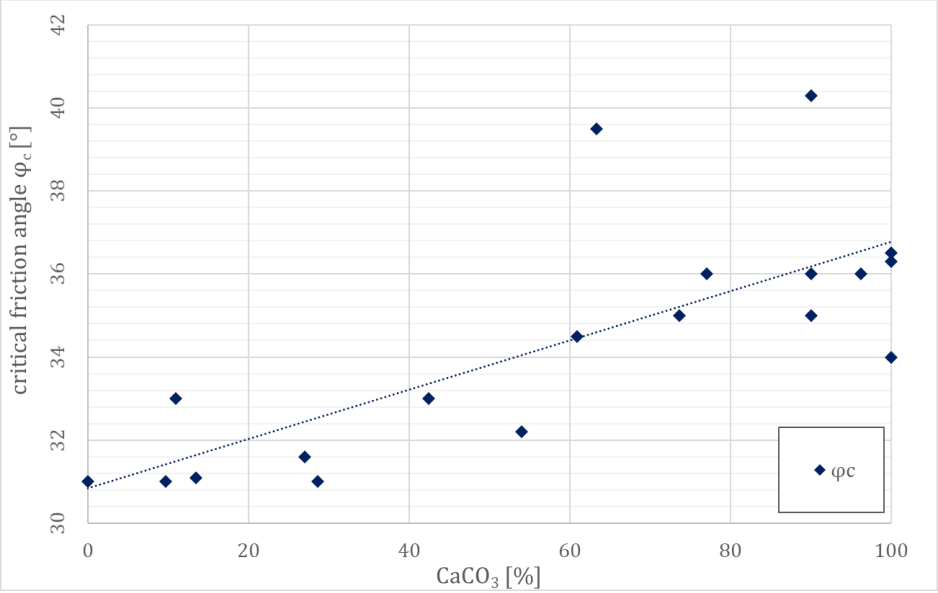

FIGURE 3.9: Relation between carbonate content and the critical friction angle φ_c

Grain density ρ_s

Figure 3.10 depicts the relation between an increasing carbonate content and the grain density ρ_s. Silica sands mainly consist of quartz occurring as the mineral silicon dioxide (SiO_2) whereas calcareous sands are primarily composed of calcium carbonate ($CaCO_3$). Quartz has a density of 2.6 – 2.7 g/cm^3. Calcium carbonate most commonly occurs as the mineral calcite which has a density of 2.7 g/cm^3. However, seashells and corals might also be made up from the carbonate mineral aragonite which has an even higher density of 2.9 – 3.0 g/cm^3. This explains why a rising carbonate content leads to an increase of the grain density ρ_s.

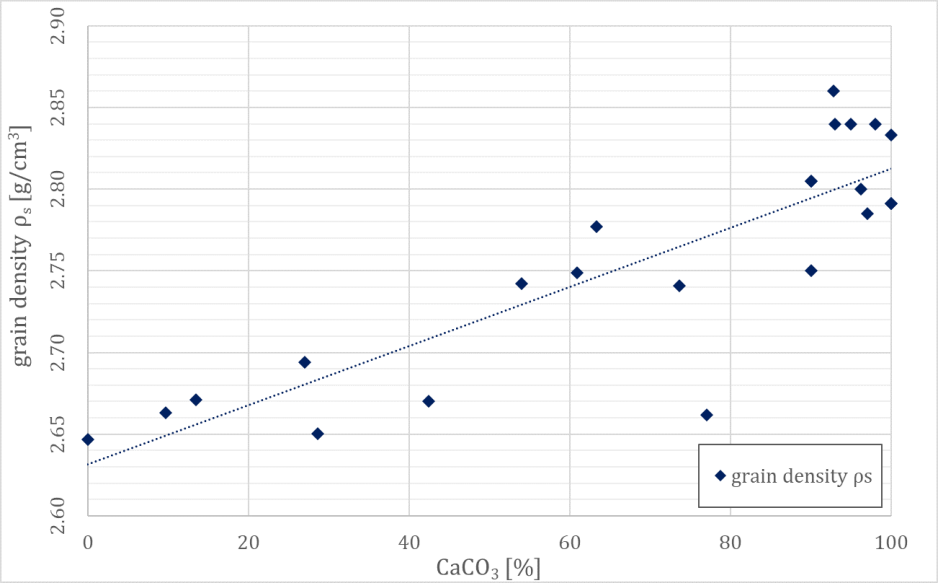

FIGURE 3.10: Relation between carbonate content and the grain density ρ_s

4 The Karlsruhe Interpretation Method

This chapter will explain the theoretical concepts which provide the basis of the Karlsruhe Interpretation Method (KIM). To understand the KIM, it is important to understand the basics of hypoplasticity and the cavity expansion theory. After a short introduction to hypoplasticity in general, the hypoplastic constitutive equation as it was proposed by "von Wolffersdorff" [25] will be explained and the determination of the necessary model parameters will be described. Subsequently, the cavity expansion theory with a focus on spherical cavity expansion will be described and it will be shown how the so-called shape factor k_q is derived. Finally, the KIM-equation and the results of the Karlsruhe Interpretation Method will be explained.

4.1 Introduction

In contrast to the interpretation methods presented in Chapter 3 which are based on empirically determined parameters, the Karlsruhe Interpretation Method combines an empirical parameter and numerical simulations to calculate the cone resistance corresponding to a certain state of the soil. As shown by Meier in his dissertation [16], the Karlsruhe Interpretation Method is a promising tool to interpret the the results of a simple Cone Penetration Test especially in calcareous sands where commonly used correlations between the cone resistance q_c and the relative density D_r are no longer valid [3].

The Karlsruhe Interpretation Method (KIM), developed by Cudmani in 2001 [5], is a semi-empirical method based on numerical simulations of a spherical cavity expansion. Cudmani established a relation between the limit pressure p_{LS} obtained from spherical cavity expansion calculations and the cone resistance q_c by introducing a so-called shape factor k_q. The shape factor k_q is derived from the results of CPTs performed in a calibration chamber and represents the empirical part of the KIM-equation:

$$q_c = k_q(D_r) \cdot p_{LS}(p'_0, D_r) \tag{4.1}$$

Equation 4.1 consists of two parts, the shape factor k_q and the limit pressure p_{LS}. While the empirically determined shape factor k_q is only dependent on the relative density D_r, the limit stress p_{LS} is derived from the solution of a spherical cavity expansion (SCE) problem. More information about the SCE will be given in Chapter 4.3

and the shape factor will be explained in the subsequent Chapter 4.4. A hypoplastic equation, calibrated to the soil present at the specific site, is used to model the mechanical behavior of the continuum in which the spherical cavity expansion (SCE) is simulated. The input parameters required for the calibration of the hypoplastic equation are determined by basic lab-tests performed on disturbed samples taken from the site under investigation [25]. This guarantees that the characteristics of the soil on site are properly represented in the simulation. The use of the site-specific hypoplastic model is a big advantage of the KIM over other correlation methods which use general parameters often determined on a wide range of sands.

In the following chapters, the hypoplastic parameters, the spherical cavity expansion and the determination of the shape factor k_q will be explained with a focus on the characteristics of calcareous sands in general and the KELLER database in particular.

4.2 Hypoplasticity

The very first version of the hypoplastic constitutive equation was presented by Kolymbas in 1977 [26] at the Institute of Soil and Rock Mechanics at the University of Karlsruhe. In his studies, Kolymbas answered the question whether it was possible to develop a mathematical expression for irreversible deformations without applying the concepts of elastoplasticity, such as yield surface, plastic potential, flow and hardening rules. He was motivated by the observation that many granular materials do not show an elastic regime at all and rather develop plastic deformations from the beginning. As a consequence, the elastoplastic approach of dividing the deformations into an elastic and a plastic range, seems to be debatable and does not necessarily reflect the real mechanical behavior of granular materials such as sand. As a result of his research, Kolymbas was able to formulate a single equation describing the change of the stress in a simple grain skeleton due to rearrangement of the grains and other important features of the behavior of granular soils. It recognizes that plastic deformations may set on from the very beginning of the loading process and does therefore not distinguish between plastic and elastic ranges. Another outstanding aspect of hypoplasticity is its simplicity. Contrary to elastoplasticity, it avoids the aforementioned additional notions like yield and plastic potential surfaces or hardening rules.

The applicability of the hypoplastic constitutive equation originally proposed by Kolymbas was quite limited. Several researchers have since introduced improved versions to overcome shortcomings of the initial equation and adapted it to soils with different characterisitics. Niemunis and Herle introduced the concept of intergranular strain in 1997 [27] which allows to model the effects of small-strain stiffness in hypoplasticity. A hypoplastic equation for fine-grained soils like clay was presented by Mašín in 2005 [28]. Mašín's model combines general principles of hypoplasticity with traditional critical state soil mechanics. As can be seen, hypoplasticity is applicable to a wide range of problems and materials and should therefore rather be regarded as a framework of constitutive models than one particular equation.

The version presented in the following chapters was developed by von Wolffersdorff in 1996 [25] and is also the one Cudmani used for his CPT interpretation method. It was primarily developed to reproduce the mechanical behavior of granular materials such as sands and gravels.

4.2.1 The hypoplastic model by „von Wolffersdorff"

The model by „von Wolffersdorff" is considered to be the reference hypoplastic model for granular materials like sand and gravel. As von Wolffersdorff explains in his paper [25], the presented constitutive relation requires four material constants that allow for a realistic description of the mechanical behavior over a wide range of stresses and densities and four calibration constants that need to be calibrated for each material specifically [25]. The parameters that are required for the constitutive equation are listed in Table 4.1.

TABLE 4.1: parameters for the hypoplastic constitutive model and the necessary lab tests

parameter		*labtest*
critical friction angle	φ_c	angle of repose test
limit void ratios	e_{i0} e_{c0} e_{d0}	densest and loosest packing (DIN 18126)
granulate hardness	h_s	high-pressure oedometer (DIN 18135)
exponent	n	
exponent	α	drained triaxial test (DIN 18137-2)
exponent	β	

Another important parameter for the hypoplastic model is the initial void ratio e_{init}. This void ratio lies somewhere between $e_d \leq e_0 \leq e_i$ and, as it defines the initial density state of the soil, has a significant influence on the results of the calculations with the hypoplastic model.

The hypoplastic constitutive model of „von Wolffersdorff" describes idealized characterisitics of a so called *simple grain skeleton*. Simple grain skeletons are characterized by the following properties [29]:

- The state of the grain skeleton is defined by the grain stress-tensor $\dot{\sigma}$ and the void ratio e.
- Deformation takes place only due to rearrangement of grains.
- The sand grains are considered indestructible. Abrasion or grain crushing is not considered.

- Three limit void ratios exist. There is an upper limit and a lower limit void ratio, e_i and e_d respectively. Both decrease with an increasing mean effective grain pressure p'_s. If $e > e_i$ macro-voids occur and contacts between grains are lost which would render the grain skeleton non-existent. In case of $e < e_d$ the grain skeleton would transform into a kind of dry masonry. There is also a critical void ratio e_c which, just like the other two, decreases with an increasing mean effective stress p'_s and is reached after large monotonic shear deformations.

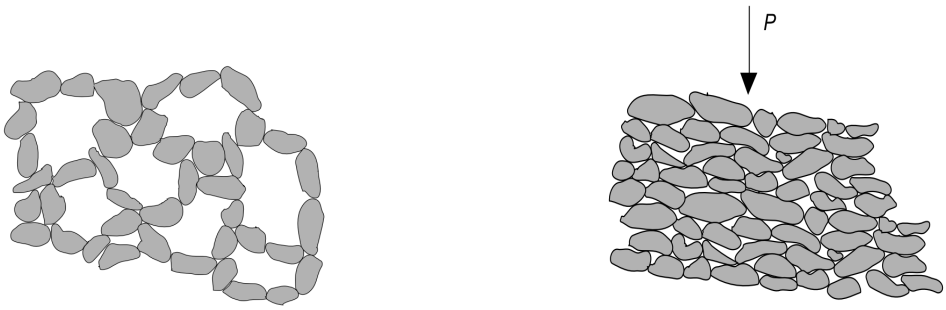

(A) (B)

FIGURE 4.1: (a) Macrovoids occur when $e > e_i$, (b) dry masonry is formed when $e < e_d$ [29]

- The mechanical behavior of the grain skeleton is rate-independent. This means the stress-strain curves do not change with stress- or strain-rate.
- In case of proportional deformation paths, the corresponding stress paths will, independently from the initial path, become proportional. This is the so-called *Swept Out of Memory* behavior (SOM), a very characteristic behavior of granular materials.
- Attractive forces like physico-chemical forces and cementation of the grain contacts are not considered.

4.2.2 Determination of the model parameters

To ensure good representation of the material, it is preferable that the parameters of the hypoplastic model for sand depend directly on the granulometric properties like grain shape, angularity, distribution of grain size, friction angle and a sort of grain hardness. The process of the determination of the parameters for hypoplasticity has been extensively elaborated in various publications by Bauer (1996) [30], von Wolffersdorff (1996) [25], Herle and Gudehus (1999) [31] and Herle (2000) [32] and will be summarized on the next pages.

Critical friction angle φ_c

The critical friction angle φ_c determines the resistance of a granular material to monotonic shearing in a critical state. This critical state is reached during large monotonic shearing if both, the stress rate and the volumetric deformation rate become zero. A drained or undrained triaxial test or a simple- or direct-shear test on an initially very loose specimen ($e \approx e_{max}$) are suitable for the determination of φ_c. However, there's certain difficulties connected to the determination of the critical friction angle from the direct-shear or the triaxial test. Reaching the critical state under the premise of a homogeneous deformation is hardly possible and, in addition to that, the stress-state is not precisely defined in the direct-shear test. The issues with the triaxial-test stem from the formation of shear-bands in the specimen during the test which make a homogeneous deformation impossible [29]. For a dry granular material like sand, a simple estimation of φ_c can be achieved from the angle of repose test as shown in Figure 4.2. This test has the advantages of being simple, easily reproducible, fast and therefore, cheap.

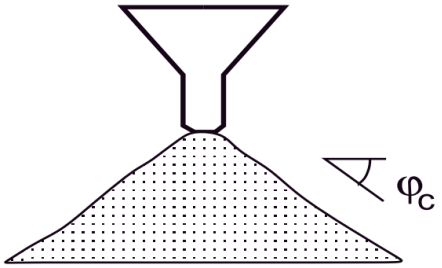

FIGURE 4.2: Schematic depiction of the angle of repose test to determine φ_c [31]

The angle of repose is the inclination of the slopes of a pile of sand when it is poured. During the angle of repose test, the goal is to obtain a sand heap in its loosest state by filling a funnel with dry sand and lifting it vertically without letting the funnel lose contact to the sand material. The steady flow of grains causes a quasi-critical state to be reached. The actual value of the critical friction angle can then be calculated by measuring the height and diameter of the pile or measured digitally by means of image processing.

Herle and Gudehus [31] studied the influence of the particle size distribution on the angle of repose and found that the mean grain diameter d_{50} has a larger effect than the coefficient of uniformity C_u. According to Herle and Gudehus, larger sand grains have to overcome higher couple stresses while rolling down the pile during the angle of repose test which may be the explanation for the increase of φ_c with the grain size. For the calcareous sands in the KELLER-database it was found that the above statements are true for all materials but one. The sample from the Al Zour LNG site has a low value of $\varphi_c = 31°$ and a high value of $d_{50} \approx 1.00$ mm. That's also the reason why the trendline in Figure 4.3 (A) is horizontal. If the Al Zour LNG point in the bottom right is ignored, the trend clearly shows an increase of the friction angle with d_{50} and C_u and confirms the findings of Herle and Gudehus.

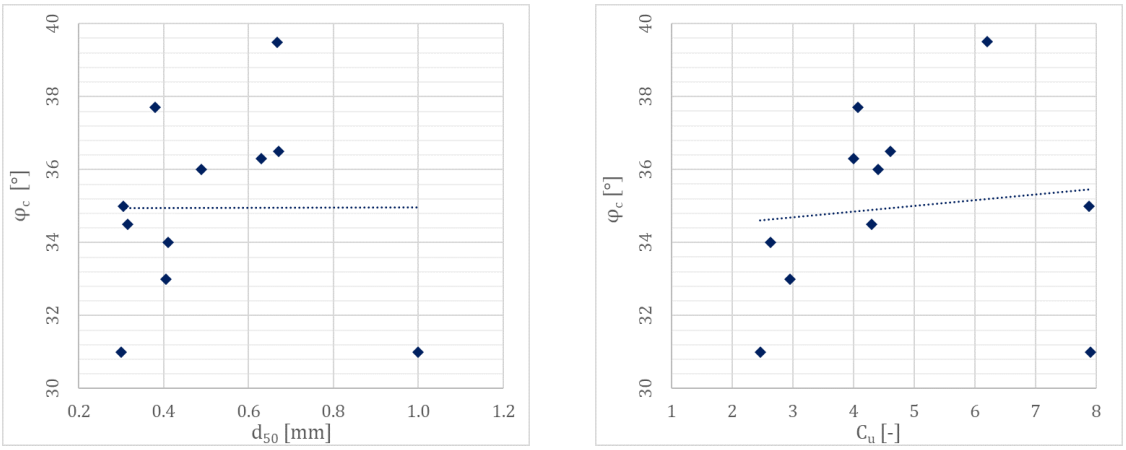

(A) (B)

FIGURE 4.3: Increase of the critical friction angle φ_c with the grain size (A) and the coefficient of uniformity (B)

Limit void ratios e_{i0}, e_{d0} and e_{c0}

The void ratios e_{i0} and e_{d0} describe the upper and lower boundary of possible void ratios. The limiting void ratios e_i, e_d and e_c decrease with an increasing mean effective stress p'_s. To guarantee realistic values at zero as well as at very high pressures, Bauer proposed the following equation [30]:

$$\frac{e_i}{e_{i0}} = \frac{e_c}{e_{c0}} = \frac{e_d}{e_{d0}} = \exp\left[-\left(\frac{3 \cdot p_s}{h_s}\right)^n\right] \tag{4.2}$$

As depicted in Figure 4.4, the void ratios reach the limit values e_{i0}, e_{c0} and e_{d0} at zero mean skeleton pressure and they asymptotically approach zero for a very high p'_s.

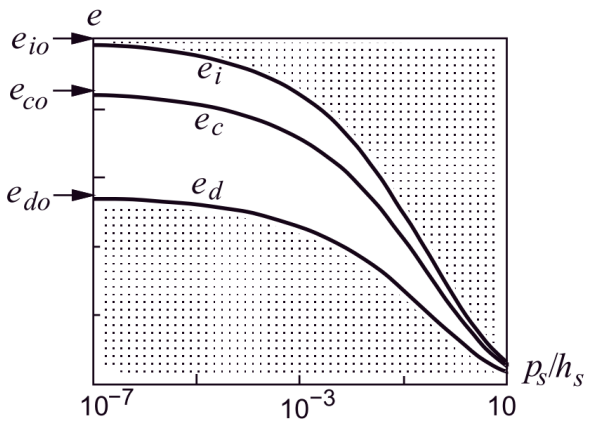

FIGURE 4.4: Relation between e_i, e_c, e_d and p_s. The gray area designates the inapplicability of the hypoplastic model. [31]

The parameter e_{i0} defines the largest possible void ratio at zero grain pressure. Theoretically, a void ratio of e_{i0} is reached during isotropic consolidation of a grain suspension

in the moment, when a grain skeleton is formed. Experimentally determining this parameter is close to impossible but it can be calculated for idealized grain skeletons. If identical spheres are arranged in a regular array, the maximum possible void ratio is 0.91 [31]. For the identical glass spheres the value of e_{max} was determined to lie between 0.72 and 0.77 in experiments. By comparing the maximum theoretical value of $e_{i0} = 0.91$ with the values measured in experiments the ratio of $e_{i0}/e_{max} \approx 1.20$ is defined. Herle [29] proposed to approximate e_{i0} from e_{max} with $e_{i0} = 1.15 \cdot e_{max}$.

The value e_{d0} describes the minimum void ratio at zero grain pressure. It is assumed that the most effective way to densify a granular material is to load the specimen with cyclic shearing with small amplitude under constant pressure. According to Herle and Gudehus [31], the value e_{d0} is close to the minimum void ratio e_{min} determined with standard tests like the one described in DIN 18126. Hence, the relation $e_{d0} \approx e_{min}$ is assumed [29].

The critical void ratio e_{c0} is the third void ratio needed for the hypoplastic model and the second parameter related to the critical state. Since it is defined at zero pressure, no direct measurement is possible. Herle und Gudehus [31] observed that e_{c0} is approximately equal to the void ratio at the loosest state e_{max}. During the standard e_{max}-test, sand is poured into a mold from very small falling height. The sample undergoes large shear deformations at very low pressures which corresponds to an almost critical state.

If the granulate hardness h_s, exponent n together with a single value of e_d at p_s are known, all three void ratios can also be calculated from Equation 4.2. As an example, the equation for e_{d0} is mentioned below:

$$e_{d0} = e_d \cdot exp\left[-\left(\frac{3 \cdot p_s}{h_s}\right)^n\right] \tag{4.3}$$

Herle writes that the void ratios e_d, e_c and e_i mainly depend on non-uniformity and the grain shape [29]. The void ratios are supposed to decline with the increase of C_u because the voids between bigger grains are filled with smaller grains. Figure 4.5 shows the results of the analysis of the calcareous sands from the KELLER-database. The graph shows that only e_c and e_i notably decrease whereas e_d stays more or less constant even though C_u increases from 2.46 to 7.91.

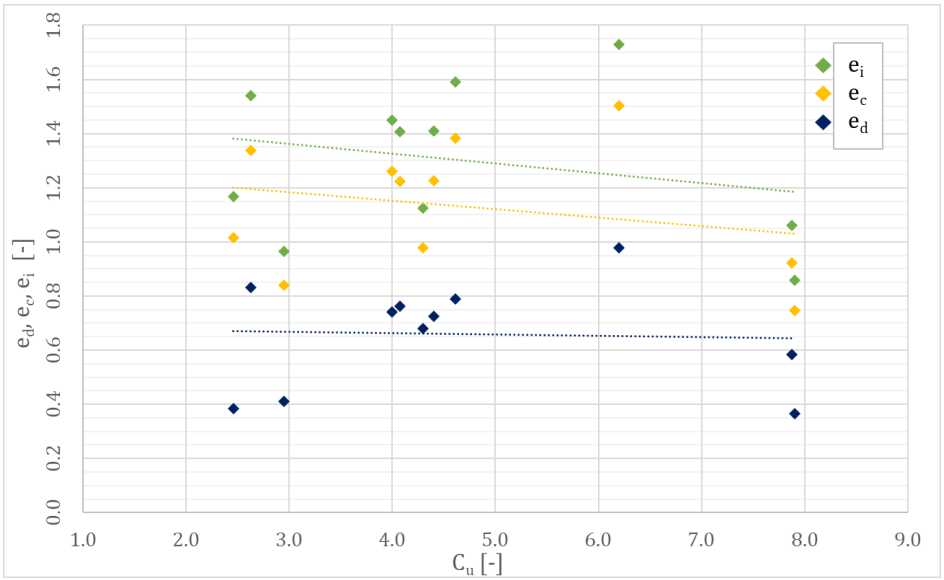

FIGURE 4.5: Relationship between e_d, e_c, e_i and C_u

It is also stated that the void ratios increase with the angularity of the sand grains [29]. As mentioned in Chapter 1, the investigated sands are all calcareous sands which are made up from sea-shells, coral lumps and other skeletal remains of marine organisms whose shape differs a lot from silica sand particles. Especially the angular shape of sea-shells, which favors the occurrence of big voids and the porous skeletons of corals contribute to the increase of the void ratios. For these reasons it is assumed that the carbonate content is an indirect measure of the angularity of the grains. Figure 4.6 proves that there is a significant increase of the void ratios associated with the increase of the carbonate content.

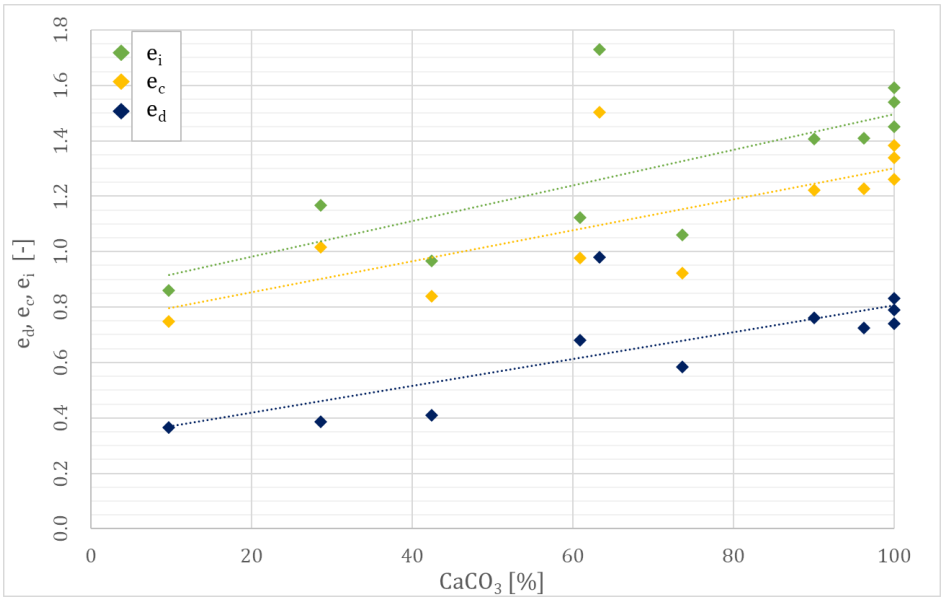

FIGURE 4.6: Relationship between e_d, e_c, e_i and the carbonate content

Granulate hardness h_s and exponent n

The granulate hardness h_s is used as a reference pressure and, although the name might suggest otherwise, it must not be confused with the hardness of single grains. The magnitude of h_s is primarily influenced by the grain-size, -shape, -material and -size distribution [29]. Exponent n governs the pressure sensitivity of the grain skeleton which means it allows for a non-proportional increase of the incremental stiffness with an increasing mean skeleton pressure p'_s.

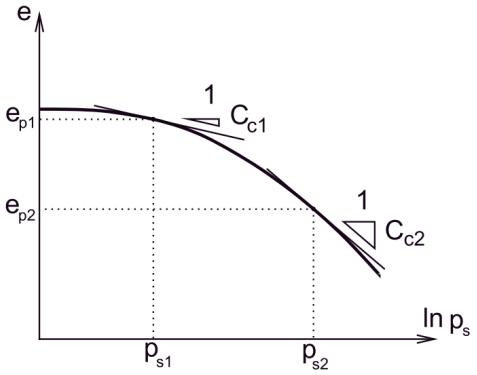

FIGURE 4.7: Determination of n for a stress range between p_{s1} and p_{s2} [31]

The determination of the granulate hardness h_s and exponent n can be done by performing a proportional compression test on an initially very loose sand sample. Proportional compression describes a linear stress-path starting at zero pressure. Since the isotropic triaxial compression test is quite laborious, it is usually substituted with a much simpler oedometer test. However, it is not easy to install a sample with a void ratio of $e = e_{max}$ in the oedometer's ring as even striking off the surface will already cause the sample to slightly compact. According to Herle [32], small deviations of the experimental initial void ratio do not influence the shape of the measured curve and are therefore acceptable.

With a pressure range from p_{s1} to p_{s2}, the corresponding void ratios e_{p1} and e_{p2} and compression indices C_{c1} and C_{c2} (Figure 4.7), exponent n can be calculated with the following equation:

$$n = \frac{\ln\left(\frac{e_{p1} \cdot C_{c2}}{e_{p2} \cdot C_{c1}}\right)}{\ln\left(\frac{p_{s2}}{p_{s1}}\right)} \tag{4.4}$$

After the calculation of n, h_s can be derived with the equation mentioned below:

$$h_s = 3 \cdot p_s \cdot \left(\frac{n \cdot e_p}{C_c}\right)^{\frac{1}{n}} \tag{4.5}$$

As Equations 4.4 and 4.5 show, n can be calculated independently of h_s whereas the knowledge of n is necessary for the determination of h_s. To show the influence of the parameters h_s and n on the shape of compression curves, Figure 4.8 compares curves calculated with varying qualitative h_s and n values. Exponent n reflects the curvature of the curve and h_s the slope of it.

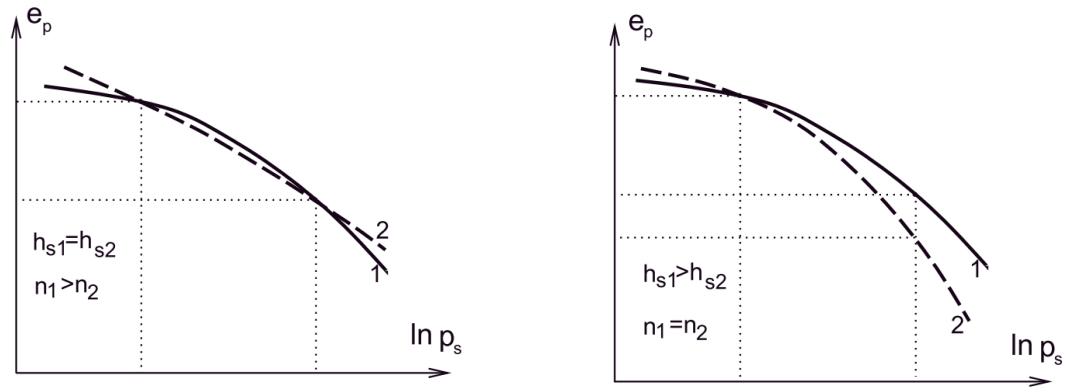

(A) (B)

FIGURE 4.8: Influence of the parameters h_s (A) and n (B) on the shape of the compression curve [29]

Herle [29] states that the granulate hardness h_s decreases with an increase of the compressibility. This behavior can also be seen in the graph in Figure 4.8 (B). The compression curve of material 2 with the smaller h_s-value is steeper, which corresponds to a higher compressibility. Based on the KELLER-database of calcareous sands, the influence of the grain size on the compressibility and, hence, the granulate hardness h_s and exponent n was examined. Figure 4.9 depicts the influence of the mean grain size d_{50} on h_s and n for the sand samples from previous KELLER projects.

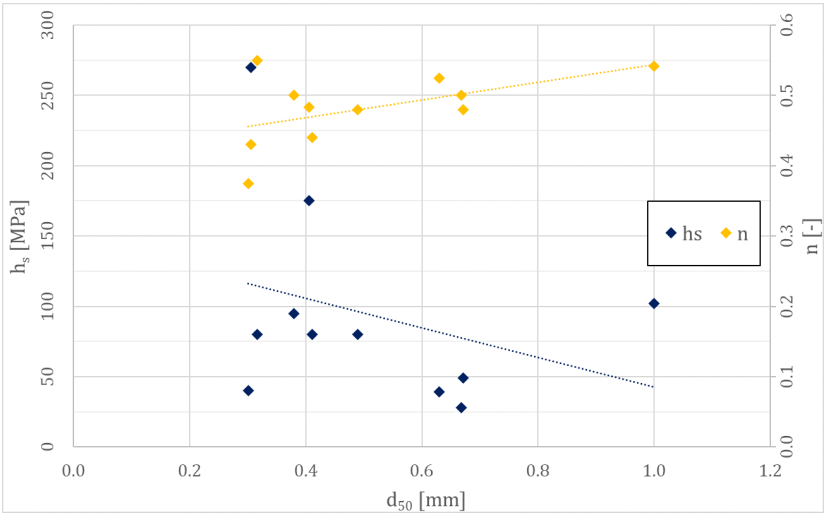

FIGURE 4.9: Influence of the mean grain size d_{50} on the parameters h_s and n

An increasing grain size lowers the compressibility because larger grains are more susceptible to crushing [33]. It is also assumed that the compressibility is affected by the

mineralogy of the sand. The main mineral in calcareous sand is calcite or aragonite (both $CaCO_3$) which only reaches a value of 3 on Mohs' scale of hardness whereas the mineral SiO_2, main component of silica sands, reaches a value of 7.

Figure 4.10 compares the compression curves resulting from four high-pressure oedometric compression tests on dense and loose samples. To ensure a potential grain fracturing does occur during the test and to record its effects, the oedometer tests were performed with a maximum vertical stress of $\sigma'_{v,max} = 25$ MPa. Besides considering possible grain fracturing, high-pressure oedometric tests are also necessary because the hypoplastic constitutive equation has to be calibrated for a comparable pressure range as obtained in the actual CPTs [16]. Even though the requirements of a simple grain skeleton do not allow grain fracturing, its effects can indirectly be incorporated in the hypoplastic model with the parameters h_s and n this way.

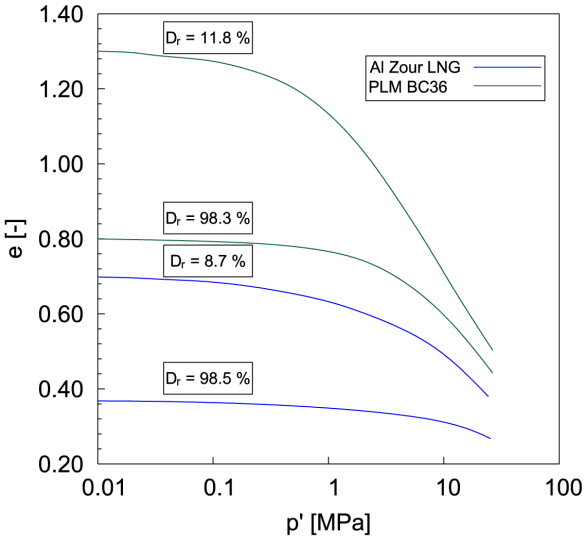

FIGURE 4.10: Comparison of two compression curves resulting from high-pressure oedometer tests [34]

Table 4.2 lists the granulometric properties which were found to have the biggest influence on the parameters h_s and n [31]. As can be seen in Figure 4.10, the compression curve of sample BC36 is steeper than the curve of the LNG-sample, which corresponds to the lower value of h_s. According to Herle and Gudehus, exponent n depends strongly on the coefficient of uniformity C_u and the mean grain size d_{50}. They found that n increases with decreasing C_u and increasing d_{50}. For the granulate hardness h_s, they found that an increasing value of d_{50} will cause a decline of h_s. While the relation between n and C_u could not be confirmed, the influence of d_{50} on n and h_s was confirmed for the sand samples in the KELLER-database (Figure 4.9).

TABLE 4.2: Comparison between the granulometric parameters of the sand samples from the PLM BC36- and Al Zour LNG-project [34]

Material	$CaCO_3$ [%]	C_u	d_{50} [mm]	h_s [MPa]	n
BC36	100	4.61	0.671	49	0.480
LNG	9.73	7.91	1.00	102	0.542

Exponent α

Exponent α controls the influence of the relative void ratio r_e on the peak friction angle φ_p. During shearing of a dense sand sample at a constant mean pressure, the friction angle will increase to a peak friction angle ($\varphi_p > \varphi_c$). The difference between φ_p and φ_c increases with the pressure-dependent relative void ratio r_e [32]. Exponent α controls the peak friction angle of the material and hence, also the dilatancy behavior [16].

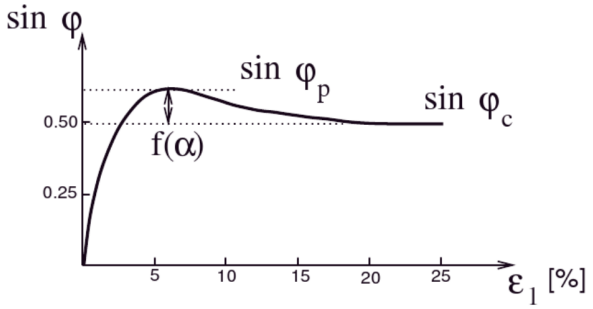

FIGURE 4.11: Exponent α controls the relation between φ_p and φ_c [35]

The exponent α is determined by performing a triaxial test on a dense sample and considering the peak state. According to Herle and Gudehus, the peak friction angle φ_p decreases with increasing C_u, grain sphericity and with decreasing mean grain size d_{50} for a constant pressure and density [31].

Figure 4.12 compares the stress-strain curves of two different sand samples taken from previous KELLER projects. Since the focus of this investigation lies on the influence of the carbonate content on the hypoplastic parameters, the two samples with the lowest and the highest $CaCO_3$-value were compared to each other. The sand sample from box BC36 at the PLM project consists of 100 % calcium carbonate whereas the carbonate content of the sample from the Al Zour LNG project is only 9.73 %.

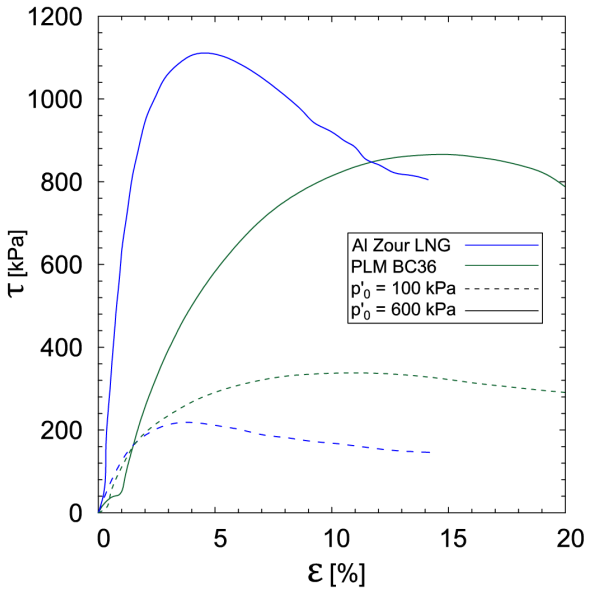

FIGURE 4.12: Comparison of two stress-strain curves showing different dilatant behavior depending on granulometric properties [34]

The Al Zour LNG sample shows a much more distinct dilatant behavior than the BC36 sample which ultimately leads to a lower value of α. As can be seen in Table 4.3, this is in accordance with the findings of Herle and Gudehus saying that the peak friction angle φ_p and therefore the dilatancy angle, decreases with increasing C_u and decreasing mean grain size d_{50}.

TABLE 4.3: Comparison between the granulometric parameters of the sand samples from the PLM- and Al Zour LNG-project [34]

Material	$CaCO_3$ [%]	φ_c [°]	C_u	d_{50} [mm]	α
BC36	100	35.5	4.61	0.671	0.045
LNG	9.73	31.0	7.91	1.00	0.095

Exponent β

The stiffness of a grain skeleton with a void ratio of $e < e_c$ can be adjusted via the exponent β. Figure 4.13 shows that the compression curve is flatter for a higher β-value. The magnitude of this influence strongly varies with the initial void ratio of the sample in the oedometer. The curves in the left graph were calculated for a loose sample (high initial e) and show a much smaller difference than the curves in the right graph which were calculated for a dense sample (low initial e). β plays an important role for dense soils, meaning only if the void ratio e is substantially lower than e_i. β can be determined from oedometric compression tests by calculating the ratio of the stiffness moduli at two different void ratios (dense and loose) but at the same pressure. This pressure T_1 is denoted on the x-axis on Figure 4.13 and represents the vertical stress in the oedometer.

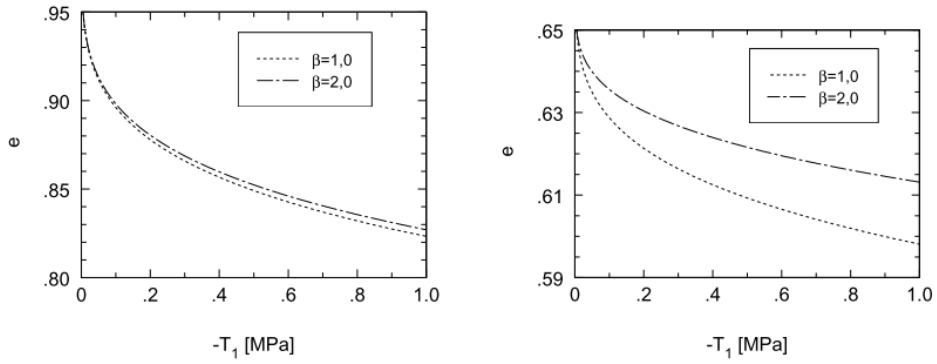

FIGURE 4.13: Influence of exponent β on calculated one-dimensional compression curves simulated for a loose (left) and dense (right) sample [29].

$$\beta = \frac{\ln\left(\beta_0 \cdot \frac{E_2}{E_1}\right)}{\ln\left(\frac{e_1}{e_2}\right)} \tag{4.6}$$

Usually, E increases proportionally with the decrease of the void ratio e at the same pressure. Herle and Gudehus [31] conducted several experiments to determine the influence of granulometric properties on the value of exponent β and concluded that, as an estimate or when lacking experimental data, it is usually sufficient to assume $\beta = 1$.

4.2.3 Conclusion on the hypoplastic parameter determination

As stated in Chapter 4.2.1, the hypoplastic model by „von Wolffersdorff" [25] is only valid for a simple grain skeleton. A simple grain skeleton presumes that the grains are indestructible meaning that abrasion and/or crushing of the sand particles is not considered. However, calcareous sands have a high tendency to grain fracturing which raises the question, how a hypoplastic equation can accommodate that behavior. In an attempt to answer this question, Meier examined the use of the KIM in calcareous sands in his dissertation *Application of Hypoplastic and Viscohypoplastic Constitutive Models for Geotechnical Problems* [16]. On the one hand he writes that further research about the applicability of a hypoplastic constitutive model on materials with a tendency to grain fracturing is necessary to make an educated statement. On the other hand he demonstrated that the Karlsruhe Interpretation Method works well for a material containing breakable grains, if an accurate calibration of the hypoplastic model parameters is possible [16].

The procedure of determining the hypoplastic parameters with calcareous sands is mostly the same as for silica sands, except for the oedometer test. In order to achieve a high accuracy of the KIM and to include the effects of potential grain crushing in the results, the hypoplastic constitutive equation has to be calibrated for a comparable

pressure range as obtained in the actual CPTs. Therefore, the maximum vertical pressure σ_v should be at least 25 MPa. Other than that, no extra measures are necessary.

Table 4.4 lists 4 calcareous sands from the KELLER-database and 4 silica sands found in literature. In general, the parameters showing the biggest differences are the ones which are connected to the compressibility of the sand. The granulate hardness h_s, for example, shows the biggest differences. It is assumed that this is caused by the mineralogy of silica sands. Exponent n is connected to h_s and tends to be higher in calcareous sands implying that the compression curves are steeper. The critical friction angle φ_c and the limit void ratios tend to be higher in calcareous sands as well.

TABLE 4.4: Comparison between the hypoplastic parameters of calcareous and silica sands [29]

Material	$CaCO_3$ [%]	φ_c [°]	e_{d0}	e_{c0} [-]	e_{i0}	h_s [MPa]	n	α [-]	β
calcareous sands									
Al Zour LNG	9.73	31	0.37	0.75	0.86	102	0.542	0.095	1.43
Al Zour Package 5	42.45	33	0.41	0.84	0.97	175	0.483	0.13	1.74
JAT4: Island	60.93	34.5	0.68	0.98	1.12	80	0.550	0.15	1.2
PLM - BC36	100	36.5	0.79	1.38	1.59	49	0.48	0.045	1.40
silica sands									
Toyoura	-	30	0.61	0.98	1.10	2600	0.27	0.18	1.00
Karlsruhe	-	30	0.28	0.53	0.84	5800	0.28	0.13	1.03
L. Buzzard	-	31	0.49	0.79	0.94	6400	0.45	0.16	1.00
Ticino	-	31	0.59	0.94	1.11	250	0.68	0.11	1.00

A Table listing all hypoplastic parameters for all the samples in the KELLER-database can be found in Appendix B.1.

4.3 The cavity expansion theory

The cavity expansion theory is a way to study the changes in stress, pore-water pressures and displacements caused by the expansion of cylindrical or spherical cavities in soil or rock. It serves as a useful and simple geomechanical tool for modeling complex geotechnical problems. It has therefore been applied widely in the areas of interpreting in-situ soil testing results, load-bearing behavior of pile foundations, tunnels and underground excavations and borehole stability in the petroleum industry.

Unlike many laboratory tests, CPTs are indirect tests meaning that the measured data needs to be interpreted to obtain the desired soil properties. Due to the similarity of the deformations caused by the expansion of a cavity and the penetration of a cone, the

cavity expansion theory has been used with considerable success in the interpretation of CPT data.

Bishop et al. [36] were the first to outline the analogy between cavity expansion and cone penetration in 1945 when they aimed to solve problems of metal indentation. It was observed that the pressure required to produce a deep hole in an elastic-plastic medium was proportional to the pressure necessary to expand a cavity of the same volume under the same conditions. This means that in its origins, the cavity expansion theory was already studying a penetration process but a penetration process in metal which, in comparison to soil, is a less complex material. The state-dependent behavior of soil including dilatancy or contractancy of a granular skeleton complicate the use of cavity expansion in soil mechanics. Gibson and Anderson introduced the theory to geotechnical engineering in 1961 [37]. Based on a cylindrical cavity expansion, they developed a method to estimate soil properties from pressuremeter tests. More and more researchers started taking a closer look at the connection between the limit pressure of a cavity expansion and the cone resistance and proposed relations between the two. In 1977, Vesić related the cone resistance from a CPT to the limit pressure of a spherical cavity expansion. However, Vesić did not account for dilation in his solution making his approach incapable of modeling cone penetration in medium dense to very dense sands where dilation is significant. Salgado presented a correlation which applies a stress rotation analysis to connect the cone resistance with a cylindrical cavity limit pressure in 1997 [38]. The soil behavior in Salgado's research was modeled by an elastic-perfectly plastic constitutive law with a non-associated Mohr-Coulomb yield condition.

This chapter will explain the theoretical background of the spherical cavity expansion and explain its role in the Karlsruhe Interpretation Method.

4.3.1 Spherical cavity expansion

The simulation of the penetration of a cone in sand with the spherical cavity expansion theory is based on the assumption that the soil around a cone more or less deforms in the shape of a sphere. Cavity expansion in soil is a one-dimensional boundary value problem which is solved by applying the principles of continuum mechanics. To describe the stress-strain behavior of the soil, a constitutive model is needed. The cavity expansion theory does not require a certain soil model but can be carried out in any model capable to describe soil behavior adequately [39]. From the available soil models the most appropriate one has to be chosen according to the nature of the problem and the required accuracy. Cudmani and Osinov [40] numerically solved the boundary value problem of the spherical cavity expansion with the use of a hypoplastic constitutive equation calibrated to the soil under investigation (Chapter 4.2). Since all soils in Cudmani's research can be classified as sands, the hypoplastic constitutive equation proposed by von Wolffersdorff [25] was chosen as the most adequate one.

The actual simulation model is built up of two concentric spheres with differing initial radii r_{a0} and r_{b0}, where $r_{a0} < r_{b0}$. Sphere A expands quasi-statically and symmetrically inside of sphere B which represents the adjacent soil and is the outer boundary at

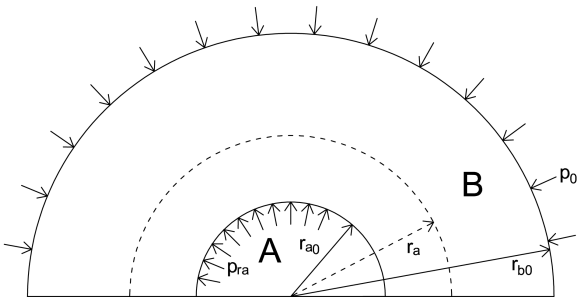

FIGURE 4.14: Schematic depiction of the spherical cavity expansion, adapted from Uhlig [41]

the same time. To make sure the model size does not interfere with the results of the simulation, the radius of sphere B is taken as $r_{b0} \gg r_{a0}$. If the change of the circumferential stress p_θ at the outer boundary r_b is small, the outer radius is deemed large enough [42]. The calculations of Cudmani and Osinov showed that an increase of r_a of 100% leads to a less than 0.1% variation in the circumferential stress p'_θ at r_b when $r_{b0}/r_{a0} \geq 30$ for loose and $r_{b0}/r_{a0} \geq 90$ for dense soils [42]. As the expansion of sphere A progresses with a constant velocity, sphere B is loaded with the initial mean effective stress p'_0 which is kept constant during the simulation. For a series of simulations, p'_0 is chosen to represent a pressure range from low to high and does not depend on the soil properties. While sphere B is subjected to the constant mean effective pressure p'_0, the radial pressure p'_{ra} in sphere A increases with the continuing expansion until the radial and circumferential stress, p'_{ra} and p'_θ, and the void ratio e approach limit values that correspond to the critical state of the soil. For a given soil, these limit values depend on the initial state governed by the initial mean effective stress p'_0 and the initial relative density D_r (or e_0).

The relative density is calculated with the following formula:

$$D_r = \frac{e_{max} - e}{e_{max} - e_{min}} \tag{4.7}$$

As Cudmani writes in his dissertation [5], the lower boundary void ratio e_d and the critical void ratio e_c strongly depend on the pressure in the grain skeleton. Since Equation 4.7 does not consider the pressure dependence of the limit void ratios, it may not be appropriate for the characterization of density if a wide pressure range is considered [43], [44]. In the context of the theory of hypoplasticity, a pressure-dependent relative density I_D^* employing the pressure-dependent limit void ratios e_c and e_d is more adequate to describe the state of a cohesionless soil:

$$I_D^* = \frac{e_c - e}{e_c - e_d} \tag{4.8}$$

Detailed information is given in *Theoretical investigation of the cavity expansion problem based on a hypoplasticity model* [42] where the numerical algorithm is also described in detail.

Results of a series of spherical cavity expansions from $r_{a0} = 1$ to $r_{a0} = 3.3$ which were perfomed by Cudmani and Osinov [42] are shown in figure 4.15. These simulations were carried out for a variety of relative densities with a hypoplastic model calibrated to Ticino sand and with an initial pressure p'_0 of 100 kPa. The radial pressure p_r, the circumferential pressure p_θ and the void ratio e at the cavity wall are shown as functions of the cavity radius r_a. With an increasing ratio between r_a and r_{a0}, the radial and circumferential pressure component increases and monotonically approaches its limit value corresponding to the critical state of the soil. Cudmani [5] states that for practical applications, the expansion ratio of $r_a \approx 2 \cdot r_{a0}$ for loose and $r_a \approx 3 \cdot r_{a0}$ for dense soil is sufficient to reach the limit pressures.

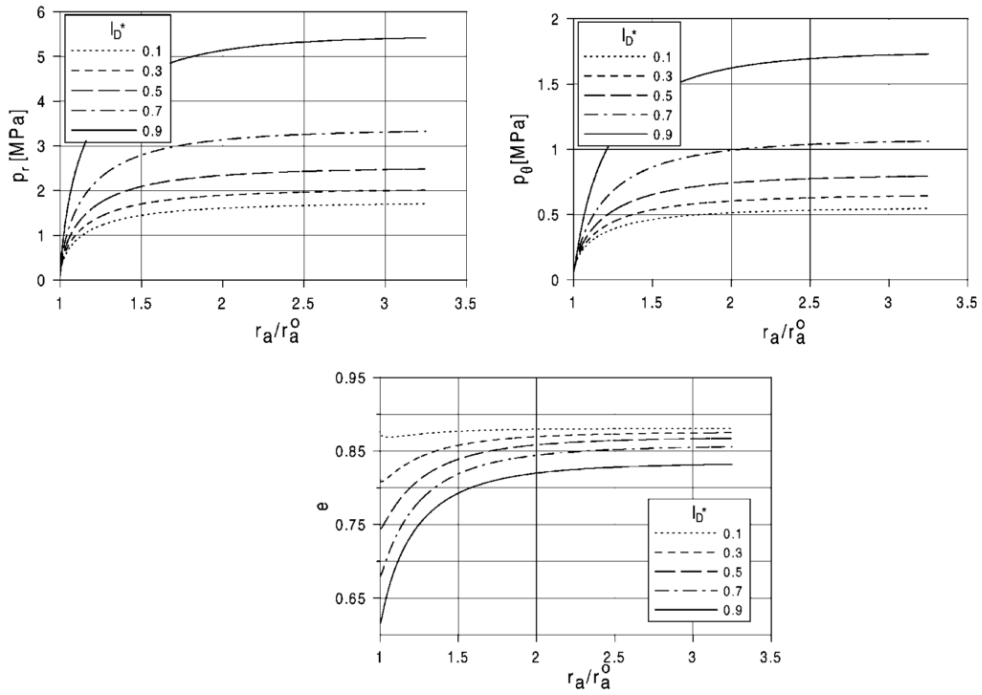

FIGURE 4.15: Progression of the pressures p_r and p_θ and the void ratio e during a spherical cavity expansion with $p'_0 = 100$ kPa [42]

The void ratio e and the deviatoric stress $q' = (p'_r - p'_\theta)/2$ at the cavity wall are plotted against the mean pressure $p' = (p'_r + 2 \cdot p'_\theta)/3$ in Figure 4.16 (A) and (B). The lines labeled e_c and e_d in Figure 4.16 (A) correspond to the limit void ratios from the hypoplastic model. As can be seen, both of these values decline with an increasing pressure p following Equation 4.2 proposed by Bauer [30]. The straight line in Figure 4.16 (B) represents the critical-state line which is defined by $q'/p' = sin\varphi_c$. As can be seen, the deviatoric stress q' approaches its limit value much faster in loose soil because the corresponding initial void ratio e_{init} is closer to its critical value e_c than in dense soil. The dashed line in Figure 4.16 represents a soil in a dense state and it is evident that the critical state is reached at a much higher pressure p than in the loose soil. Figure 4.15 and 4.16 (A) show an increase of the void ratio e with a continuous expansion of the cavity and an increasing mean pressure p' which reveals that the ground is actually loosening during the spherical cavity expansion. This behavior is related to dilatancy of the soil.

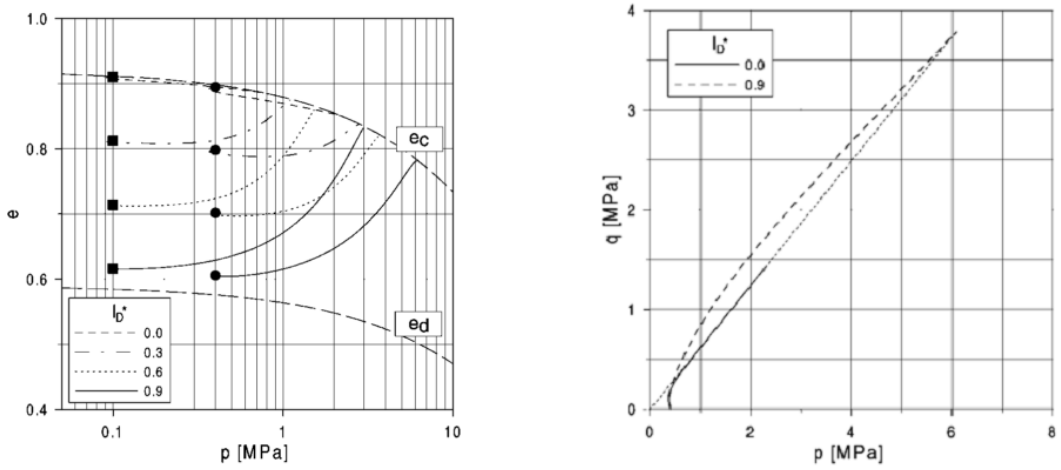

(A) (B)

FIGURE 4.16: Development of the void ratio e (A) and the $q-p$ path for an initial pressure of $p_0' = 0.4$ MPa (B) for the expansion of a spherical caviy in Ticino sand [42]

Plotting the radial limit pressure p_{LS} as a function of the initial pressure p_0 and the initial relative density I_D^* for Ticino sand reveals the final connection between the limit pressure p_{LS} and the cone resistance q_c. The similarity between the curves shown in Figure 4.17 and the resulting curves from cone penetration tests in calibration chambers is indisputable, which confirms that the limit pressure and the cone resistance depend on the initial state of the soil in the same manner. The initial state is defined by the initial stress p_0' and the relative density I_D^*.

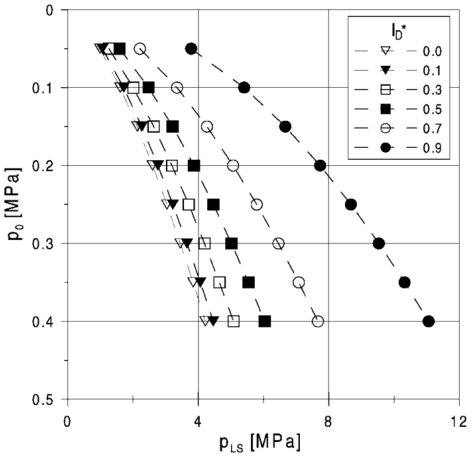

FIGURE 4.17: The limit pressure p_{LS} for a spherical cavity expansion versus the initial pressure p_0 for different initial relative densities I_D^* calculated for Ticino sand [42]

Cudmani solved the SCE problem for nine different sands; five silica and four carbonate sands. The results show that the mineralogical composition of the sands has a big influence on the magnitude of the limit stress p_{LS}. Figure 4.18 (A) and (B) shows the curves resulting from Cudmani's investigation for $I_D^* = 0.9$. At an initial pressure p_0

of 0.4 MPa, the limit stress p_{LS} in silica sands ranges from ∼9.60 MPa to ∼14.80 MPa whereas in carbonate sands it only ranges from ∼4.20 MPa to ∼7.20 MPa. This is consistent with the results of CPTs performed in calibration chambers with carbonate sands which also produce lower cone resistances.

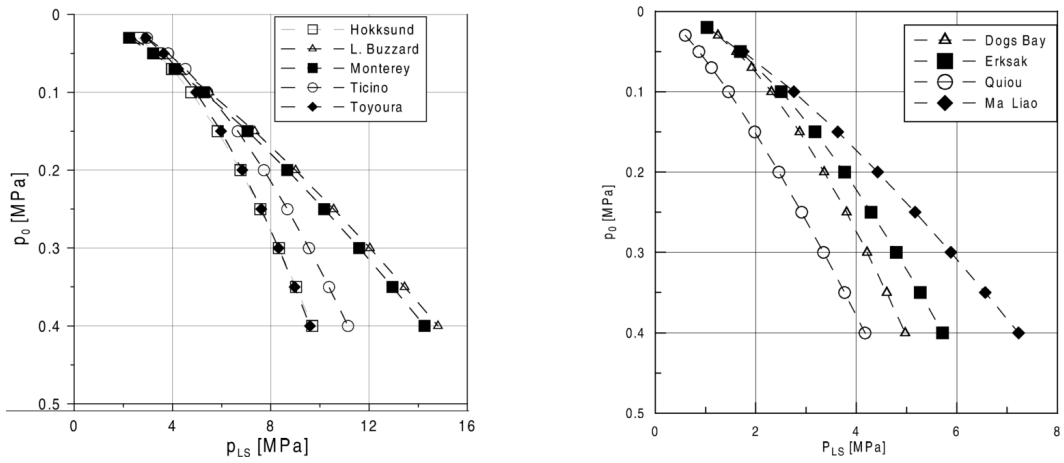

(A) (B)

FIGURE 4.18: Limit pressure p_{LS} vs. initial pressure p_0 for silica (A) and carbonate (B) sands and a relative density of $I_D^* = 0.9$ [5]

After Cudmani and Osinov [40] solved the SCE-problem for the five different silica sands and various initial conditions, they found that the radial limit pressure p_{LS} as a function of the initial state can be approximated by the equation:

$$p_{LS} = a \cdot p_0^b \tag{4.9}$$

where p_0 is the initial mean pressure and a and b are given by:

$$a = a_1 + \frac{a_2}{a_3 + I_D^*} \qquad \textit{and} \qquad b = b_1 + \frac{b_2}{b_3 + I_D^*} \tag{4.10}$$

Performing a series of SCE-simulation will result in a set of curves showing the dependency of p_{LS} on the relative density and p_0. Figure 4.19 shows a set of curves calculated by the geotechnical laboratory in Germany for the PLM sample. Every dot on the graph represents one solution of the spherical cavity expansion with a certain pressure-dependent relative density I_D^* and a certain initial pressure p_0. The lowest I_D^* was 0% and was successively increased in steps of 10% to a maximum value 100%. For each I_D^*-value, the simulation was run 5 times amounting to a total of 50 simulations. From the resulting curves, the a_i- and b_i-parameters are found by means of simple curve fitting.

Finally, Table 4.5 lists four calcareous sands from the KELLER-database and four silica sands found in literature [5]. A clear difference between the various a_i- and b_i-parameters for calcareous and silica sands is not as obvious as it is for the hypoplastic

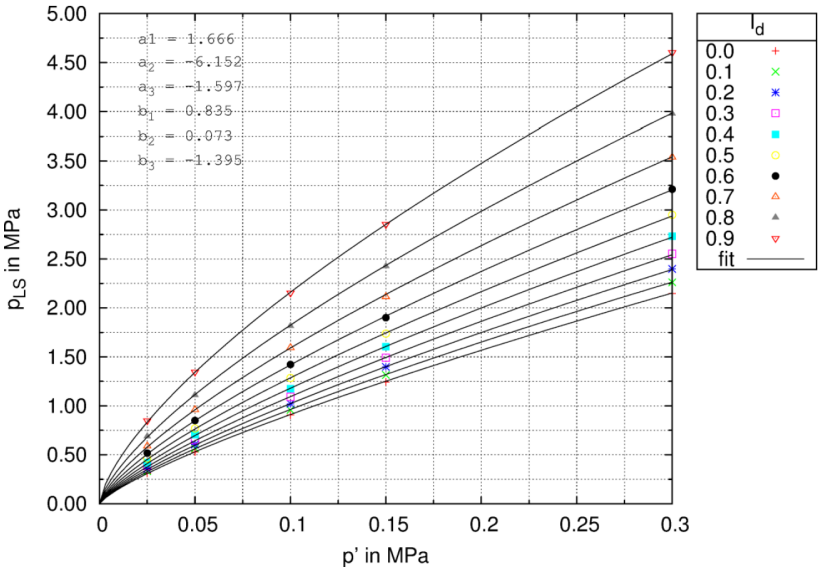

FIGURE 4.19: Exemplary curves resulting from a series of 50 SCE-simulations based on the PLM AZ28 sample [34]

variables. A slight difference is observed in the average value of a and b which is related to the different mineralogical and granulometric characteristics of carbonate and silica sands. To investigate the influence of the a_i and b_i-parameters on the results of the KIM in detail, a sensitivity analysis was conducted. The results are presented in Chapter 5 of this thesis.

TABLE 4.5: Comparison of the KIM-parameters obtained from the SCE performed on different calcareous and silica sands [5], [16]

Material	$CaCO_3$	a_1	a_2	a_3	a	b_1	b_2	b_3	b
				calcareous sands					
Al Zour LNG	9.73	1.526	-6.299	-1.370	9.707	0.826	0.062	-1.232	0.728
Al Zour Pack. 5	42.45	0.185	-8.795	-1.276	13.195	0.879	0.103	-1.248	0.720
JAT4: Island	60.93	-0.246	-13.140	-1.996	9.167	0.871	0.136	-1.343	0.688
PLM - BC36	100	2.550	-4.477	-1.544	7.293	0.841	0.060	-1.460	0.771
average					9.841				0.727
				silica sands					
Toyoura	-	1.944	-6.814	-1.439	10.066	0.807	0.161	-1.377	0.600
Ticino	-	3.055	-6.686	-1.355	11.911	0.794	0.133	-1.379	0.623
Karlsruhe	-	1.132	-8.529	-1.774	8.398	0.824	0.140	-1.406	0.651
L. Buzzard	-	1.704	-8.777	-1.229	15.658	0.920	0.087	-1.319	0.799
average					11.508				0.668

4.4 The shape factor k_q

Strictly speaking, the deformation caused by the expansion of a spherical cavity does not exactly correspond to the deformation caused by the penetration of a cone in sand. However, as explained in the last chapter, the development of the limit pressure shows the same dependence on the initial density and stress as the cone resistance. Cudmani proposed to connect the cone resistance q_c with the limit pressure p_{LS} by introducing the so-called shape factor k_q which leads to Equation 4.11. The shape factor was determined by comparing results of cone penetration tests in large calibration chambers on nine different sands with the limit pressures obtained by solving SCE problems for the same soils, same initial pressure p_0 and same initial density.

$$q_c = k_q \cdot p_{LS} \rightarrow k_q = \frac{q_c}{p_{LS}} \tag{4.11}$$

Figure 4.20 shows the dependence of the shape factor on the density I_D^* for four different pressure ranges: a) $p_0' < 0.05$ MPa, b) $0.05 < p_0' < 0.15$ MPa, c) $0.15 < p_0' < 0.25$ MPa and d) $0.25 < p_0' < 0.50$ MPa. Cudmani showed that k_q varies between 2 and 6 and is not influenced by p_0' [5]. The continuous line in the graphs of Figure 4.20 represents the mean value of k_q and is approximated by the following equation:

$$k_q = 1.5 + \frac{5.8 \cdot (I_D^*)^2}{(I_D^*)^2 + 0.11} \tag{4.12}$$

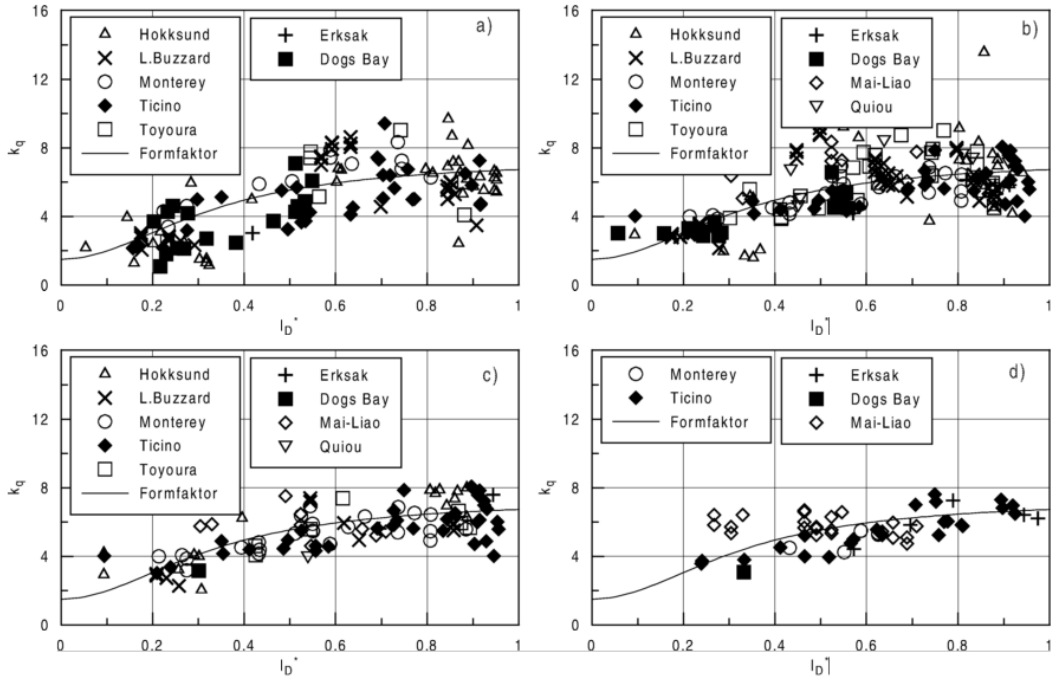

FIGURE 4.20: Shape factor k_q versus the pressure-dependent relative density I_D^* for four different pressure ranges [5]

According to Cudmani, this approximation has been determined for a pressure range from $p_0 = 0.03$ MPa to $p_0 = 0.5$ MPa, a range of I_D^* from 0 to 1 and a granulate hardness h_s between 50 MPa and 10000 MPa [5]. However, that doesn't necessarily mean that Equation 4.12 is not valid for values beyond these limits. Cudmani has shown that his method also delivers satisfactory results for materials with a lower granulate hardness than 50 MPa. Figure 4.21 shows two graphs which compare the measured and the calculated values of q_c for Dog's Bay ($h_s = 30$ MPa) and Mai-Liao sand ($h_s = 32$ MPa) with a tolerable accordance of the two q_c-values.

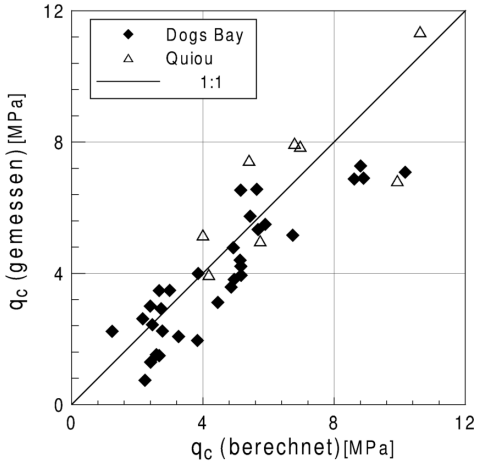

FIGURE 4.21: Comparison of calculated (KIM) and measured (CCT) cone resistance values for two calcareous sands [5]

In addition to the two calcareous sands, Dogs Bay and Quiou, shown in Figure 4.21, Cudmani also compared the measured q_c-values of five silica sands to the q_c-values calculated with the shape factor and limit pressure. Figure 4.22 shows the graphs for Monterey and Ticino sand and proves that these values show good accordance as well. In total, Cudmani reports that about 85% of the compared values deviate less than 25% from the straight line representing a 1:1 agreement. This is seen as proof that the shape factor can establish an adequate correlation between the calculated radial limit pressure p_{LS} and the measured cone resistance q_c [5].

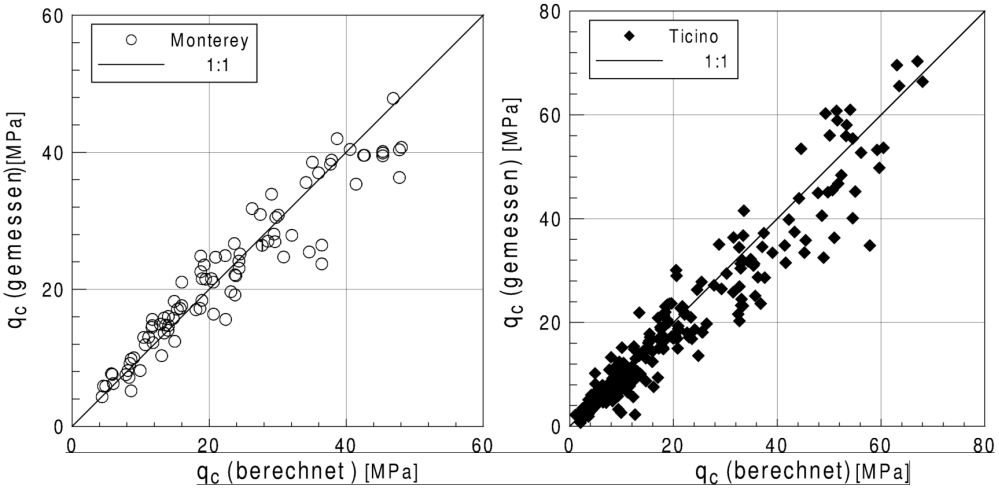

FIGURE 4.22: Comparison of calculated (KIM) and measured (CCT) cone resistance values for two silica sands [5]

The shape factor introduced by Cudmani is based on calibration chamber tests (CCTs) performed on nine different sands of which only two are carbonate sands. This leads to the question whether the shape factor differs for calcarous sands or not. To establish a connection between the measured cone resistance q_c and limit stress p_{LS} in fine-grained soils, Uhlig [41] has performed CCTs on a clay and a silt and solved the corresponding spherical cavity expansion problems to establish the associated shape factor. It is therefore assumed that by performing a number of calibration chamber tests on a variety of carbonate sands and simulating the corresponding spherical cavity expansion to establish a shape factor for carbonate sands, might increase the accuracy of the KIM-results.

4.5 The KIM equation

The previous chapters summed up all factors that go into the KIM-equation. Combining all the formulas of these factors leads to the final KIM-equation. Note that in the equations given below, the pressure-dependent density I_D^* is exchanged with the relative density D_r. I_D^* is used in the hypoplastic model to explain the pressure-dependency of the limit void ratios (Figure 4.4). For practical applications of the KIM it is sufficient to apply the relative density D_r [16] which will also be used in the equations from here on.

In its simplest form the equation only has two components, the shape factor k_q and the limit stress p_{LS} from the solution of the spherical cavity expansion:

$$q_c = k_q \cdot p_{LS} \tag{4.13}$$

Chapter 4.3.1 explained the determination of the limit pressure and its parameters a_i and b_i. The shape factor k_q was introduced in Chapter 4.4:

$$q_c = \left(1.5 + \frac{5.8 \cdot D_r^2}{D_r^2 + 0.11}\right) \cdot \left(a \cdot p_0^b\right) \tag{4.14}$$

$$a = a_1 + \frac{a_2}{a_3 + D_r} \qquad \textit{and} \qquad b = b_1 + \frac{b_2}{b_3 + D_r} \tag{4.15}$$

$$p_0' = \left(\frac{1}{3} \cdot \sigma_v' \cdot (1 + 2 \cdot K_0)\right) \tag{4.16}$$

Adding the formulas for the a and b parameters and the mean effective stress p_0 to the equation leads to the final form which allows to calculate the cone resistance q_c for any desired relative density D_r:

$$q_c = \left(1.5 + \frac{5.8 \cdot D_r^2}{D_r^2 + 0.11}\right) \cdot \left(a_1 + \frac{a_2}{a_3 + D_r}\right) \cdot \left(\frac{1}{3} \cdot \sigma_v' \cdot (1 + 2 \cdot K_0)\right)^{\left(b_1 + \frac{b_2}{b_3 + D_r}\right)} \tag{4.17}$$

4.6 Results of the KIM

After the results of all the steps explained in the previous chapters are obtained, the Karlsruhe Interpretation Method can be applied for two different investigations. First, for a given initial state defined by the relative density D_r and the initial pressure p_0, the cone resistance q_c can be calculated. The second application involves the solution of the inverse problem and calculate the relative density of a soil based on results obtained from a CPT.

In the first case, the result of the KIM will be a curve showing the development of the q_c-values over depth like the one shown in Figure 4.23. A curve like this, calculated for the required relative density, can be used in the design process of a project and help set the grid-spacing of the compaction points. In the second case, the in-situ relative density can be back-calculated from q_c-values measured in the field which will result in a graph showing the progression of the relative density over the depth.

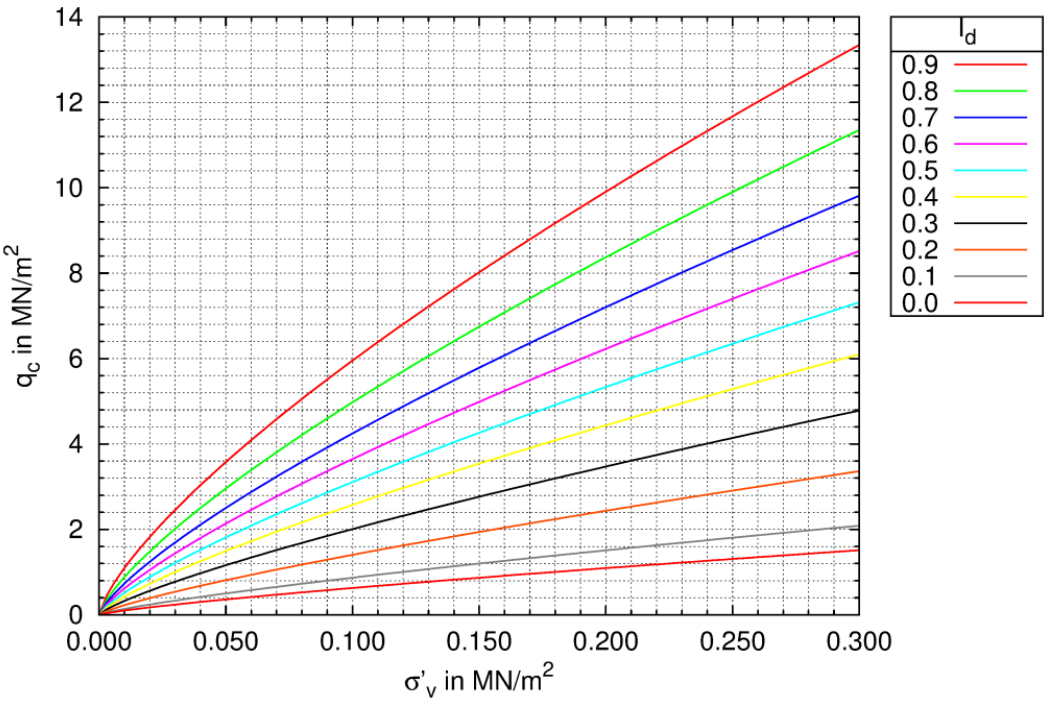

FIGURE 4.23: Exemplary q_c-curves for the PLM BC36 sample calculated by the geotechnical laboratory [34]

5 The KIM applied on the KELLER database

5.1 Introduction

After the introduction to the theoretical background of the Karlsruhe Interpretation Method, Chapter **??** will investigate the influence of the particularities of calcareous sands on the results of the KIM. It is assumed that the cone resistances computed by means of the KIM decrease with an increasing carbonate content of the sand and that therefore, the carbonate content of a soil can serve as an indicator for the magnitude of the cone resistance. This hypothesis will be tested in this chapter by investigating the impact of the input parameters on the result and how these parameters are connected to the carbonate content of the sand.

With the Karlsruhe Interpretation Method, the cone resistance q_c is calculated with the following equation:

$$q_c = k_q(D_r) \cdot p_{LS}(p'_0, D_r) \qquad with \qquad p_{LS} = a \cdot p'^b_0 \tag{5.1}$$

Parameters a and b are determined by means of curve fitting after the solution of a series of spherical cavity expansion problems and p'_0 is the effective initial mean pressure representing a certain soil-state. Chapter 4.3.1 gives a detailed insight into the procedure of the spherical cavity expansion to determine a and b and the determination of p'_0 is described in Chapter 5.2. Together with the effective mean pressure p'_0, parameters a and b form the limit pressure p_{LS} in Equation 5.1. First, the determination of p'_0 and its influence on the limit pressure will be explained. Then, the a_i and b_i parameters, their connection to the soil parameters and carbonate content and their respective influence on the result of p_{LS} will be elaborated. Finally, the influence of the limit pressure p_{LS} on the cone resistance will be shown and the results of this investigation will be summarized.

To ensure a good level of comparability, the cone resistance was calculated for the same relative density and depth for all samples in the database. Densification requirements are usually given in relative density D_r or percentage of the maximum dry density $\%MDD$. The usual requirements range from 60% to 70% for the relative density and 90% to 95% MDD. In this investigation, a target relative density of $D_r = 60\%$ and a representative depth of 10 m was chosen for the exemplary calculations.

In addition to graphs in which the connections between the various parameters are visualized, the correlations will also be quantified with correlation coefficient R. The correlation coefficient R measures the linear relationship between two variables and gives an indication of the strength of the relationship. The correlation coefficient R ranges from -1 to $+1$, where $+1$ indicates the strongest positive relationship and -1 the strongest possible negative relationship. A positive relationship between two variables means that for every increase in one variable, there is an increase in the other one as well whereas a negative relationship means that for every decrease in one variable, the other one decreases as well. The closer R is to 0, the weaker the relation between the two variables. In this study, R will mainly be used to describe the connection of the various input parameters with the carbonate content of the corresponding sand sample.

5.1.1 Sand database of KELLER

Over the last couple of years, KELLER Grundbau has sent samples from 8 different projects to a soil mechanics laboratory in Germany to have basic soil-, the hypoplastic and the KIM-parameters determined. By always sending the samples to the same geotechnical laboratory, a constant high quality and consistency of the results is ensured. All of these samples can be classified as calcareous sands and exhibit a carbonate content ranging from 9.73% to 100%. In cooperation with KELLER, Meier [16] performed chamber calibration tests and determined the hypoplastic parameters on a calcareous sand from Dubai. This material, named M100, is also added to the database making it a total of 11 different sands for which the basic soil properties, the hypoplastic and the KIM-parameters are known. Based on this material-library, one goal of the following chapters is to explore the effect of the carbonate content of a sand on the input parameters for the KIM-equation and in further consequence, on the results of the Karlsruhe Interpretation Method. Table 5.1 gives an overview of the basic properties of all investigated sand samples in the KELLER-database.

5.2 The effective mean pressure p'_0

As was shown in Chapter 4.5, the KIM-equation consists of the shape factor k_q and the limit pressure p_{LS}. The shape factor is only dependent on the relative density but the limit pressure is defined by the mean effective pressure p'_0 and the KIM-parameters a_i and b_i (with $i = 1, 2, 3$). Since the value of p'_0 is calculated with the vertical effective stress σ'_v and the coefficient of lateral earth pressure K_0, it directly depends on the basic four soil properties e_{min}, e_{max}, φ_c and ρ_s. Knowing which parameters go into the calculation of p'_0 and understanding the influence they have on the result, allows to make an estimation of the magnitude of p'_0 and get a rough idea about the subsequently calculated limit pressure p_{LS}. Therefore, the next chapters will investigate the role of each of the parameters involved in the calculation of p'_0 and explain its influence on the results. To be able to find out how the composition of the material influences the results, the connection of each computed parameter to the carbonate content of the soil will also be investigated. However, the carbonate content is not a direct input

parameter of the equation. Therefore, the influence of it on the results of the KIM has to be found by considering the connections established in Chapter 3.3.

The calculation steps were carried out for every project in the database to a depth of 10 m and a relative density of 60%. For a better comprehensibility, the results are spread across several tables listing the results for every project.

Table 5.1 confirms the findings in Chapter 3.3. All soil parameters show a tendency to increase with an increasing carbonate content in the soil. The maximum values are displayed in bold and the minimum values in italic.

TABLE 5.1: The KELLER-database of calcareous sands and their basic properties

Material	$CaCO_3$ [%]	e_{min} [-]	e_{max} [-]	φ_c [°]	ρ_s [g/cm^3]
Al Zour LNG	9.73	*0.365*	*0.747*	*31*	2.663
Sheikh Jaber CW	28.6	0.385	1.015	31	*2.650*
Al Zour Package 5	42.45	0.410	0.840	33	2.670
JAT4: Island	60.9	0.680	0.977	34.5	2.749
JAT4: South Side	63.3	**0.979**	**1.504**	**39.5**	2.777
Palm Jumeirah	73.6	0.583	0.922	35	2.741
M100 Dubai sand	90	0.762	1.223	36	2.805
Palm Deira	96.2	0.725	1.226	36	2.800
PLM - AZ28	100	0.740	1.261	36.3	2.791
PLM - BC36	100	0.790	1.384	36.5	2.791
Zakkum Island	100	0.831	1.338	34	**2.833**

Judging from theses soil properties, it is expected that the maximum value of the vertical effective pressure σ'_v at a depth of 10 m will be calculated for the Al Zour LNG sample and the minimum value will result from the JAT 4: South Side material.

5.2.1 Calculation steps

The mean effective stress p'_0 is an important factor of the KIM-equation as it incorporates basic soil parameters in the form of the vertical effective stress σ'_v and the coefficient of lateral earth pressure K_0. To understand how each of the parameters listed in Table 5.1 enters the calculation sequence, the necessary calculation steps will be explained with the aid of the respective formulas. p'_0 is calculated with the following equation:

$$p'_0 = \left(\frac{1}{3} \cdot \sigma'_v \cdot (1 + 2 \cdot K_0)\right) \qquad with \qquad \sigma'_v = \gamma \cdot z \tag{5.2}$$

The coefficient of lateral earth pressure can be calculated with the formula proposed by Jaky [45] for normally consolidated soils:

$$K_0 = 1 - sin\,(\varphi_c) \tag{5.3}$$

The effective vertical stress is determined by multiplying the unit weight of the soil with the depth. Depending on if the desired depth is above or below the groundwater table, either the bulk unit weight γ or the buoyant unit weight γ' is applied. The calculation of these two values requires knowing the in-situ void ratio e which is a measure of the density of the soil. Since the relative density has been set to $D_r = 60\%$, the in-situ void ratio e_{Dr} at the required relative density is calculated as follows:

$$D_r = \frac{e_{max} - e_{Dr}}{e_{max} - e_{min}} \rightarrow e_{Dr} = e_{max} - D_{r,req} \cdot (e_{max} - e_{min}) \tag{5.4}$$

After the void ratio at the target D_r-value has been determined, the dry density ρ_d corresponding to that value has to be computed. The grain density ρ_s and the previously determined e_{Dr} are used in the equation listed below:

$$\rho_{d,Dr} = \frac{\rho_s}{1 + e_{Dr}} \tag{5.5}$$

Together with an assumed moisture content of $w = 20\%$ assumed for all projects and the gravitational acceleration g, this density value is then employed to calculate the bulk unit weight γ:

$$\gamma_{Dr,req} = (1 + w) \cdot \rho_{d,Dr} \cdot g \tag{5.6}$$

Finally, the bulk unit weight $\gamma_{Dr,req}$ is utilized in the calculation of the vertical effective stress σ'_v which, subsequently is used to determine the mean effective stress p'_0. In case the desired depth is below the groundwater table it is necessary to calculate the buoyant unit weight γ'. The calculation of γ' requires knowing the density of the saturated soil below the groundwater table ρ_{sat} first.

$$\rho_{sat} = \frac{\rho_s + (e_{Dr} \cdot \rho_w)}{1 + e_{Dr}} \tag{5.7}$$

With that value determined, it is possible to calculate the buoyant unit weight γ':

$$\gamma' = \rho_{sat} \cdot g - \gamma_w \tag{5.8}$$

It is noted here, that the assumed moisture content in Equation 5.6 might be too high for the climatic conditions in the UAE and can be lowered to a more appropriate value. Lowering the value of w will lower the mean effective stress p'_0 and ultimately also lead to lower q_c-value resulting from the KIM.

5.2.2 Void ratios e_{min} and e_{max} and grain density ρ_s

The void ratio at the target relative density e_{Dr} is calculated with Equation 5.4 for which, aside from the required relative density, the limit void ratios are input parameters. Since the values of e_{min} and e_{max} tend to increase with the content of $CaCO_3$, the calculated value for e_{Dr} also shows a tendency to increase. Therefore, it is no surprise that the sample from JAT 4: South Side, which exhibits the highest values of e_{min} and e_{max} in the database also shows the highest in-situ void ratio of $e_{Dr} = 1.189$ for a relative density of 60%. This value is then applied in Equation 5.5 to derive the dry density corresponding to the required relative density. Having the highest value of e_{Dr}, the calculations for the JAT 4: South Side material result in the minimum values of the dry density and the unit weight of 1.269 g/cm^3 and 15.22 kN/m^3, respectively. The sample from the Al Zour LNG site on the other hand shows the lowest values of e_{min} and e_{max} and therefore results in the highest dry density and unit weight in the database. 1.755 g/cm^3 and 21.05 kN/m^3, respectively. Since every calculation step leading up to the bulk unit weight is affected by the results of the preceding equation, the void ratios e_{min} and e_{max} influence every result from the beginning on.

The carbonate content of a soil only correlates with the soil properties but it is not the actual cause of, for example, the increase of the limit void ratios. This is the reason why the material with the highest carbonate content does not automatically show the highest value of e_{Dr} or the lowest unit weight γ_{Dr}. The in-situ void ratio calculated for the targeted relative density and the bulk unit weight γ however, are connected by a causal relationship. That means that the material with the lowest in-situ void ratio will also be the material that results in the highest dry density and unit weight. That statement is proven true by the sand sample retrieved from the Al Zour LNG project which, in addition to the lowest carbonate content of 9.73%, also exhibits the lowest value of the in-situ void ratio of $e_{Dr} = 0.518$.

Analogous to the void ratios, an increase of the grain density ρ_s of a calcareous sand is connected to an increase the carbonate content. In combination with the void ratio e_{Dr}, the grain density ρ_s is used for the computation of the dry density at the required relative density $\rho_{d,Dr}$ with Equation 5.5. In contrast to the void ratios, increasing the grain density would cause the dry density to increase as well and lead to rising values of the unit weights γ and γ'. However, ρ_d is not only a function of ρ_s but also of the in-situ void ratio e_{Dr} which, as its value increases, causes the value of the in-situ density $\rho_{d,Dr}$ to decrease. The calculated dry densities of samples with a high grain density like the Zakkum Island, PLM AZ28 and BC36 material, all result in the lower spectrum of the database. This data suggests that the effect of the limit void ratios e_{min} and e_{max} outweighs the influence of the grain density in the calculation of the dry density and the subsequently derived unit weights γ and γ'. An explanation for that

might be the differences in the ranges of the parameters. As Table 5.2 shows, there's a significant difference between the maximum and minimum values of e_{min} and e_{max} in the database whereas the grain density values only show a small spread.

TABLE 5.2: Differences between the maximum and minimum values of e_{min}, e_{max} and ρ_s in the database

		MIN	MAX	Δ [%]
minimum void ratio	e_{min}	0.365	0.979	168.22
maximum void ratio	e_{max}	0.747	1.504	101.34
grain density	ρ_s [g/cm^3]	2.650	2.833	6.89

The projects are listed in an increasing order of their carbonate content to ease the identification of a possible pattern connecting the parameters. Again, the maximum values are displayed in bold and the minimum values in italic.

TABLE 5.3: Results of density and unit weight calculations for the materials in the KELLER-database of calcareous sands for $D_r = 60\%$

Material	$CaCO_3$ [%]	e_{Dr} [-]	$\rho_{d,Dr}$ [g/cm^3]	γ_{Dr} [kN/m^3]	σ'_v [kPa]
Al Zour LNG	9.73	*0.518*	**1.755**	**21.05**	210.54
Sheikh Jaber CW	28.6	0.637	1.619	19.43	194.29
Al Zour Package 5	42.45	0.582	1.688	20.25	202.53
JAT4: Island	60.9	0.799	1.528	18.34	183.39
JAT4: South Side	63.3	**1.189**	*1.269*	*15.22*	152.23
Palm Jumeirah	73.6	0.719	1.595	19.14	191.39
M100 Dubai sand	90	0.946	1.441	17.29	172.94
Palm Deira	96.2	0.925	1.454	17.45	174.51
PLM - AZ28	100	0.948	1.432	17.19	171.90
PLM - BC36	100	1.028	1.377	16.52	165.18
Zakkum Island	100	1.034	1.393	16.72	167.16

Figure 5.1 displays the influence of the void ratio e_{Dr} (A) and the grain density ρ_s (B) on the mean effective pressure p'_0. As expected, there is an inverse relationship between e_{Dr} and the subsequently calculated p'_0 meaning that an increasing in-situ void ratio e_{Dr} causes the mean effective pressure to decrease. The coefficient of correlation for the $p'_0 - e_{Dr}$ graph was calculated to be R = -0.9853 which indicates a very strong negative correlation between the two variables. It is noted that, in contrast to what the graph in Figure 5.1 (B) suggests, the decline of the mean effective pressure is not caused by an increase of the grain density. The much wider range of the limit void ratios e_{min}

and e_{max} outweighs the influence of the grain density in the course of the calculation of the mean effective pressure p'_0 which is why the value of p'_0 decreases even if the grain density increases.

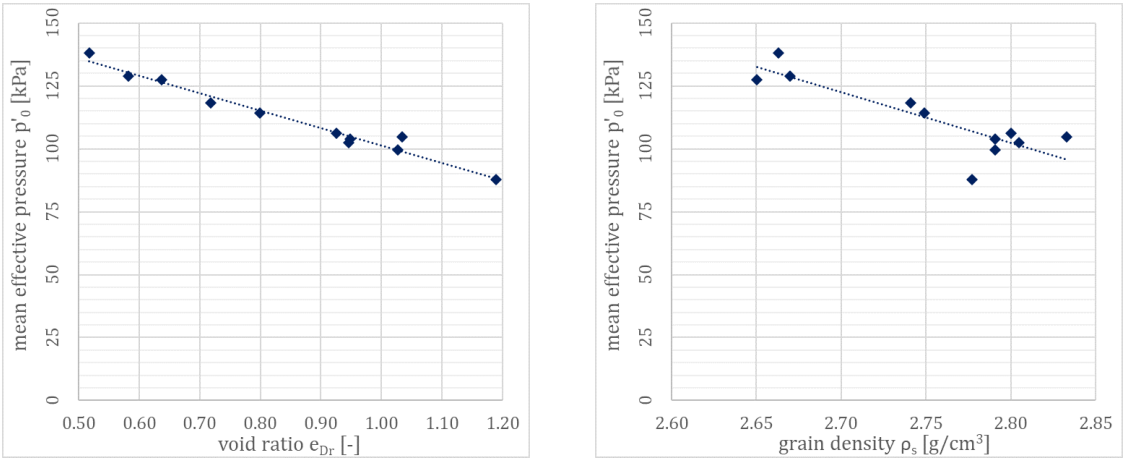

(A) (B)

FIGURE 5.1: Relationships between mean effective pressure p'_0 and the void ratio e_{Dr} (A) and the grain density ρ_s (B)

Aside from influencing the result of the KIM through the mean effective stress, the limit void ratios also affect it through the spherical cavity expansion. As parameters $e_{min} = e_{d0}$, $e_{max} = e_{c0}$ and $e_{i0} = 1.15 \cdot e_{max}$ of the hypoplastic constitutive equation they control the mechanical behavior of the soil during the SCE-simulation.

5.2.3 Critical friction angle φ_c

The critical friction angle φ_c is employed in Equation 5.3 to calculate the coefficient of lateral earth pressure K_0. The value of the Sinus-function steadily increases for the range of φ_c in the KELLER-database from 31° to 39.5°, lowering the resulting coefficient of lateral earth pressure. Together with the vertical effective pressure σ'_v, this coefficient is then used in Equation 5.2 to derive the mean effective stress p'_0. As explained in Chapter 3.3, there is a positive correlation between φ_c and the content of $CaCO_3$ meaning that K_0 will be lower in a sand that contains a high amount of carbonate.

The highest critical friction angle of $\varphi_c = 39.5°$ in the database was determined on the sample from the JAT 4: South Side project. Therefore, this material also shows the lowest coefficient of lateral earth pressure of $K_0 = 0.364$. Besides already resulting in the lowest bulk unit weight in the database, this is another reason why the mean effective pressure at a depth of 10 m in this material is the lowest of all materials and only $p'_0 = 87.69$ kPa. The example on the other side of the range is, again, the Al Zour LNG sand. The critical friction angle in this sand was tested to be $\varphi_c = 31°$ which results in $K_0 = 0.485$ and ultimately in a mean effective pressure of $p'_0 = 138.25$ kPa.

Results of a short exemplary calculation to show the impact of a high value of φ_c are summed up in Table 5.4. To maintain comparability, the mean effective pressure p'_0 was calculated for a vertical stress of $\sigma'_v = 10$ kPa for both materials. It is shown that throughout the database, the critical friction angle φ_c increases by 27.42% leading to a decrease of K_0 of 24.95 % and a subsequent decrease of the mean effective pressure p'_0 of 12.33%.

TABLE 5.4: Effect of a high φ_c on the mean effective stress p'_0 calculated for $\sigma'_v = 10$ kPa

		Al Zour LNG	JAT4: South Side	Δ [%]
critical friction angle	φ_c [°]	31	39.5	27.42
lateral earth pressure	K_0	0.485	0.364	-24.95
mean effective pressure	p'_0 [kPa]	6.57	5.76	-12.33

Figure 5.2 displays the influence of the critical friction angle on the mean effective pressure p'_0. As the correlation coefficient of R = -0.9226 indicates, p'_0 is negatively correlated to an increasing value of φ_c meaning that an increasing critical friction angle will cause a decrease of the value of mean effective pressure p'_0.

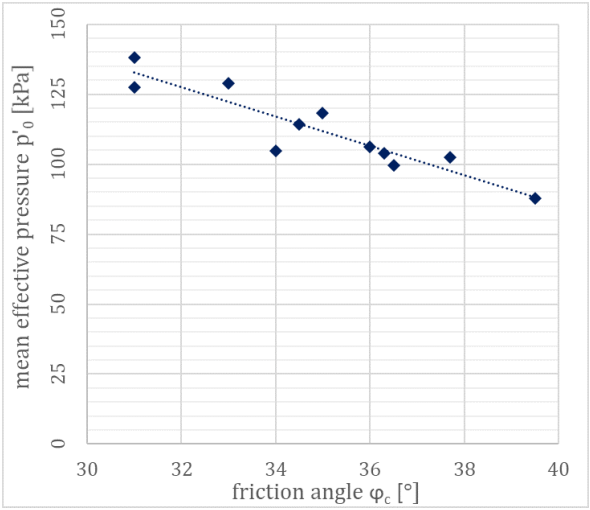

FIGURE 5.2: Influence of the critical friction angle φ_c on the mean effective pressure p'_0

Just like the limit void ratios, the critical friction angle does not only influence the result of the KIM through the mean effective pressure. It is also one of the eight hypoplastic parameters governing the mechanical behavior of the soil in the simulation of the spherical cavity expansion. However, establishing a connection between the hypoplastic parameters and the values of a_i and b_i resulting from the SCE has proved to be a challenge. A more detailed explanation of this problem will be given in a later section.

5.2.4 Influence of the mean effective pressure p'_0 on the limit pressure p_{LS}

After the unit weight γ has been calculated for each project, the vertical and the mean effective stress were computed over a depth of 10 m. The progression of the mean effective pressure for all investigated projects is shown in Figure 5.3. Continuing the trend, the parameters determined on the Al Zour LNG sample lead to the highest values of p'_0 whereas the soil properties of the JAT 4: South Side sample lead to the lowest p'_0-values. That might suggest that the same trends will also occur in the calculation of the limit pressure p_{LS}. However, that calculation step needs the six parameters a_i and b_i (with $i = 1, 2, 3$) and these parameters are not derived from equations but from simulations and subsequent curve-fitting. Therefore, it is more difficult to relate the a_i and b_i parameters to the initial soil parameters. By looking at the results of the p_{LS}-calculations listed in Table 5.5, it becomes evident that the previous trends for Al Zour LNG and JAT 4: South Side do not continue for the calculation of the limit pressure. The maximum and minimum values of p_{LS} are now calculated for the Al Zour Package 5 and the PLM-BC36 sample, respectively. The reason for that is the aforementioned introduction of the parameters a and b and their impact on the results of the calculation of the limit pressure p_{LS}.

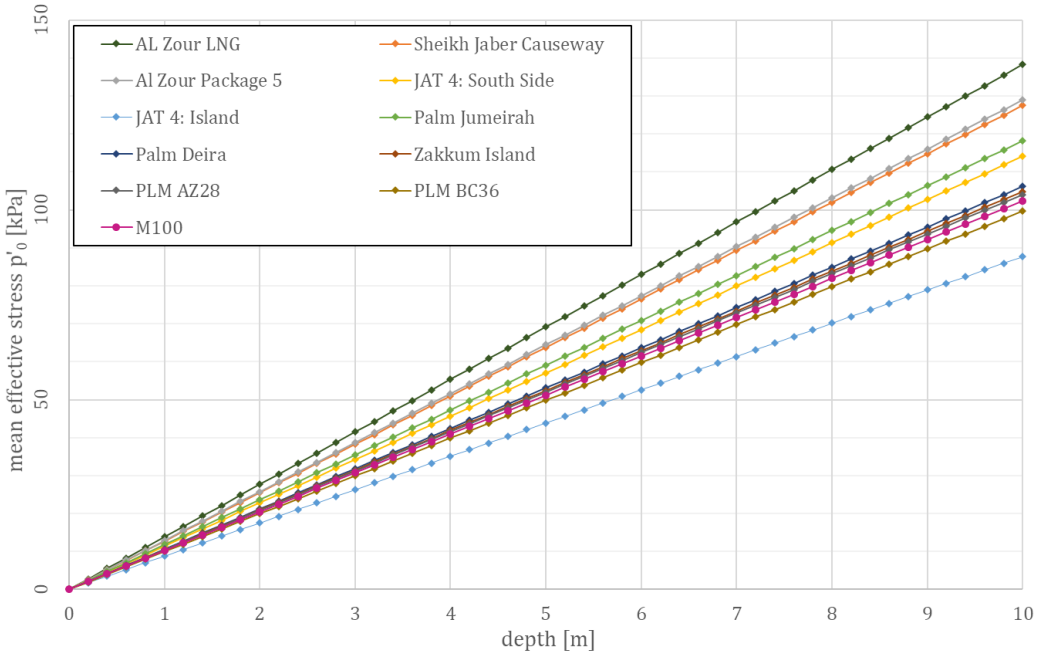

FIGURE 5.3: Development of the mean effective pressure p'_0 over depth

The influence of the mean effective pressure p'_0 on the limit pressure on p_{LS} is plotted in Figure 5.4 (A). It is shown that there is a positive correlation meaning that p_{LS} increases with an increasing value of p'_0. This relationship is also confirmed by the calculated coefficient of correlation of 0.7441 which indicates a good correlation considering p'_0 is not the only input parameter for the calculation of the limit pressure p_{LS}.

TABLE 5.5: Results of stress calculations based on the parameters of the samples in the KELLER-database

Material	$CaCO_3$ [%]	σ'_v [kPa]	K_0 [-]	p'_0 [kPa]	p_{LS} [MPa]
Al Zour LNG	9.73	**210.54**	**0.485**	**138.25**	2.299
Sheikh Jaber CW	28.6	194.27	0.485	127.57	2.602
Al Zour Package 5	42.45	202.51	0.455	128.98	**3.020**
JAT4: Island	60.9	183.39	0.434	114.14	2.060
JAT4: South Side	63.3	*152.24*	*0.364*	*87.69*	1.825
Palm Jumeirah	73.6	191.39	0.426	118.20	1.981
M100 Dubai sand	90	172.93	0.388	102.43	1.580
Palm Deira	96.2	174.51	0.412	106.13	2.143
PLM - AZ28	100	171.89	0.408	104.05	1.458
PLM - BC36	100	165.18	0.405	99.68	*1.233*
Zakkum Island	100	167.16	0.441	104.84	1.593

Figure 5.4 (B) plots the calculated values of p'_0 of each project against the corresponding carbonate content and shows that there is a negative correlation between the two variables. p'_0 decreases with an increasing carbonate content. The associated coefficient of correlation of R = -0.7788 indicates a strong correlation between the percentage of carbonate in the soil and the mean effective pressure p'_0. The behavior plotted in the graph is a logical consequence considering the negative correlations between the carbonate content and the input parameters for p'_0.

5.3 The KIM-parameters a_i and b_i

The six KIM-parameters a_i and b_i are determined by means of curve fitting after performing a series of spherical cavity expansion problems. The constitutive hypoplastic equation used in that simulation is calibrated to the soil of interest and can therefore closely reproduce the behavior of the actual sand on site. For that reason, it is assumed that parameters a_i and b_i must depend in a certain way on the soil properties from which the hypoplastic parameters are derived. However, since neither a_i nor the b_i values are computed with formulas which have actual input parameters with a physical background, it is more difficult to detect the soil properties which influence these values the most. Nevertheless, the influence of these parameters on the cone resistances resulting from the KIM is substantial and will be investigated in the following paragraphs. Like in the previous chapters, the connection between the input parameters and the carbonate content will be assessed. The determination of the hypoplastic

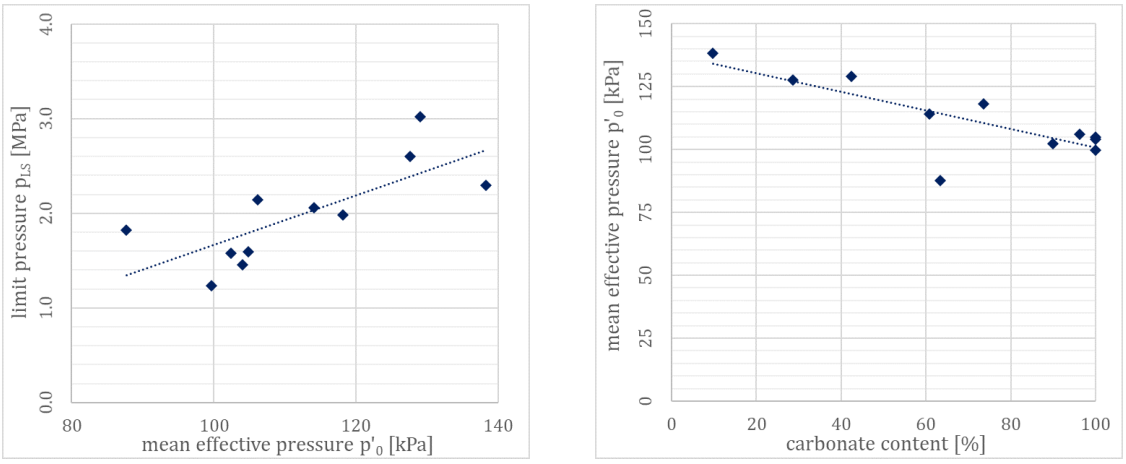

(A) (B)

FIGURE 5.4: The limit pressure p_{LS} plotted against the mean effective pressure (A) and the mean effective pressure p'_0 plotted against the carbonate content (B)

model parameters is explained in Chapter 4.2 and Chapter 4.3.1 gives a detailed insight into the procedure of the spherical cavity expansion. A table listing all the a_i- and b_i-parameters in the database is shown in Appendix C.1.

As a first step, the six a_i and b_i values are employed to calculate the input parameters a and b for the calculation of the limit pressure p_{LS}. Parameters a and b are the result of the following equations:

$$a = a_1 + \frac{a_2}{a_3 + D_r} \qquad b = b_1 + \frac{b_2}{b_3 + D_r} \tag{5.9}$$

Together with the effective mean pressure p'_0, parameters a and b form the limit pressure p_{LS} in the KIM-equation:

$$p_{LS} = a \cdot p'^{b}_0 \tag{5.10}$$

Table 5.6 shows the values of a, b, p'_0, p_{LS} calculated for each project in the KELLER-database. Parameter a is highest for the Al Zour Package 5 sample and material PLM-BC36 exhibits the lowest value of parameter b. These are also the samples that result in the highest and the lowest value of the limit pressure p_{LS} for a relative density of $D_r = 60\%$ and a depth of 10 m.

By looking at the values of a and b it becomes obvious that the values of a are much larger than the values of b. In Equation 5.10, parameter b is the exponent of the mean effective pressure p'_0 which, at the same time is multiplied by parameter a. This suggests that the resulting limit pressure p_{LS} is more sensitive to a variation of b than a variation of a. At the same time, it is assumed that an increase of both of the parameters will also result in an increase of p_{LS}. Figure 5.5 plots the limit pressure p_{LS} against parameter a and b and shows that, while the assumption for parameter a is correct, the limit pressure p_{LS} slightly declines with the increase of parameter b. Since p_{LS} is the product of p'^{b}_0 multiplied by a, the positive correlation between a and

TABLE 5.6: Results of the limit pressure and cone resistance calculations based on the KELLER-database of calcareous sands

Material	$CaCO_3$ [%]	a [-]	b [-]	p'_0 [kPa]	p_{LS} [MPa]
Al Zour LNG	9.73	9.707	0.728	**138.25**	2.299
Sheikh Jaber CW	28.6	9.096	*0.608*	127.57	2.602
Al Zour Package 5	42.45	**13.195**	0.720	128.98	**3.020**
JAT4: Island	60.9	9.167	0.688	114.14	2.060
JAT4: South Side	63.3	8.266	0.621	*87.69*	1.825
Palm Jumeirah	73.6	10.027	0.759	118.20	1.981
M100 Dubai sand	90	*6.936*	0.649	102.43	1.580
Palm Deira	96.2	9.833	0.679	106.13	2.143
PLM - AZ28	100	7.837	0.743	104.05	1.458
PLM - BC36	100	7.298	**0.771**	99.68	*1.233*
Zakkum Island	100	7.953	0.713	104.84	1.593

p_{LS} simply stems from their mathematical relation; a higher value of the multiplier will result in a higher value of the result. Because parameter b is the exponent in $p_0'^b$, a higher value of b should also increase the result of the limit pressure but Figure 5.5 (B) does not show evidence for that. The reason for that is the combination of b and the value of p'_0. Since p'_0 has to be entered in MPa into the equation, its value will remain below 1.0 for most relevant depths. In the projects of the database, p'_0 at a depth of 10 m and a relative density of $D_r = 60\%$, ranges between 0.088 MPa (JAT4: South Side) and 0.138 MPa (Al Zour LNG) whereas parameter b varies between 0.608 and 0.771. Thus, the value resulting from the mean effective pressure p'_0 (<1.0 MPa) raised to the power of b (<1.0) declines with an increase of b for the investigated cases.

The calculated coefficients of correlation for the relationship between a and b and p_{LS} support the results of Figure 5.5 (A) and (B). For the connection between p_{LS} and a the coefficient of correlation amounts to 0.8801 indicating a strong positive correlation. For the relationship between the limit pressure p_{LS} and parameter b, the coefficient is only -0.2789 and thus implies a weak negative connection. An increase of the limit pressure p_{LS} is therefore much stronger connected to an increase of parameter a than to parameter b.

The a_i- and b_i-components of Equations 5.9 are material constants based on curve fitting. Parameters a and b however, depend on the relative density for which the cone resistance is to be determined. As Table 5.7 shows, the values of parameter a vary substantially throughout the database even for a constant value of $D_r = 60\%$.

Given that the equation for a and b is the same, the difference between the variation of the two parameters might be unexpected at first. To understand where this difference comes from, a closer look at the values of a_i and b_i has to be taken. The standard

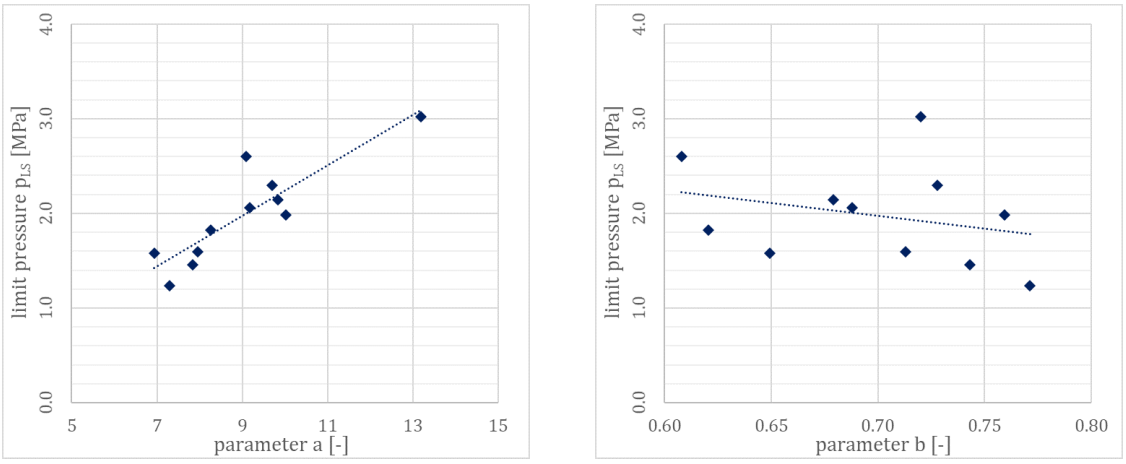

(A) (B)

FIGURE 5.5: The correlation between parameters a (A) and b (B) and the resulting limit pressure p_{LS}

deviation σ calculated for each parameter describes the variation of the various values within the database (see Table 5.7). It can be seen that the standard deviation of the a_i parameters shows much higher values and thus, a much wider spread. Since parameter a is calculated with parameters a_1, a_2 and a_3, this is also the explanation for the larger variation in comparison to parameter b. Due to the high value of the correlation coefficient for the connection between p_{LS} and a and the wider spread of its values, it is assumed that parameter a has a bigger influence on the result of p_{LS} than parameter b and therefore also a bigger influence on the calculated cone resistance q_c.

TABLE 5.7: Statistical parameters of the a_i and b_i values in the KELLER database of calcareous sands

	a_1	a_2	a_3	a	b_1	b_2	b_3	b
minimum	-25.082	-218.502	-7.384	6.936	0.826	0.060	-1.845	0.608
maximum	2.555	-4.477	-1.276	13.195	1.183	0.716	-1.199	0.771
average	-3.706	-46.346	-2.644	9.028	0.924	0.212	-1.422	0.698
median	0.399	-8.528	-1.729	9.096	0.876	0.115	-1.375	0.713
std. deviation σ	10.341	84.413	2.237	1.733	0.122	0.226	0.207	0.054

Aside from the respective values of a_i and b_i, parameters a and b are also influenced by the relative density D_r. To see how the parameters develop with an increasing relative density, a and b were calculated for a range of D_r from 0% to 100% in 10%-increments. Figure 5.6 shows the results of these calculations for the projects Al Zour Package 5 and PLM-BC36, the samples with the highest value of a and the lowest value of b, respectively. The influence of D_r seems to vary strongly with the material but in general it can be said that an increasing relative density leads to an increase of parameter a and a decrease of parameter b. Both reasons for an increase of p_{LS} and therefore q_c. For the Al Zour Package 5 sample, parameter a calculated with D_r =

100% is 352.85% higher than the value calculated with $D_r = 0\%$. The a parameters for PLM BC36 for the same range differ only by 97.72%. Parameter b varies by -41.78% for Al Zour Package 5 and -11.17% for the PLM BC36 sample.

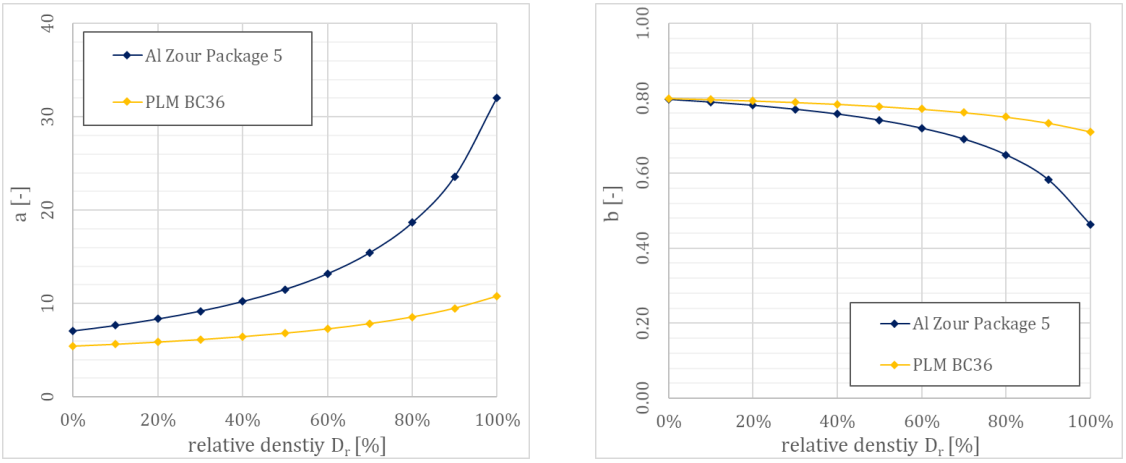

(A) (B)

FIGURE 5.6: The effect of an increasing relative density on the parameters a (A) and b (B) for the samples Al Zour Package 5 and PLM BC36

The Al Zour Package 5 graph in Figure 5.6 (A) represents the upper boundary curve whereas the PLM BC36 graph in Figure 5.6 (B) represents the lower boundary curve for all materials in the database. The graphs showing the increase of parameters a and b for all samples are plotted in Appendix C.2.

To evaluate the connection between parameters a and b and the soil's carbonate content, their respective values were plotted in Figure 5.7.

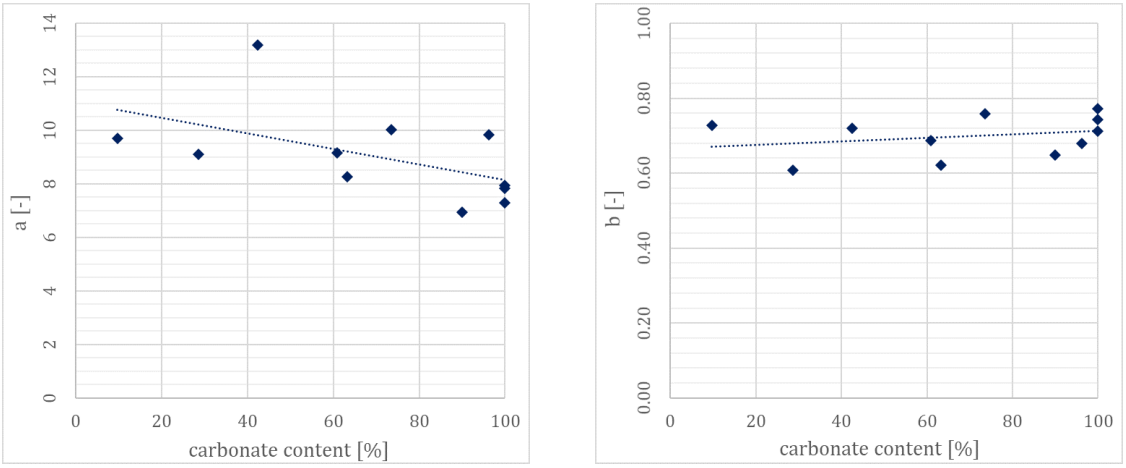

(A) (B)

FIGURE 5.7: Parameter a (A) and b (B) plotted against the carbonate content of the sand samples in the KELLER-database

Even though it seems that parameter a is a bit stronger correlated with the carbonate content than parameter b, it is still not a reliable connection. In the Al Zour LNG

sample, the carbonate content is 9.73% and the value of a amounts to 9.707. For the Palm Deira sample however, the carbonate content was tested to be 96.2 % and a results in only a slightly higher value of 9.833. As will be explained later on, this might be the result of the curve fitting in the calibration of the hypoplastic parameters for the Palm Deira sample which shows that the a_i and b_i parameters are very sensitive to certain assumptions. Indicated by the almost horizontal trend-line in Figure 5.7 (B), the correlation between the carbonate content and parameter b is even weaker. The results of the correlation analysis confirm these statements. For the carbonate content and parameter a, the coefficient of correlation is -0.5316 and for parameter b it is 0.2718.

5.3.1 Relation between soil properties and KIM-parameters

The a_i and b_i parameters for the calculation of the limit pressure p_{LS} are derived from curve-fitting the results of a series of spherical cavity expansion simulations. These simulations are performed with a hypoplastic constitutive model which is calibrated to the specific soil on site. As was explained in Chapter 4.2, these parameters depend on basic soil properties. It is therefore expected, that there is a connection between the characteristics of the soil and the a_i and b_i parameters.

While comparing the a_i- and b_i-parameters of the projects in the database to the respective soil and hypoplastic parameters, it was discovered that there are two a_i-b_i-data-sets which are quite similar to each other but quite different to all other data-sets. The KIM-parameters of the Sheikh Jaber CW and the JAT 4: South Side materials are quite similar even though the soil properties of both samples show significant differences. A comparison of the two materials can be seen in Table 5.8.

The d_{10} value for the Sheikh Jaber CW sample is missing because this material has a fines content of 15.51% which means 15.51% of the sand sample has a grain size smaller than 0.063 mm and didn't allow the d_{10} value to be measured by means of a sieve analysis. The graph of the particle size distribution is depicted in Appendix C.3. Under the assumption that the a_i and b_i parameters are influenced by the soil properties and judging from the properties listed in Table 5.8, a data-set with significantly differing values of a_i and b_i would be expected. The values listed in Table 5.9 prove that this expectation is wrong. A maximum difference of -17.03 % for the b_2-values is observed. It is also due to the similarities between the a_i and b_i parameters, that the curves of the two materials plotted in Appendix C.2 show a very similar shape. However, the resulting q_c-values for $D_r = 60\%$ at a depth of 10 m differ by about 30%.

Comparing the parameters of the M100 and the Palm Deira sample reveals exactly the opposite. In this example the carbonate content of 90% in the M100 and 96.2% in the Palm Deira material is almost identical and the initial soil properties vary only by maximum 4.86 % in the case of e_{min}. Table C.4 in Appendix C compares the the various parameters of the two samples and shows that only two of the hypoplastic parameters show noteworthy disparities. These two parameters are the exponents α and β differing by 76.92% and -36.36%, respectively. Exponents α and β are determined based on the results of a drained triaxial and a one-dimensional high-pressure compression test. The

TABLE 5.8: Comparison of the parameters of the Sheikh Jaber CW and the JAT 4: South Side samples

	Sheikh Jaber CW	JAT 4: SS	Δ[%]
$CaCO_3$	28.6	63.3	121.33
e_{min}	0.385	0.979	154.29
e_{max}	1.015	1.504	48.18
φ_c	31	39.5	27.42
ρ_s [g/cm^3]	2.650	2.777	4.78
d_{60} [mm]	0.362	0.910	151.38
d_{10} [mm]	-	0.147	-
e_{i0}	1.167	1.729	48.16
h_s [MPa]	40	28	-30.00
n	0.375	0.500	33.33
α	0.14	0.50	257.14
β	1.40	0.10	-92.86

calibration of α and β is done with a hypoplasticity element test program and is quite sensitive to certain assumptions. It is therefore assumed that the differences between the a_i and b_i parameters of the two materials are caused by inaccuracies during the calibration of α and β for the Palm Deira material. Table B.1 lists all hypoplastic parameters for the projects in the KELLER-database.

Another fact that supports the theory of high sensitivity in the parameter calibration should be mentioned here as well. When the soil mechanics lab was working on the samples PLM AZ28 and BC36, a preliminary progress report with the results of the PLM AZ28 sample was sent to KELLER. The results in this report led to significantly higher q_c-values than were expected considering the carbonate content of 100%. When the final report was submitted the laboratory stated that a triaxial test was repeated, the hypoplastic parameters were re-calibrated and the SCE simulations were also performed again. As a result of this procedure, only one hypoplastic parameter changed. Exponent α declined from 0.23 to 0.05 after the re-run of the tests. A small adjustment of α caused a substantial alteration of the a_i and b_i parameters of material PLM AZ28 and, subsequently, a reduction of the calculated cone resistance value of 38.14%. Comparisons of the incorrect and re-calibrated values can be found in Appendix C.5.

Since the soil behavior during the simulation of the SCE is governed by a hypoplastic model, the shape of the resulting curves must be influenced by the model's parameters. As the examples above show, finding a connection between the soil properties and the KIM parameters proved to be difficult. That could mean, that a_i and b_i can provide a general idea about the geometrical shape of the curve and about the magnitude of the cone resistance but a back-calculation to the hypoplastic or soil parameters might not be possible.

TABLE 5.9: Comparison of the parameters of the Sheikh Jaber CW and the JAT 4: South Side samples. The q_c-value is calculated for a depth of 10 m and $D_r = 60\%$.

	Sheikh Jaber CW	JAT 4: SS	Δ[%]
a_1	-25.082	-23.941	4.55
a_2	-215.493	-218.502	-1.40
a_3	-6.905	-7.384	-6.94
b_1	1.183	1.141	-3.55
b_2	0.716	0.594	-17.03
b_3	-1.845	-1.742	5.60
q_c [MPa]	15.46	10.84	-29.88

5.3.2 Sensitivity analysis

In order to evaluate the influence of the single a_i and b_i parameters on the q_c-result, a sensitivity analysis was conducted. First the median of each parameter was calculated and compared to the parameters of every project to find the sample most in the "middle" of the data-set. The data-set of the Zakkum Island project showed the smallest deviance from the median values. In fact, the four parameters a_1, a_2, a_3 and b_2 of this sample are identical to the median value.

For each iteration, only one of the six parameters was varied by +/-50% and +/-100% of the standard deviation and the remaining parameters were kept in their original form. This way, it was made sure that the variation of the result is a direct consequence of the variation of that one parameter. Every single parameter was varied and the corresponding cone resistances were calculated for a relative density of $D_r = 60\%$ and a depth of 5 m. The results were then compared to identify the parameter with the single most influence on the resulting q_c-value. Resulting q_c-curves from these computations are plotted in Appendix C.6.

Unfortunately, it was not possible to achieve the desired result and determine the influence of the a_i or b_i parameters on the magnitude of the cone resistance q_c. As can be seen in Figure C.3, the alteration of the values partly leads to impossible negative cone resistance values. Especially adding 50% of the corresponding standard deviation to the a_3-value caused the resulting cone resistance to reach an unrealistic value of 600 MPa at a depth of 5 m. A look at equation 5.9 helps to understand this result. In this case, the value of a_3 became -0.610 and therefore similar to the relative density which is entered as 0.6 into the equation. Thus, the denominator became -0.01 which caused the value of parameter a to result in 826.95. As was explained in Chapter 5.3, a high value of parameter a leads to a high value of p_{LS} which in turn leads to a high value of q_c.

Since the a_i and b_i parameters are derived by curve-fitting the same results of the SCE, it is assumed that there must be an inter-relation between these parameters. Varying

only one of the parameters during each iteration in the sensitivity analysis these interrelations are completely ignored and the modified parameter becomes disproportionate to the other parameters. It is assumed that this is the reason why the sensitivity analysis did not deliver realistic results.

5.4 Influence of the limit pressure p_{LS} on the cone resistance q_c

Together with the shape factor k_q, the limit pressure p_{LS} is used in Equation 5.1 to calculate the cone resistance q_c. The limit pressure depends on the KIM parameters a and b and the mean effective pressure p'_0 and therefore represents the state of the soil for which the cone resistance should be computed. The correlations between the input parameters and their influence on the limit pressure have been explained and shown in the previous chapters. This chapter will show briefly, how the value of the limit pressure affects the value of the calculated cone resistance. Figure 5.8 (A) shows the development of the limit pressure p_{LS} with an increasing carbonate content and 5.8 (B) depicts the connection between p_{LS} and the cone resistance.

The graph in Figure 5.8 (A) proves that there is a negative correlation between the carbonate content of the soil and the resulting limit pressure p_{LS}. This statement is supported by a correlation coefficient of R = -0.7604 indicating a strong relationship. For Figure 5.8 (B) the graph draws a perfect linear correlation between the limit pressure p_{LS} and the cone resistance q_c. This perfect linearity originates from the equation for q_c (Equation 5.1) in which p_{LS} is multiplied with the shape factor k_q to result in the cone resistance. Since the shape factor is constant as long as the relative density is not changed in the equation, this is the reason for the perfect correlation.

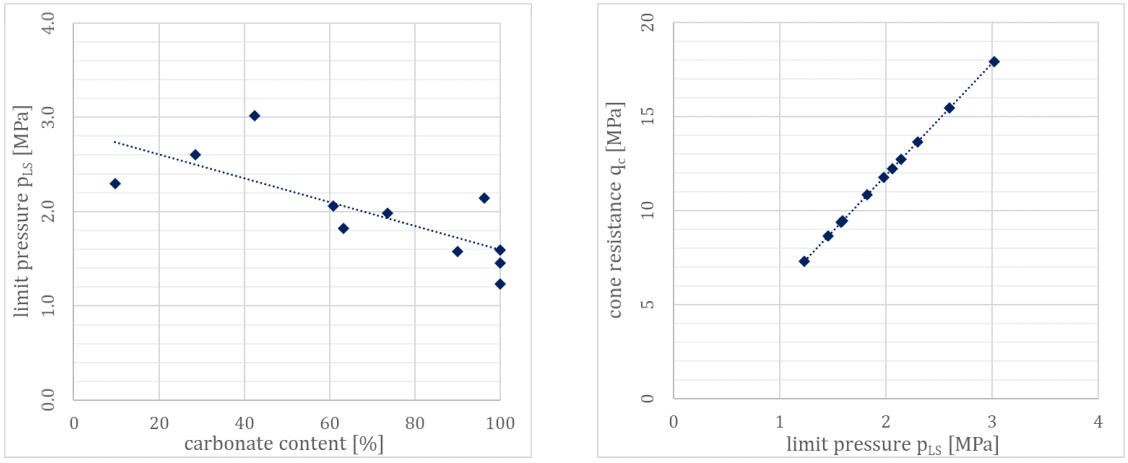

(A) (B)

FIGURE 5.8: The limit pressure plotted against the carbonate content (A) and the cone resistance plotted against the limit pressure (B)

Due to the connection between p_{LS} and k_q it is also expected that the cone resistance q_c will show the same connection to the carbonate content as the limit pressure.

5.4.1 Influence of the carbonate content on the cone resistance q_c calculated with the KIM

To finally show the influence of the soil's carbonate content on the results of the KIM, Figure 5.9 plots the q_c-values calculated for each project against the corresponding carbonate content. The graph clearly shows that there is a negative correlation between the value of the cone resistance calculated with the KIM and the content of $CaCO_3$ in the sand. The associated R-value of -0.7606 implies a medium to strong negative correlation between the two variables and therefore proves that the hypothesis after which the KIM-results decrease with an increasing carbonate content, is correct.

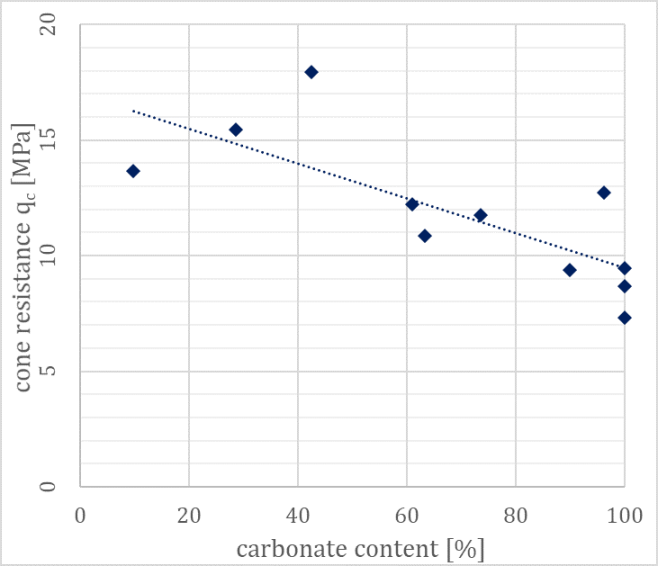

FIGURE 5.9: Relationship between the carbonate content and the cone resistance q_c at a depth of 10 m and relative density of 60%

The highest KIM-results are not calculated for the sand with the lowest carbonate content but result from the parameters of the Al Zour Package 5 material which consists of 42.45% $CaCO_3$. Based on the results calculated for the projects in the KELLER-database it seems that the KIM-q_c-value and the carbonate content actually show a positive correlation for the three samples with carbonate levels below 50%. As the graph in Figure 5.9 shows, the cone resistance values of the Al Zour Package 5, the Sheikh Jaber Causeway and the Al Zour LNG projects, the three samples with carbonate levels ranging from 9.73% to 42.45%, increase with an increasing carbonate content. This implies that for predicting the KIM-results in sands that show a carbonate content below a certain level, other factors than the percentage of $CaCO_3$ may also have to be considered to make a reliable estimation. A decrease of the KIM-results calculated for the samples in the database can only be observed for the materials with a carbonate content above approximately 50%. One attempt at explaining this circumstance is that the sand's mechanical behavior is mainly governed by the characteristics and mineralogy of the predominant sand grains. Sands which exhibit a carbonate content below 50% are therefore still governed by the characteristics of the dominant silica grain fraction. It is assumed that the carbonate sand fraction only starts to affect the mechanical

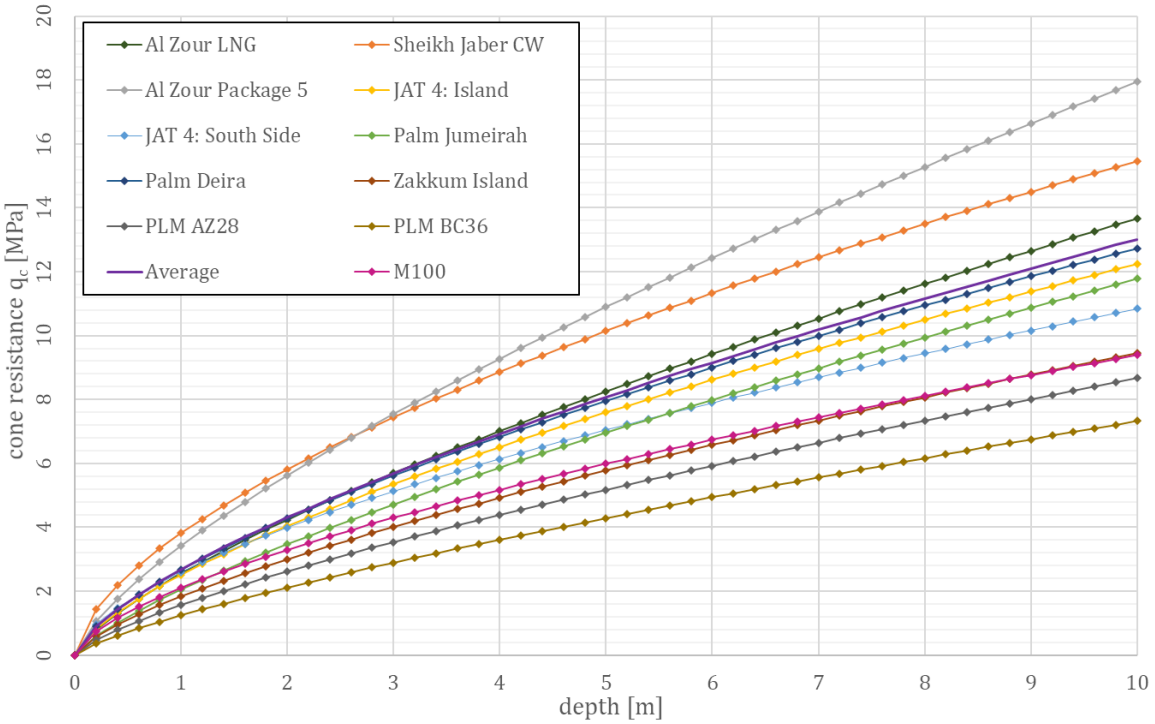

FIGURE 5.10: Cone resistance curves calculated with the KIM for all projects in the database and a relative density of 60%

behavior when it exceeds a certain threshold level with its influence increasing as the carbonate fraction gets larger. After this level is surpassed, the KIM-results generally decline with an increasing carbonate content. However, the three tested samples with a carbonate content below 50% do not provide enough data to identify the value of that threshold level.

KIM-curves computed for a relative density of 60% for all the investigated projects are plotted in Figure 5.10. The three materials Zakkum Island, PLM AZ28 and BC36 resulted in the lowest q_c-curves. These are also the three materials with the highest carbonate content of 100%. Sand samples from the Al Zour LNG, the Al Zour Package 5 and the Sheikh Jaber Causeway projects with a carbonate content below 50% produced the highest q_c-curves.

The Palm Deira material seems to contradict the established relationships from the previous chapters. According to this sand's carbonate content of 96.2% one might expect a cone resistance curve in the same region as materials with a similarly high content of $CaCO_3$. But as Figure 5.10 shows, the q_c-curve of this sand is almost equal to the average curve. As was explained in Chapter 5.3.2, this is most probably attributed to calibration procedure of the hypoplastic model parameters. These parameters have a strong influence on the a_i and b_i parameters which, together with the mean effective pressure p'_0, ultimately govern the result of the cone resistance calculated with the KIM.

5.5 Conclusion

The intentions of this chapter are to explain the necessary calculation steps, identify the inter-relations of the parameters and identify the connection between the results of the KIM and the carbonate content of the respective soil sample. After presenting the necessary calculation steps and the corresponding equations, it was shown how the initial soil parameters influence the result of the calculation of the mean effective pressure p'_0 and how their effect propagates to the final result of q_c. Up to this step of the calculation sequence, the effect of each input parameter can be explained with the respective equations and the resulting value of p'_0 can be predicted quite accurately.

Besides the mean effective pressure p'_0, the calculation of the limit pressure also requires the a_i- and b_i-parameters. However, the introduction of these parameters makes a further forecast of the result more difficult. Chapter 5.3 explained the impact of the parameters a and b on the calculation of the limit pressure p_{LS} and described the difficulties of relating them to the initial soil properties. The calculation of the limit pressure p_{LS} at a depth of 10 m and a relative density of 60% for every project in the database revealed that, due to the impact of parameters a and b, the maximum and minimum values of p_{LS} are not calculated for the samples with the maximum and minimum mean effective pressure p'_0. Performing a simple sensitivity analysis did not bring any clarity into the connection between the a and b parameters and the soil properties. On the basis of four data-sets it was shown that a back-calculation from the a_i and b_i parameters to the initial soil properties might not be possible without performing a proper sensitivity analysis involving a re-calibration of the hypoplastic parameters and the KIM-parameters.

In the introduction it was asserted that the carbonate content can serve as an indicator for the magnitude of the resulting cone resistance q_c. By relating the decisive parameters of each project to the respective carbonate content, it was demonstrated that an increasing carbonate content correlates with a decrease of the mean effective pressure p'_0, the limit pressure p_{LS} and, ultimately, the cone resistance q_c. To sum up the result of the calculations, Table 6.7 gives an overview of the main components of the KIM-equation calculated for every project in the database. The projects are listed in order of their carbonate content which makes it more obvious how some parameters behave with the rise of the percentage of $CaCO_3$.

TABLE 5.10: Results of the main components of the KIM-equation calculated for a depth of 10 m and a relative density of $D_r = 60$ %

Material	$CaCO_3$ [%]	p'_0 [MPa]	a [-]	b [-]	p_{LS} [MPa]	$q_{c,KIM}$ [MPa]
Al Zour LNG	9.73	**0.138**	9.707	0.728	2.299	13.66
Sheikh Jaber CW	28.6	0.128	9.096	*0.608*	2.602	15.46
Al Zour Package 5	42.45	0.129	**13.195**	0.720	**3.020**	**17.94**
JAT4: Island	60.9	0.114	9.167	0.688	2.060	12.24
JAT4: South Side	63.3	*0.088*	8.266	0.621	1.825	10.84
Palm Jumeirah	73.6	0.118	10.027	0.759	1.981	11.77
M100 Dubai sand	90	0.102	*6.936*	0.649	1.580	9.39
Palm Deira	96.2	0.106	9.833	0.679	2.143	12.73
PLM - AZ28	100	0.104	7.837	0.743	1.458	8.66
PLM - BC36	100	0.100	7.298	**0.771**	*1.233*	*7.33*
Zakkum Island	100	0.105	7.953	0.713	1.593	9.46

For a better understanding of the relationships between the various parameters and their connection to the carbonate content of the soil, the diagram in Figure 5.11 was developed.

The diagram serves as a visual aid to explain the effects of an increasing carbonate content on the various input parameters and illustrates the propagation of each parameter to the resulting cone resistance q_c. The arrows next to each of the parameters indicate the way they are changed by the preceding parameter.

Reading the diagram from top to bottom would result in the following sequence: a sand with a high carbonate content will very likely show high values of the limit void ratios e_{min} and e_{max}. These will in turn cause the value of the in-situ void ratio e_{Dr} for a certain relative density to be high as well. Even though an increasing carbonate content will also cause the grain density ρ_s to rise, the influence of a high in-situ void ratio will outweigh the grain density's effect and lower the result of the dry density calculation. Analog to the limit void ratios and grain density, the critical friction angle tends to be higher in sands with a high carbonate content which in turn causes a lower coefficient

of lateral earth pressure K_0. The computed value of ρ_d will be used to calculate the effective vertical pressure σ'_v which will then, together with K_0 be incorporated in the equation for the mean effective pressure p'_0. With the a_i and b_i parameters obtained from the simulation of the spherical cavity expansion, the limit pressure p_{LS} will be calculated. Conclusively, p_{LS} will be multiplied with the shape factor k_q for the target relative density and result in the cone resistance q_c.

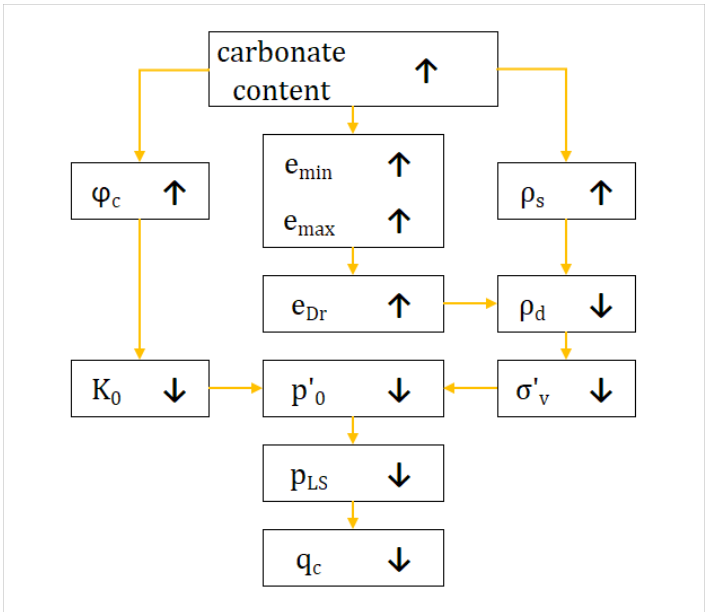

FIGURE 5.11: Influence of the carbonate content on various soil properties and calculated parameters

6 Case study: Application of the KIM at a land reclamation project in Dubai

KELLER was appointed to carry out the ground improvement works of the reclaimed land at Jumeirah Open Beach, Dubai. The dredged sand used as hydraulic fill for this project showed high amounts of sea-shells and coral lumps and was therefore expected to exhibit a carbonate content high enough to lead to the known issues with the quality control of the compaction works by means of CPT. For this reason, this project was chosen to serve as a case study for the practical application of the KIM. This chapter will describe the procedure from taking the samples to the evaluation of the results.

6.1 Introduction

The project at hand is an extension to an existing reclaimed peninsula in Jumeirah Open Beach in Dubai. As can be seen in Figure 6.1 (A), the proposed extension involves increasing the area of the northern peninsula by approximately 170000 m^2 through an extensive land reclamation operation which will require approximately 4 million m^3 of additional dredge material [46].

KELLER was appointed as a geotechnical contractor to carry out the necessary ground improvement works and prepare the reclaimed land for the subsequent construction of infrastructure and residential development. For a project like this in which the land is reclaimed by hydraulic filling, deep vibratory compaction is a suitable method to densify the soil throughout the full thickness of the reclamation fill. After the first reclamation works were completed, it was found that the dredged sand contains a significant amounts of sea-shells and coral lumps and must therefore show an elevated level of $CaCO_3$. Since CPTs performed in calcareous sands tend to measure lower cone resistance values than in silica sands [4], concerns were raised about the required q_c-values and it was decided to apply a site-specific procedure to correlate the relative density D_r and the cone resistance q_c. Therefore, the Karlsruhe Interpretation Method was used.

The Karlsruhe Interpretation Method is capable of calculating the value of a cone resistance corresponding to any desired relative density. Solving the inverse problem is possible as well and allows to calculate the relative density that corresponds to measured q_c-values. To examine the accuracy of the solution of such an inverse calculation, a series of in-situ density tests were performed with cutter-cylinders of different dimensions to determine the in-situ relative density. These values were then compared

to D_r-values resulting from measured post-CPT cone resistances. These tests and the results will be discussed here as well.

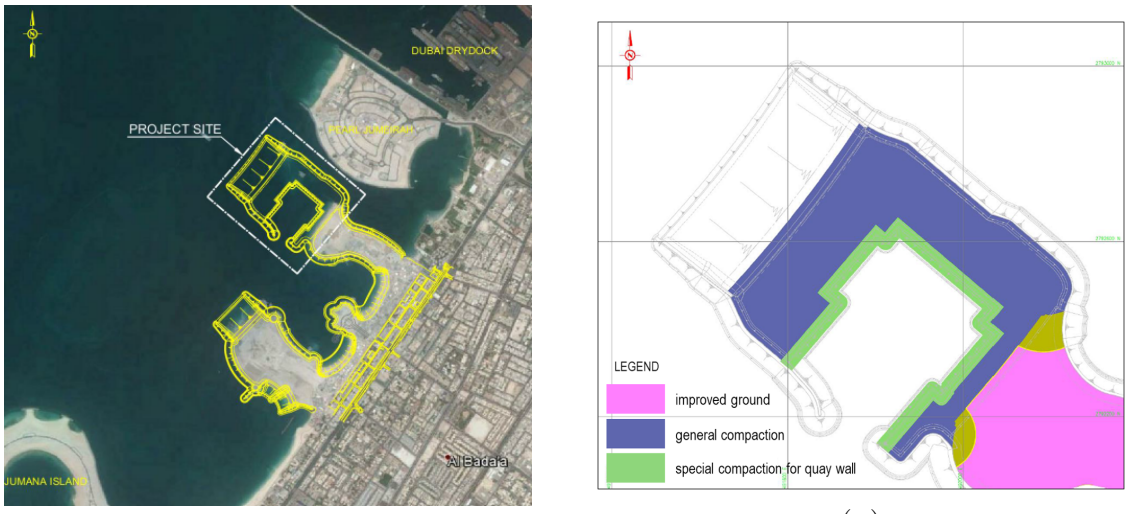

(A) (B)

FIGURE 6.1: Location of the project (A) and the extent of the compaction works (blue and green) (B) [46]

6.1.1 Compaction criteria

Quality control of the compaction for the verification of the ground improvement was done by cone penetration tests performed no less than seven days after the completion of the compaction works in the area [46]. To guarantee that the soil mass achieves certain minimal criteria related to stiffness, liquefaction criteria and shear strength, the cone resistances measured in the post-CPTs have to be higher than a performance line corresponding to a certain relative density.

One set of two cone penetration tests is carried out within every box of 25 m $\times$ 25 m (625 m^2) in specific locations in the triangular compaction grid. One cone penetration test is situated at 1/3 of the distance between two compaction points and one in the center of the triangle. The results of these CPTs are averaged and a rolling mean (see Chapter 3.1.3) over 40 cm (20 cm above and 20 cm below) is determined to smoothen the curve. This rolling mean q_c-profile will then be used for the evaluation of the compaction criteria.

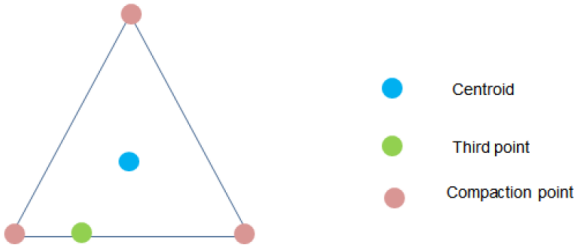

FIGURE 6.2: CPT-points in the triangular compaction grid [46]

For the project described in this chapter, the criteria to be achieved after the compaction are as follows:

- All post-compaction CPTs achieve higher cone resistance values than the performance line associated with the minimum target relative density of 60%.
- Below the water table, the averaged post-CPT q_c-values at each test location is allowed to be below the average target relative density of 65% at a maximum of 10% of the treatment depth.
- Above the water table, the averaged post-CPT q_c-values at each test location may not fall below the average target relative density of 65% at all.

To obtain a detailed cone resistance curve over the whole depth of the fill, the performed CPTs log the q_c-value in 2 cm increments. According to the compaction requirements mentioned above, the client can refuse to accept the compaction work and ask for remedial action if a single one of the measured 2-cm-cone-resistance values falls short of the requirement with the argument being that by not reaching the required cone resistance, sufficient stiffness and therewith sufficient resistance against liquefaction and excess settlements can not be guaranteed. It is questionable if the evaluation in such small increments is reasonable because the overall stiffness will not be affected much by a few thin less compacted layers.

6.1.2 Cone resistance requirements provided by the client

The cone resistance requirement proposed by the client is determined by calculating a weighted average of the cone resistance vales computed with three different methods.

There are a few issues with the proposed cone resistance requirement. Method A was identified as the interpretation method proposed by Baldi et al. [15]. However, there were no references given in the documents provided by the client and even after extensive research in the relevant literature, it was not possible to identify the other two equations. It was also not possible to clarify why Method A and B have double the weight of Method C in the calculation of the weighted average.

The three methods are as follows:

- Method A:

$$q_c = 157 \cdot (\sigma'_v)^{0.55} \cdot e^{(2.41 \cdot D_r)} \tag{6.1}$$

- Method B:

$$q_c = \frac{1}{3.193} \cdot \sqrt{\sigma'_v} \cdot 10^{\left(\frac{D_r - 41}{64.778}\right)} \tag{6.2}$$

- Method C:

$$q_c = 2.776 \cdot \sqrt{\sigma'_v} \cdot \left(\frac{D_r}{100}\right)^2 \tag{6.3}$$

For every increment of depth, a value of q_c was calculated with each of the three equations listed above. Then, a weighted average of the three values was calculated with the following equation:

$$q_{c,avg} = \frac{2 \cdot q_{c,A} + 2 \cdot q_{c,B} + q_{c,C}}{5} \tag{6.4}$$

For the calculation of the q_c-values corresponding to the two targeted relative densities of $D_r = 60\%$ and $D_r = 65\%$, the vertical effective stress σ'_v in the equations listed above is calculated with a predefined unit weight $\gamma = 18.5$ kN/m^3. However, as was shown in Chapter 5.2.1, the unit weight γ depends on the targeted relative density D_r and increases when D_r increases. In the equations proposed by the client, the change of γ with the change of D_r is ignored. Another issue is that the unit weight of the PLM samples is lower than the prescribed unit weight of $\gamma = 18.5$ kN/m^3. A higher unit weight γ leads to a higher vertical effective stress σ'_v which in consequence will lead to a higher required q_c-value. That means that the q_c-target values calculated with the defined unit weight will correspond to a relative density higher than the demanded one. Back-calculating the relative density corresponding to a unit weight of $\gamma = 18.5$ kN/m^3 according to the calculation steps in Chapter 5.2.1 resulted in the values listed in Table 6.1. As can be seen, for the samples from the boxes AZ28 and BC36, the prescribed unit weight corresponds to a relative density much higher than the required relative density.

TABLE 6.1: Results of the back-calculation from a given unit weight $\gamma = 18.5$ kN/m^3

box	$CaCO_3$ [%]	γ [kN/m^3]	ρ_d [g/cm^3]	e_{Dr} [-]	D_r [%]
AZ28	100	18.5	1.542	0.810	86.5
BC36	100	18.5	1.542	0.810	96.6

6.2 Sand samples for the KIM

According to Cudmani [5], the parameters necessary for the calibration of the hypoplastic material model can be determined on disturbed soil samples. This simplifies the sampling process a lot since taking undisturbed samples in cohesionless material like sand is very difficult and can only be done by freezing techniques.

Two sand samples at two different locations were taken and sent to a soil mechanics laboratory. Under the assumption that the dredged sand is more or less homogeneous throughout the whole reclaimed area, it was expected that the hypoplastic and KIM-parameters resulting from the lab tests should not differ too much. To make sure the soil mechanics lab has enough material, an amount of approximately 20 kg per sample were taken from the site.

In previous projects, only one sand sample was taken from the site and sent to the geotechnical laboratory. As a "blind" test for the laboratory to see how much the material and KIM parameters differ across the site, two sand samples were retrieved from the site investigated in this chapter.

6.2.1 Sampling locations

Figure 6.3 illustrates the location of the two boxes from which the samples were taken. The samples were retrieved on the 29th of March 2017. By that time, the reclamation works were still at an early stage and much of the western part of the project site has not yet been reclaimed or was still not accessible. The boxes AZ28 and BC36 were chosen because, in addition to the mandatory pre-compaction CPTs, pre-compaction boreholes were also carried out in these boxes. This provides a lot of information about the subsurface conditions and allows the results of the KIM to be referenced to the results of the pre-CPTs and the boreholes.

Table 6.2 some information about the pre-compaction-CPTs and pre-compaction-boreholes. Note that the elevation is given in the Dubai Municipality Datum (DMD).

Table 6.2: information of the pre-CPTs and boreholes in box AZ28 and BC36

box		*elevation*	*depth*
AZ28	pre-CPT	4.07 m DMD	14.78 m
	borehole	4.11 m DMD	14.80 m
BC36	pre-CPT	5.50 m DMD	17.48 m
	borehole	5.57 m DMD	17.60 m

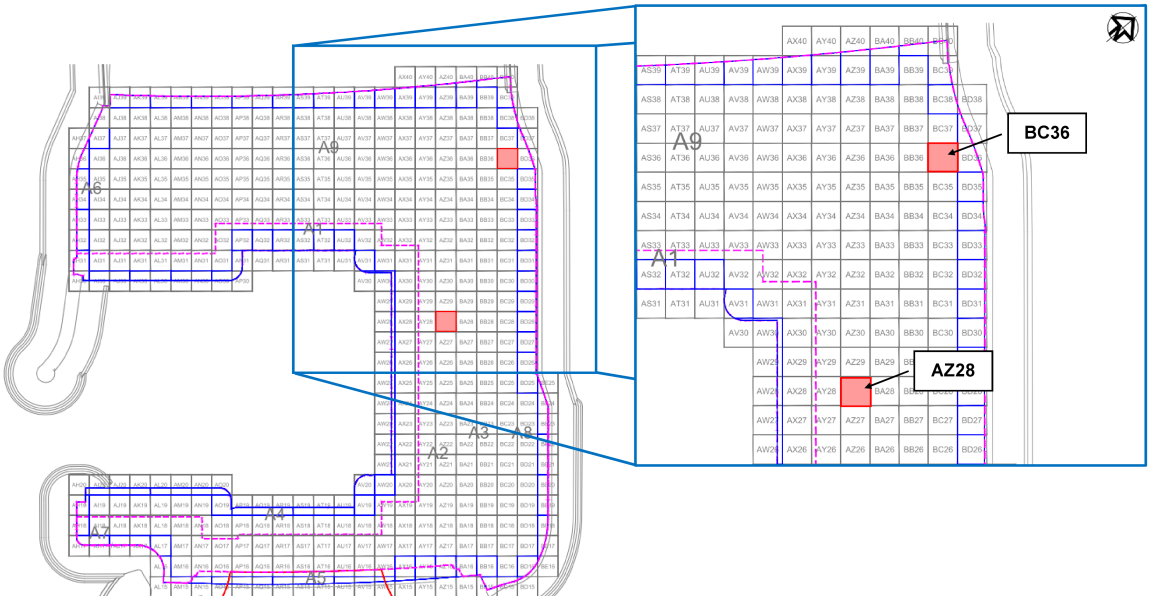

FIGURE 6.3: Location of the boxes from which the samples were taken

6.2.2 Taking the samples

As can be seen in Figure 6.4 (A) and (B), corals and sea-shells and fragments of them tend to accumulate on the ground's surface because the lighter sand particles are carried away by the constant wind leaving only the heavier sea-shells and coral fragments behind. Soil samples taken from the surface might have shown an increased content of shells and corals and would therefore not have been representative of the fill material. To obtain suitable samples, a wheel-loader excavated a ditch (Figure 6.5 (A)) with a depth of approximately 1 m in the vicinity of the borehole and pre-CPT. After the ditch was excavated, laborers stepped in and shoveled sand from the bottom into the sample bags until roughly one fourth of the bag was full (Figure 6.5 (C), (D)).

Due to the weight of approximately 25 kg of each sample and the partially sharp-edged sand grains, durable sampling bags were required. Flour bags which are perfectly suited for this task. Alternatively, a sturdy bucket with a lid can be used as a sampling container. After two bags with roughly 25 kg of sand from the bottom of the ditch were filled, the bags were labeled with the box code and the date to avoid confusion with the samples from the other box. This procedure was repeated in box BC36. For photos of the sampling process in box BC36 please refer to Appendix D. From each location, a sample of 25 kg was packaged and sent to a soil mechanics lab where the lab-tests and numerical simulations were performed. The remaining 25 kg from each box were stored to have a back-up material for investigations that might be necessary later.

(A) (B)

FIGURE 6.4: Accumulation of large sea-shells and coral lumps on the surface in box BC36

6.3 Results

After receiving the sand samples from the investigated project, the soil mechanics laboratory carried out a series of tests and numerical simulations in order to determine the relevant material and model parameters for the KIM. The following subsections will explain the necessary tests and discuss the results.

Before any of the tests were performed, the two samples were sieved and any sand grains larger than d $>$ 8 mm were removed by the laboratory. This had to be done because of size limitations of the test apparatuses. According to the laboratory, the desired ratio of sample height h to the maximum grain size d_{max} for a one-dimensional compression test should be $h/d_{max} > 5$.

Figure 6.6 shows the removed material which mainly consists of fragmented sea-shells and corals. In total, 2.7% of the mass of the sample from box AZ28 and 6.7% of the mass of the BC36 sample had to be removed. Meier [16] investigated the influence of coarse grains with $d > 4$ mm on the cone resistance q_c in a series of calibration chamber tests at the University of Karlsruhe. For these tests, Karlsruhe silica sand was mixed with a coarse material (d $>$ 4 mm) mainly consisting of sea-shells and coral lumps from a sand sample from Dubai. Two sand samples with a coarse fraction of 5% and 20% were prepared. After performing two CPTs in the calibration chamber on each mixture, the results were compared to the results of the CCT on the sand without a coarse fraction. Meier found that a coarse content of up to 5% has no influence on the resulting cone resistance q_c. For the material with a coarse fraction of 20% the resulting cone resistance values were approximately 25% higher than the results from the 5% material [16]. Meier also notes that these findings cannot be transferred to coarse material that only consists of large shells and shell fragments without any coral lumps.

Based on these results it can be concluded that the influence of removing 2.7% and 6.7% of coarse material is negligible [34].

(A) (B)

(C) (D)

FIGURE 6.5: Excavation of the ditch (A) and taking of the samples (B) in box AZ28 and the bagged and labeled samples from box AZ28 ((C) and (D))

6.3.1 Basic soil parameters

As a first step the laboratory performed several standard index tests to find the basic soil properties of the samples. A complete list of the performed tests can be found in Table D.1 along with the resulting parameters and the related testing standard. All retrieved parameters are either necessary for the calculation of the mean effective pressure p'_0 or are the base for the subsequent calibration of the hypoplastic model and the simulation of the spherical cavity expansion.

Table 6.3 sums up the results of the laboratory tests. Even though the carbonate content is not a direct input parameter for the calculations of the KIM, it is an important parameter because it allows the estimation of several soil parameters like the limit void ratios and the friction angle. As explained in Chapter **??**, a high carbonate content correlates with a low q_c-value resulting from the KIM. The carbonate content of the samples from the boxes AZ28 and BC36 was determined according to DIN 18129. As the amount of sea-shells and coral lumps observed while taking the samples already suggested, the carbonate content of both samples was determined to be 100% $CaCO_3$.

The differences between the parameters of both sand samples are small and the sand can be considered to be more or less identical. Both sand samples also show values which are typical for calcareous sands. The limit void ratios e_{min} and e_{max}, the grain

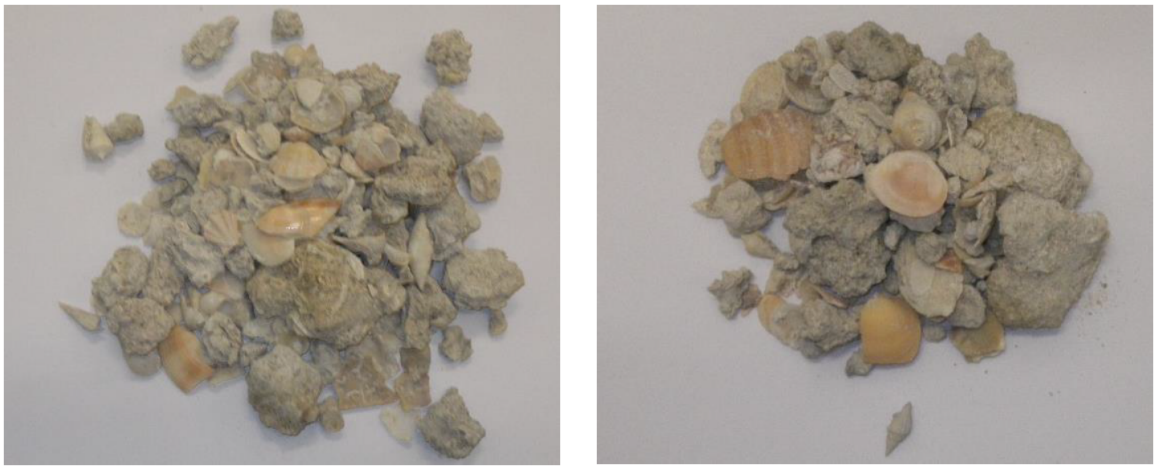

(A) (B)

FIGURE 6.6: Sand grains larger than d > 8 mm removed from the AZ28 (A) and BC36 (B) sample [34]

density ρ_s and the friction angle φ_c show values which would be expected in sand with a carbonate content of 100%. The parameters of Ticino sand are also listed in Table 6.3 to show how the values of a typical silica sand compare to the parameters of the calcareous sand samples from the project described in this chapter. The lower values of the friction angle φ_c and the limit void ratios are attributed to the different shape and origin of the sand grains. The sand grains of Ticino sand are in general more rounded and, due to the different mineralogy, less prone to grain crushing. Both of these characteristics cause the friction angle, the void ratios and the grain density to be lower than in the calcareous samples. Note that the Δ-values were calculated to show the differences between the AZ28 and BC36 sample only and do not consider the values of Ticino sand.

The maximum dry density (MDD) also known as Proctor density ρ_{Pr} was determined by the standard Proctor test. In this test, the sample is compacted in three equal layers, each layer receiving 25 blows of a 2.5 kg weight falling from a height of 300 mm. Mengé et al. [47] state that, in calcareous sands, this technique causes crushing of the sand particles which causes the maximum dry density to increase and lead to higher densities than can be reached in the field. In the same paper, it is recommended to use the vibratory table test according to ASTM D4253 to determine the MDD of calcareous sands since the grain crushing is expected to be lower in this test than in the Proctor test.

TABLE 6.3: Basic soil properties of the samples from box AZ28 and BC36 [34]

box	$CaCO_3$	e_{min}	e_{max}	φ_c	ρ_s	ρ_{Pr}	w_{opt}
	[%]	[-]		[°]	[g/cm³]		[%]
Ticino [5]	-	0.59	0.94	31	2.67	-	-
AZ28	100	0.74	1.261	36.3	2.791	1.55	18.2
BC36	100	0.79	1.384	36.5	2.791	1.50	20.8
Δ [%]	0.00	6.76	9.75	0.55	-0.69	-3.23	14.29

6.3.2 Grain size distribution

The grain size distribution was determined with a sieve analysis according to DIN 18123 - 5. The resulting graphs are plotted in Figure 6.7 for both materials and show that the samples are practically identical. The d_i values and the coefficient of uniformity C_u listed in Table 6.4 also confirm the similarity of the two samples.

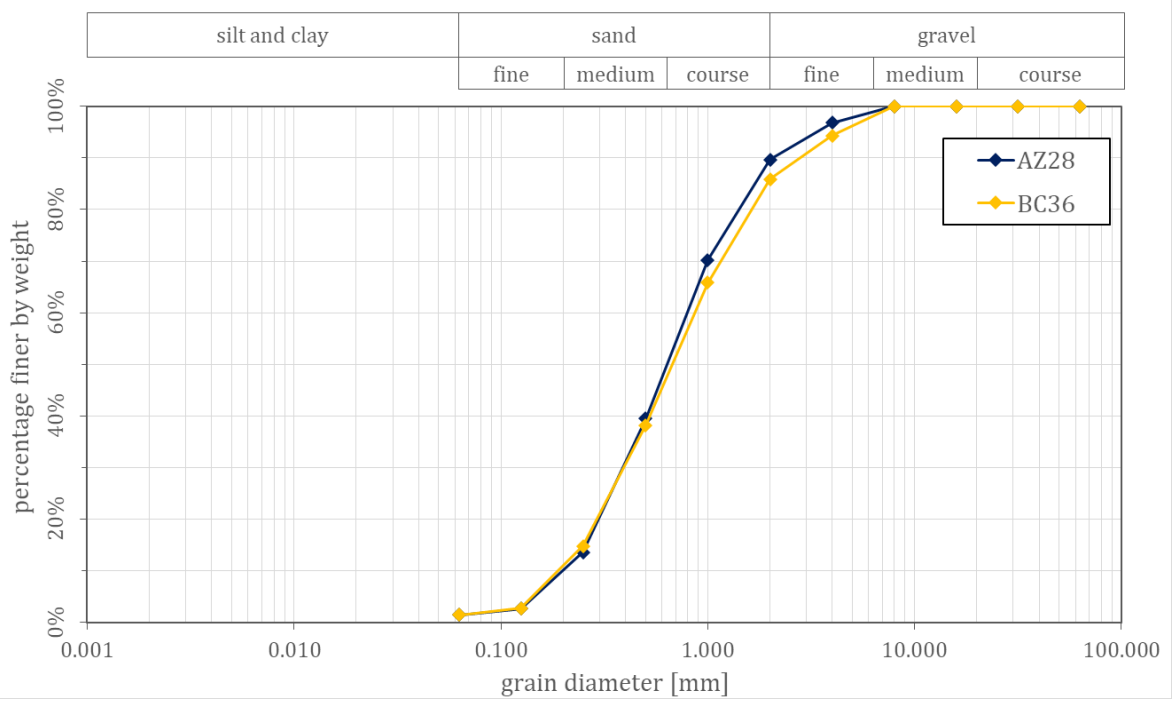

FIGURE 6.7: Grain size distribution of both samples [34]

TABLE 6.4: d_i-values and coefficient of uniformity C_u of the samples from box AZ28 and BC36 [34]

box	$CaCO_3$ [%]	d_{60}	d_{30} [mm]	d_{10}	C_u [-]
AZ28	100	0.8	0.395	0.2	4.0
BC36	100	0.896	0.395	0.194	4.61
Δ [%]	0.00	12.00	0.00	-3.00	15.25

6.3.3 Hypoplastic parameters

As a next step, the hypoplastic material model was calibrated to the sand samples from box AZ28 and BC36. For that purpose, the necessary material parameters listed in Table 6.5 were determined according to the procedure described in Chapter 4.2. As can be seen, the differences between the two data-sets are increasing compared to the differences between the index parameters listed in Table 6.3. With a difference of 25.6% and -28.9% the values of h_s and β of both materials show the biggest variation. It is assumed that this is connected to the interrelation of the parameters h_s, n, α and β which are found through an iterative process by simulating one-dimensional compression tests and consolidated triaxial tests with by means of an element test program.

TABLE 6.5: Hypoplastic parameters of the samples from box AZ28 and BC36 [34]

box	$CaCO_3$ [%]	φ_c [°]	e_{d0}	e_{c0} [-]	e_{i0}	h_s [MPa]	n	α [-]	β
Ticino [5]	-	31	0.590	0.940	1.110	250	0.680	0.11	1.00
AZ28	100	36.3	0.740	1.261	1.450	39	0.525	0.050	1.97
BC36	100	36.5	0.790	1.384	1.592	49	0.480	0.045	1.40
Δ [%]	0.00	0.55	6.76	9.75	9.79	25.64	-8.57	-10.00	-28.93

The values for Ticino sand were determined by Cudmani [5] and are listed in Table 6.5 to show how the hypoplastic parameters differ from the calcareous ones. While all parameters show quite a difference, the values of the granulate hardness h_s show the largest variation. The larger h_s-value of the Ticino sand results from the stiffer reaction of a silica grain skeleton during the one-dimensional compression test. Exponent α, which controls the dilatancy behavior of the sample, is higher for the Ticino sand sample because silica sands are less prone to grain crushing and therefore show a more distinct dilatant behavior than calcareous sands. The results of the triaxial tests on the AZ28 and BC36 samples discussed in the next paragraph confirm this statement.

For the calibration of the hypoplastic material model, four consolidated-drained triaxial tests were performed for each sample. Two triaxial tests with an isotropic effective mean

pressure of $p'_0 = 100$ kPa on two specimens, one with a loose and one with a dense initial packing, as well as two triaxial tests with an isotropic effective mean pressure of $p'_0 = 600$ kPa on a loose and a dense specimen. The results of these triaxial tests were unexpected in the sense that both materials showed significant contractive behavior even for the specimens with a dense initial packing. To verify the results, another triaxial test with an isotropic effective mean pressure of $p'_0 = 300$ kPa was carried out on a dense specimen of the BC36 material. Figure 6.8 shows the change of volume during triaxial compression of three dense specimens prepared from the BC36-material and three different isotropic effective mean pressures.

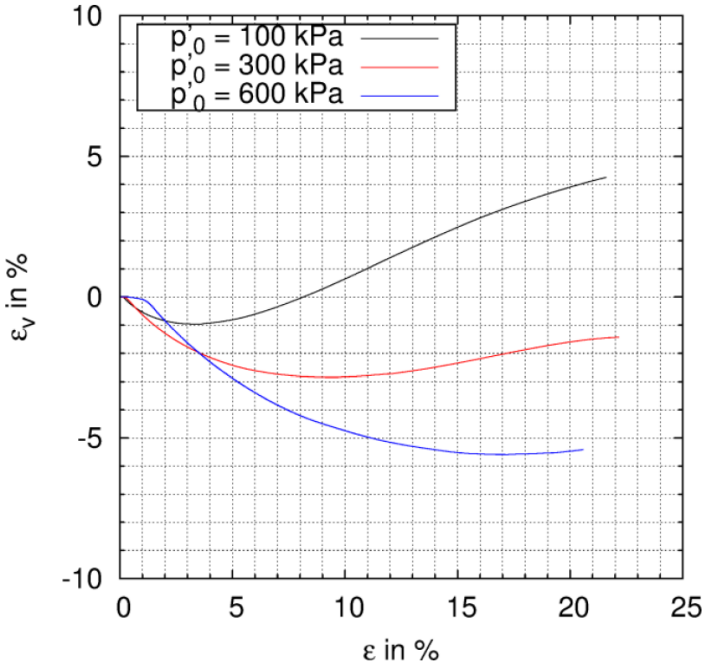

FIGURE 6.8: Volumetric strain plotted against axial strain during triaxial compression of the sample from box BC36 [34]

Usually, sand samples would first show a slight decrease of the volume (contraction) and then an increase of the volume (dilation). This well-known shearing behavior was only observed in the specimen which was subjected to the lowest isotropic effective mean pressure of $p'_0 = 100$ kPa. The other two triaxial tests at the higher pressure levels of $p'_0 = 300$ kPa and $p'_0 = 600$ kPa resulted in a contractive behavior. The samples were mounted into the triaxial test apparatus with a relative density of $\approx 80\%$. According to the soil meachanics laboratory, any further densification of sands with hard and stable grains could only be done by cyclic shearing with very small strain amplitudes [34]. Therefore, the laboratory attributed the contractive behavior to the fracturing of carbonate sand grains causing the volume of the sample to further decrease. In the case of the test performed with an isotropic effective mean pressure of $p'_0 = 100$ kPa, the pressure level wasn't high enough to cause crushing of the grains which allowed the specimen to dilate until the end of shearing. It is assumed that the origin and the shape of the grains also plays a role in this behavior but that was not investigated any further.

The granulate hardness h_s and exponent n are found by curve fitting the results of a one-dimensional high-pressure oedometer test and subsequently simulating the same test with a hypoplasticity element test program (ETP). h_s and n are adjusted until the results of the simulation match the results of the real tests. Figure 6.9 plots the curve resulting from the actual test (lab) and the curve resulting from the simulation (calc) and shows that the parameters h_s and n reproduce the real behavior of the soil quite well. The two oedometer tests were performed on a dense specimen with an initial void ratio of $e_0 = 0.749$ ($D_r = 98.3\%$) and a loose specimen with $e_0 = 1.200$ ($D_r = 11.70\%$). For the BC36 sample the two parameters were determined to be $h_s = 49$ MPa and $n = 0.480$. Results of the oedometer tests performed on the AZ28 sample are shown in Appendix D.2.1.

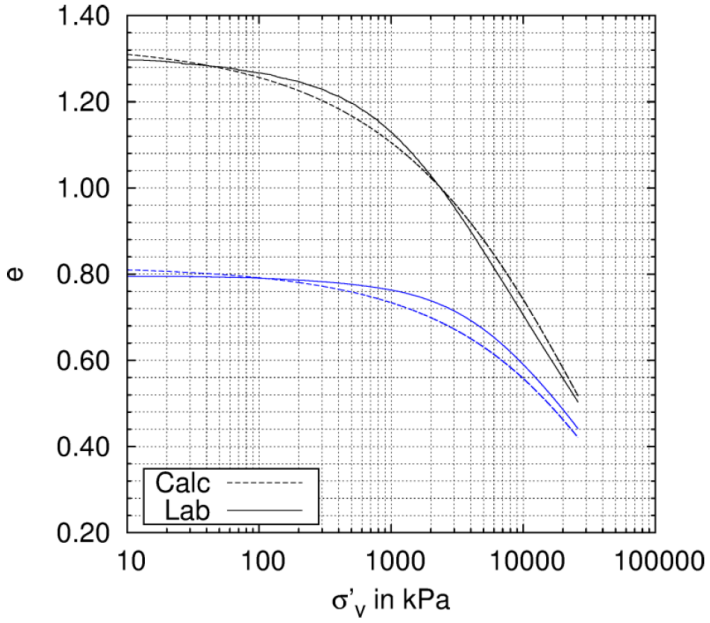

FIGURE 6.9: Results of the one-dimensional high-pressure compression test (lab) and the calibration (calc) for the sample from box BC36 [34]

The oedometer tests were performed with a vertical effective pressure up to $\sigma'_v = 25$ MPa. The high-pressures in the oedometer test are necessary to guarantee good accuracy of the KIM because the hypoplastic constitutive equation has to be calibrated for a pressure range that is similar to the pressures occurring in the actual CPTs [16]. Another reason is that the "von Wolffersdorff"-model [25] of hypoplasticity describes the change of stress in an idealized simple grain skeleton which does not allow for fracturing of the sand grains. By performing high-pressure oedometric tests, the effects of crushing sand grains are indirectly recorded and incorporated in the parameters h_s, n and β.

The exponents α and β are determined with a similar approach. By using the ETP to simulate a triaxial test, α is calibrated by adjusting its value until the simulation matches the results of the consolidated-drained (CD) triaxial test on a specimen with a dense initial packing. Exponent β is calibrated by simulating a one-dimensional high-pressure oedometer test on an initially dense specimen with the hypoplasticity ETP

and the subsequent comparison with the results of the actual tests. For the sample from box BC36, exponent α has a value of $\alpha = 0.045$ and β was calibrated to $\beta = 1.40$.

The calibration steps for h_s, n, α and β are interrelated, several iterative steps might be necessary to find the final set of parameters. The granulate hardness h_s and exponent n influence the progression of the curves of the triaxial compression test which means that, even though h_s and n might be calibrated well to the oedometer test, they might not describe the curves resulting from the ETP-simulation of the triaxial test so well (Figure 6.10). In an ideal case it is possible to find a set of parameters that adequately describes both, the oedometer and the triaxial test. In other cases, like the one presented here, a compromise has to be found depending on the desired application. Meier [16] states that the correct reproduction the compressibility of a dense specimen at very high pressures as in the case of the interpretation of CPTs in sands might be more important than the precise reproduction of the shearing behavior.

Looking at the graphs plotted in Figure 6.10 it can be seen that the results from the ETP-simulation do not nearly match the results from the triax tests as good as they matched for the oedometer test. As mentioned before, in this case it was more important to reproduce the compressibility and therefore, the overall results of the calibration of the hypoplastic parameters is deemed satisfactory by the geotechnical laboratory [34].

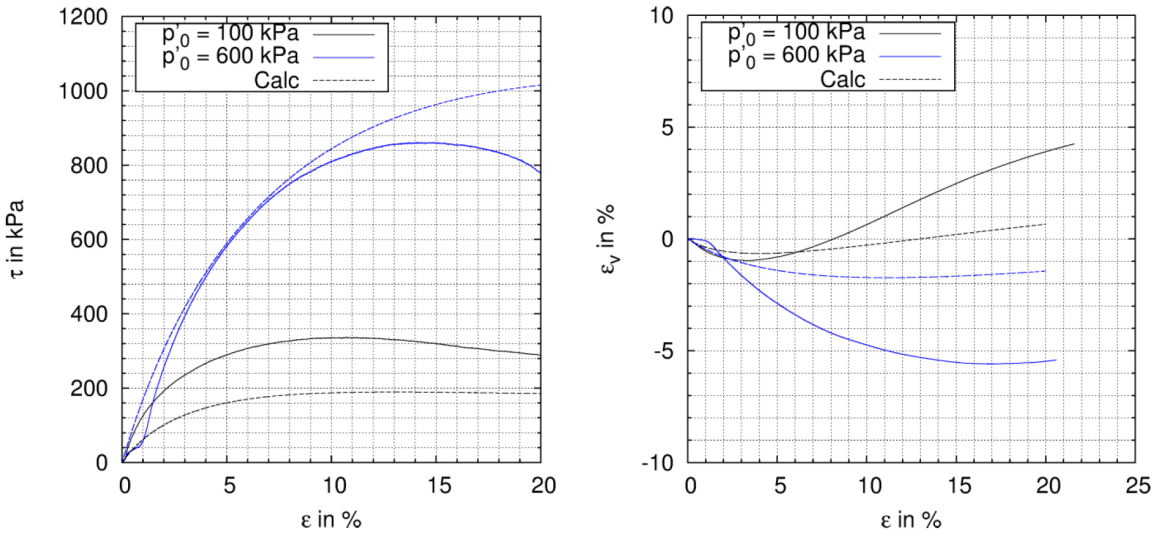

FIGURE 6.10: Results of the consolidated-drained triaxial test on a dense specimen (lab) and the calibration (calc) for the sample from box BC36 [34]

The results for the CD-triaxial test on the loose specimen of the BC36 sample are plotted in Appendix D.2.2 and the results of the CD-triaxial tests on the specimens of the AZ28 sample can be seen in Appendix D.2.3.

6.3.4 KIM-parameters

After the hypoplastic constitutive model was calibrated for both samples, the numerical simulations of the Spherical Cavity Expansion (SCE) were carried out with a finite difference code written by Dr. Osinov [40], [42]. Figure 6.11 shows the results of these simulations for the sample retrieved from box BC36. The graph for the AZ28 sample is shown in Appendix D.3.1. Every dot on the graph represents one solution of the spherical cavity expansion with a certain relative density D_r and a certain initial effective mean pressure p'_0. The numerical computations were carried out for a range of D_r-values beginning at $D_r = 0\%$ and successively increasing it in steps of 10% to a maximum possible value of 100%. For each D_r-value, the simulation was run with five different mean effective pressures p'_0 ranging from $p'_0 = 0.025$ MPa to $p'_0 = 0.30$ MPa amounting to a total of 50 simulations. Table 6.6 lists the six desired KIM-parameters a_i and b_i (with $i = 1, 2, 3$) which are obtained by curve fitting the results of the simulations.

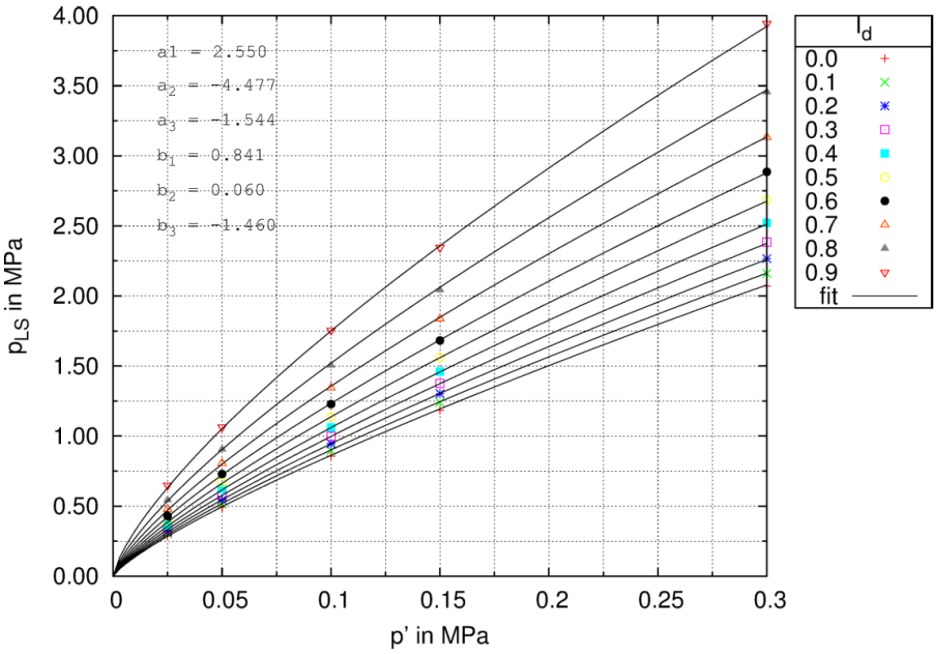

FIGURE 6.11: Results of the simulations of the SCE for the sample from box BC36 [34]. Note that $I_d = D_r$.

In comparison to the differences between the basic soil- (Table 6.3) and hypoplastic parameters (Table 6.5), the differences between the a_i and b_i values of the two materials increase significantly. Since the two sand samples are practically identical, it is assumed that the discrepancies originate in the mentioned difficulties with the calibration of the hypoplastic parameters due to the extensive grain crushing. Inaccuracies connected to curve fitting the a_i and b_i parameters are believed to be another source of the variations of these parameters.

The simulations of the Spherical Cavity Expansion in Ticino sand were performed by Cudmani [5]. Even though the values vary slightly, a clear difference between the

calcareous and the silica sands can not be identified just by looking at the single parameters.

Table 6.6: Results of the SCE simulations carried out for both samples [34]

box	$CaCO_3$ [%]	a_1	a_2	a_3	b_1	b_2	b_3
Ticino [5]	-	3.055	-6.686	-1.355	0.794	0.133	-1.379
AZ28	100	1.666	-6.152	-1.597	0.835	0.073	-1.395
BC36	100	2.550	-4.477	-1.544	0.841	0.060	-1.460
Δ [%]	0.00	53.36	-27.23	-3.32	0.72	-17.81	4.66

6.3.5 Cone resistance curves calculated with the KIM

After the laboratory tests, evaluations and simulations on the samples are completed and all necessary parameters have been determined, the cone resistance for any desired relative density and depth can be calculated. Figure 6.12 shows the q_c-curves computed with the values of the AZ28, BC36 and the Ticino sample to a depth of 10 m and a relative density of $D_r = 60\%$. The post-compaction CPTs performed in each box are also plotted to show how they compare to the q_c-curves calculated with the KIM. The dashed red line is the performance line provided by the client and calculated according to Chapter 6.1.2. While the post-compaction cone resistance measured in box AZ28 fulfills the requirements, the values measured in box BC36 are below the required level between a depth of 1.38 m and 1.50 m. Even though the required q_c-levels were not reached over a length of 12 cm only, that was enough for the client to not accept the performed compaction work as sufficient and demand recompaction. As Figure 6.12 proves, the compaction works would have been accepted if the requirements would have been calculated with the KIM. This is a good example to show why it important to have a site-specific correlation between the cone resistance q_c and the relative density D_r.

The cone resistance lines calculated with the KIM for the samples from AZ28 and BC36 also show how the results of the KIM vary even though, as shown in Table 6.3 and Figure 6.7, the two samples are more less identical. At a depth of 10 m, the q_c-values of the two samples are $q_c = 5.95$ MPa for the AZ28 sample and $q_c = 4.60$ MPa for the BC36 sample, differing by 1.35 MPa.

The curve calculated with the parameters of the silica Ticino sand resulted in q_c-values significantly higher than the values for the PLM samples. One cause of this difference are the lower values of the void ratios e_{min} and e_{max} and friction angle φ_c of the silica sand which lead to a higher mean effective pressure p'_0 and therewith to a higher cone resistance q_c resulting from the KIM analysis. Another reason for the higher results of Ticino sand are the KIM-parameter a and b calculated with Equation 4.15. Together with the mean effective pressure p'_0, these two parameters are employed in Equation 5.10 to calculate the limit pressure p_{LS}. Parameter a of Ticino sand is higher whereas

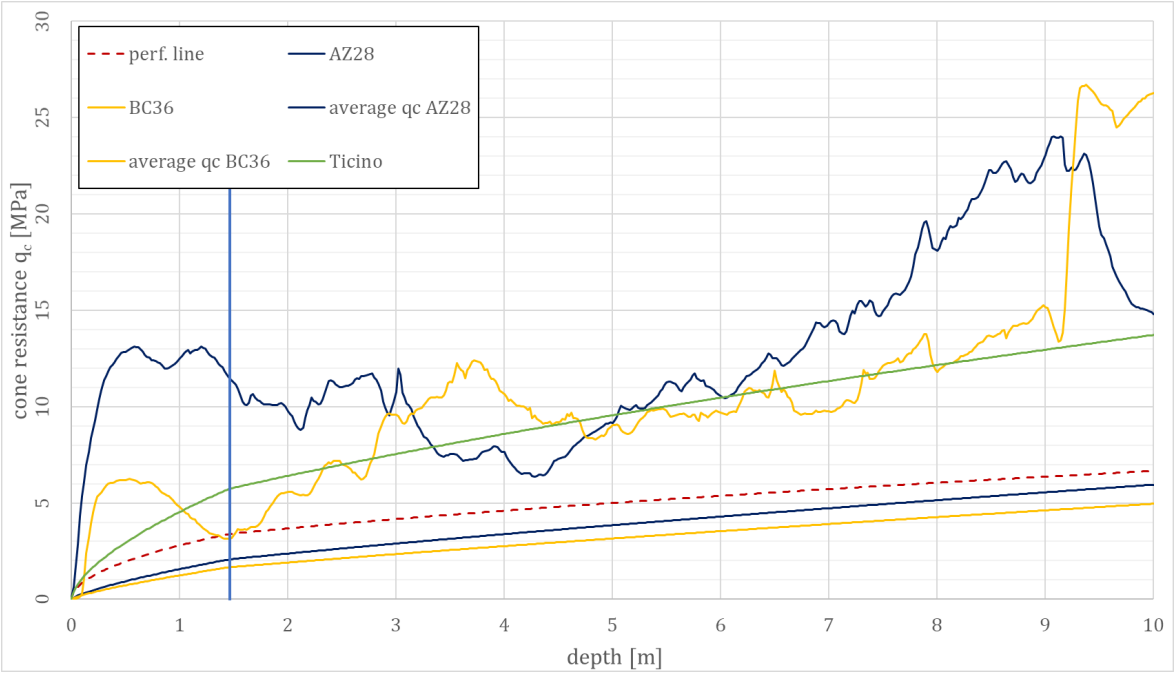

FIGURE 6.12: Cone resistance curves calculated with the KIM for both samples from the investigated project and Ticino sand

parameter b of the silica sand is lower than the respective calcareous counterparts. As was discussed in Chapter 5.3, a high value of parameter a and a low value of parameter b lead to a high cone resistance q_c.

TABLE 6.7: Main components of the KIM-equation calculated for a depth of 10 m and a relative density of $D_r = 60$ %

Material	$CaCO_3$ [%]	γ [kN/m^3]	p'_0 [kPa]	a [-]	b [-]	p_{LS} [MPa]	$q_{c,KIM}$ [MPa]
Ticino	-	18.52	71.89	11.911	0.623	2.308	13.718
AZ28	100	17.19	62.71	7.837	0.743	1.001	5.947
BC36	100	16.52	60.07	7.298	0.771	0.834	4.597

6.3.6 In-situ density tests in box AZ28

In the previous chapter, the cone resistance q_c was calculated for a certain relative density D_r. The KIM can also be used to do the inverse operation and calculate the relative density corresponding to a certain cone resistance. This was done for the results of the CPT performed after the compaction works in box AZ28 were completed. To verify the results of these calculations, the in-situ density was determined with a series of core-cutter tests. The procedure will be briefly explained in this chapter.

The core-cutter test is best suited for determining the in-situ density in cohesive soil but can also be applied in fine- to medium-grained sands. In the core-cutter test according to DIN 18125 (or ÖNORM 4414), a standardized steel cylinder is driven vertically into the soil with the help of guiding cylinder and a hammer. Figure 6.13 shows the basic setup of such a test.

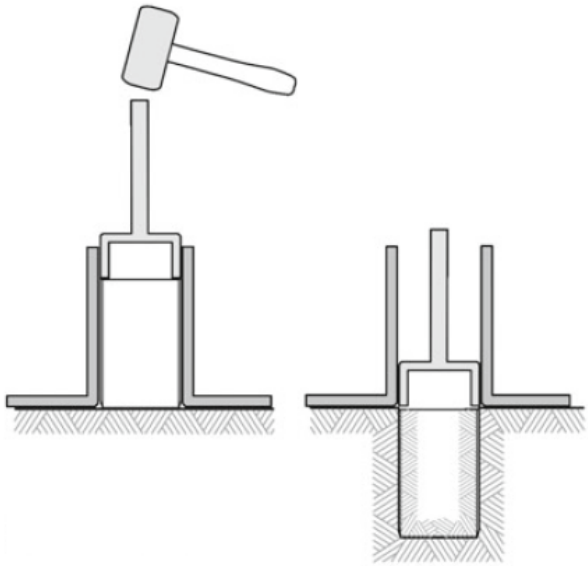

FIGURE 6.13: Basic setup of the core-cutter sampling method [48]

After the cylinder is filled, it is carefully excavated and the sample is retrieved. It is important that the soil sample in the cylinder is disturbed as little as possible during the driving and the excavation process. This is why the core-cutter method is not suitable for coarse-grained soils with a significant amount of gravel because the coarse grains would disturb the sample and distort the outcome of the density calculation. After the sample has carefully been excavated and its mass has been determined, the in-situ density ρ is defined by the ratio between the mass m of the soil sample and the volume of the core-cutter cylinder V_{cyl}.

A total of five cylinders with different diameters and heights were produced by the KELLER workshop for the tests. Steel pipes which were readily available at the workshop were cut to the desired length and one edge of the cylinders was sharpened to ease the penetration into the ground. Table 6.8 list the dimensions of all five cylinders.

The samples were taken close to the CPT location in box AZ28 in a depth ranging from the surface down to 170 cm. Shovels and a wheel-loader were used for the excavation to the desired depth where a core-cutter cylinder was placed on an even plane and a sledgehammer was used to drive it into the ground. After the cylinder was fully buried in the ground, the soil around it was removed and a metal plate was carefully pushed underneath it. Together with the metal plate, the cylinder was then lifted out of the ditch and the top and bottom surfaces were trimmed before the sand inside the cylinder was removed and carefully filled into sealable plastic bags. The plastic bags were necessary to make sure that the samples do not dry out and retain their natural moisture content. This way, a total of nine samples were taken.

TABLE 6.8: Dimensions of the core-cutter cylinders used for the in-situ density tests in box AZ28

cylinder	*diameter* [cm]		*wall thickness*	*height*	*mass*	*volume*
	inner	outter	[cm]	[cm]	[g]	[cm^3]
1	27	26.2	0.4	10	2924	5391.29
2	27	26.2	0.4	15	4438	8086.93
3	20	19.6	0.2	20	2367	6034.37
4	20	19.6	0.2	15	1775	4525.78
5	15	14.2	0.4	14.5	2109	2296.30

For the determination of the moisture content w of each sample, three times 300 g of every sample were dried for 3 hours at a temperature of around 120° Celsius in a common gas oven. By measuring the wet mass m of the specimens before and the dry mass m_d after drying, the mass of the water m_w was weighed. Now, all necessary parameters for the calculation of the relative density D_r were determined.

First, the in-situ density ρ and the dry density ρ_d were calculated with the equations:

$$\rho = \frac{m}{V_{cyl}} \qquad \rho_d = \frac{m_d}{V_{cyl}} \tag{6.5}$$

With the dry density ρ_d and the grain density ρ_s determined by the laboratory, the in-situ void ratio e was calculated:

$$e = \frac{\rho_s}{\rho_d} - 1 \tag{6.6}$$

Finally, the limit void ratios e_{min} and e_{max} from the lab-tests and the calculated in-situ void ratio e were used to compute the relative density D_r:

$$D_r = \frac{e_{max} - e}{e_{max} - e_{min}} \tag{6.7}$$

Table 6.9 shows the results of the density calculations for all nine samples. As can be seen, there is a strong discrepancy between the values of the relative densities. The relative density calculated for the top 20 cm is assumed to be too high while the values in the layers below are considered too low. As illustrated in Figure 6.13, a guidance cylinder is usually used to keep the cutter-cylinders vertical during the hammering to ensure that the soil sample is not disturbed. No such guidance cylinder was available for the tests performed in box AZ28 and the cylinders were tipping with every blow from the hammer. In addition to the vibrations from the hammering, it is believed that the tipping of the cylinders broke up the densified sand and loosened it causing the results of the in-situ and relative density calculations to be too low. Due to heavy

machinery passing over it, the top 20 cm of sand were denser and the tipping of the cylinders was not as distinct as in the deeper layers. However, the calculated values of the relative density are still unrealistically high. The incorrect results could be caused by the material's strong tendency to particle crushing described in Chapter 6.3.3. Crushing of sand particles, especially larger sea-shells, leads to a finer material which entails lower values of e_{min} and e_{max}. That would mean that the e_{min} and e_{max} values determined by the laboratory are not correct for the sand at the surface and are therefore invalid for the calculation of the in-situ relative density. It is also assumed that inaccuracies in the determination of the limit void ratios e_{min} and e_{max} described by Hamidi [49] and Tavenas [50] play a role in this.

Table 6.9: Dimensions of the core-cutter cylinders used for the in-situ density tests in box AZ28

sample	*depth*	V	m	m_d	w	ρ	ρ_d	e	D_r
	[cm]	[cm^3]	[g]		[%]	[g/cm^3]		[-]	[%]
1	0	5391.29	9123.33	8674.78	5.17	1.69	1.61	0.735	101.04
2	0	2296.33	3698.33	3575.03	3.45	1.61	1.56	0.793	89.88
3	20	4525.78	7516.67	7257.74	3.57	1.66	1.60	0.740	99.92
4	70	6034.37	8814.67	8334.73	5.76	1.46	1.38	1.021	46.12
5	90	4525.78	6739.00	6379.59	5.63	1.49	1.41	0.980	53.94
6	100	8086.93	12051.33	11217.73	7.43	1.49	1.39	1.01	47.78
7	120	4525.78	6744.00	6309.37	6.89	1.49	1.39	1.00	49.71
8	150	6034.37	8932.33	8053.96	10.91	1.48	1.34	1.09	32.60
9	170	4525.78	6862.67	6252.63	9.76	1.52	1.38	1.02	46.22

Better results of the in-situ density test would be achieved if the core-cutter cylinders could be prevented from tipping and disturbing the sample during the hammering with a guiding cylinder. In addition to that, the results would be more accurate if the weighing and drying of the samples was carried out with a proper laboratory scale and oven instead of household equipment. It is believed that determining the in-situ density with a different method and in a more professional way would improve the results. Due to the large amount of sea-shells and coral lumps mentioned in Chapter 6.2.2, the core-cutter test might not be the best suited method to determine the in-situ density in this case. The sand replacement method might be more suitable for this case and deliver more accurate results. However, the sand replacement method is more laborious and requires more equipment than the core-cutter method.

Figure 6.14 compares the results of the in-situ density tests with the relative density back-calculated with the KIM on the basis of the cone resistance values measured in a post-compaction CPT. For the observed depth from 0 m down to 2 m, the relative density derived with the KIM reaches unrealistic values above 100% and shows significant differences to the results of the in-situ density tests.

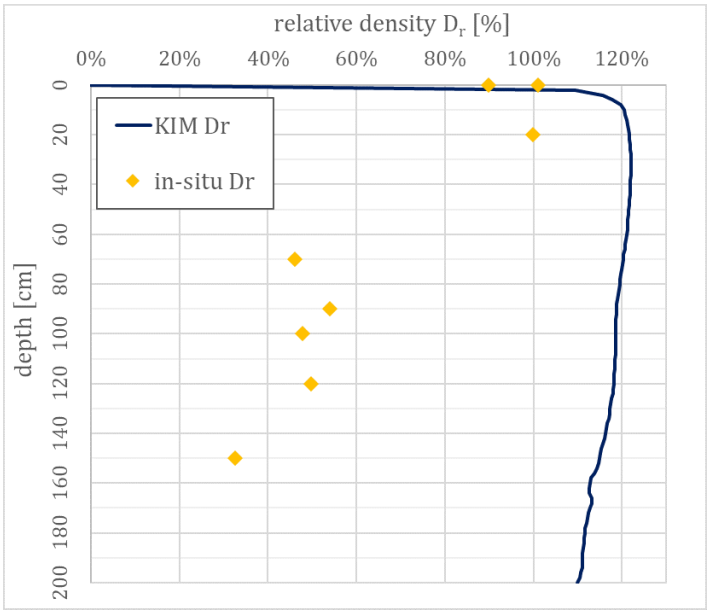

FIGURE 6.14: Results of the in-situ density tests compared to the relative density back-calculated with the KIM in box AZ28

The testing location where the post-compaction CPT was performed and the soil samples were taken was right next to a construction road with constant traffic of heavy machinery. In addition to that, it is explained in Chapter 2.1.3 how the newly reclaimed land is leveled with bulldozers. The constant stress induced by the bulldozers and the heavy construction machinery might have caused extensive grain crushing and alteration of the material in the top 2 m of the fill. The KIM parameters, however, were determined on a sample taken soon after the land was reclaimed and before there was any construction traffic. Differences in the granulometric properties between the sample-material and the later material might be an explanation for the unrealistically high values of the relative density calculated with the KIM.

6.3.7 Recommendations to apply the KIM

Based on the results presented in the previous chapters, a list of recommendations to apply the KIM was prepared. This list sums up the procedure of the application of the KIM at the case-study project in Dubai and what to consider during the sampling process.

1. **Assess carbonate content and grain size distribution of soil**

   As explained in Chapter 5.4.1, the results of the KIM decline with the increase of the carbonate content once the carbonate content in the soil crosses a threshold value of around 50%. It is assumed that the mechanical behavior of the sand is controlled by the carbonate fraction once the carbonate content is above 50%. If this is the case for the investigated project, traditional correlations between the cone resistance q_c and the relative density D_r might not be applicable because

calcareous sands develop significantly lower q_c-values compared to silica sands under similar conditions [3], [4] and might therefore lead to q_c-requirements difficult to reach. In this case, a site-specific correlation established by the KIM could reproduce the specific properties of the calcareous sand and allow to calculate realistic q_c-requirements.

Chapter 6.3 shows that the laboratory has to remove sand grains larger than d > 8 mm from the PLM samples because of limitations of the dimensions of the test equipment. Meier [16] found that if a sample contains more than 20% of coarse material, the cone resistance measured in a calibration chamber will increase by 20% in comparison to a material with 5% coarse material. That means applying the KIM on a material from which more than 20% of the material had to be removed will likely underestimate the resulting q_c-values.

In the previous projects performed by KELLER, 22 % of the sand grains from the sample from the Palm Jumeirah project were larger than d < 4 mm and had to be removed. The removal of this amount of coarse grains cannot be neglected so the soil mechanics laboratory suggested to apply a reduction factor of 0.8 to the measured q_c-values before calculating the relative density D_r.

The maximum value of the sand grain diameter d_{max} is determined by the soil mechanics laboratory and is based on the dimensions of the available test equipment and ranges between $4 \leq d_{max} \leq 8$ mm for the projects in the database.

2. **Take samples from site**

   The necessary parameters are not state-dependent and can be determined on disturbed sand samples taken from the investigated site. Because larger and heavier sea-shells and coral fragments tend to accumulate on the surface, the sample should be taken from a depth of approximately 1 m. Parameters determined on coarse material taken from the surface might not adequately represent the mechanical behavior of the rest of the fill in the SCE-simulation and therefore lead to wrong results. As was explained under point number 1, samples with a high content of coarse grains will likely underestimate the resulting q_c-values.

   The sand used as hydraulic fill might sometimes be dredged from different areas on the seafloor and can therefore have different properties. If the parameters of the sand are suspected to vary, it is recommended to take a sample from each of the different materials and compare the results of the laboratory tests. It is then possible to calculate a q_c-requirement for each of the different materials found on site. To make sure the laboratory has enough sample material to perform the tests on, at least 20 kg of sand should be retrieved from each sampling location. Durable plastic bags or sealable buckets are suitable containers for the samples.

3. **Determine soil properties and calibrate hypoplastic model**

   After the samples have been retrieved from the site and sent to the laboratory, the hypoplastic model parameters can be determined according to the procedure explained in Chapter 4.2.2. As Mengé [47] writes, it is important to consider the crushability of the calcareous sand grains in the determination of the densest

and loosest packing e_{min} and e_{max} and the Proctor density ρ_{Pr}. The hypoplastic parameters e_{d0}, e_{c0} and e_{i0} are determined from e_{min} and e_{max} and significantly influence the behavior and results of the hypoplastic model (see Chapter 4.2.2). The values of e_{min} and e_{max} will be lower due to the crushing of sand grains which affects the calculation of the unit weight γ and, further on, the result of the KIM (see Chapter 5.5).

While the crushing of sand grains is not desired when determining the limit void ratios, it is advised when performing the one-dimensional compression test. The maximum pressure should be in the range of the expected cone resistance values measured in the field to capture the effects of fracturing grains on the compressibility of the sample. It is recommended to perform one-dimensional compression tests with a pressure of up to 25 MPa.

Evaluating the results of the performed lab tests yields the necessary hypoplastic parameters for the constitutive equation. As Meier [16] states, the quality of the hypoplastic model and therefore, the results of the subsequent numerical calculations, depends on the calibration of the material parameters. Especially the two compressibility parameters, granulate hardness h_s and exponent n, which are found by curve fitting the results of one-dimensional compression tests, determine how well the crushability of the sand grains can be reproduced by the hypoplastic equation. It is therefore recommended to focus on the calibration of these two parameters.

4. **Perform a series of simulations of the Spherical Cavity Expansion problem**

   The six KIM-parameters a_i and b_i (with $i = 1, 2, 3$) are determined by curve fitting the results of simulations of the SCE carried out with a FE-code developed by Osinov [42]. To cover a realistic range of the mean pressure p' and the relative density D_r, the simulations are carried out with different initial conditions. For the projects in the database, the KIM-parameters were found by performing 50 simulations (per sample) with an initial mean pressure of $p'_0 = 0.025$, 0.05, 0.10, 0.15 and 0.30 MPa and a relative density ranging from $D_r = 0\%$ to 90%.

5. **Calculate KIM q_c-curve with the obtained parameters**

   With the parameters obtained from the previously described steps and the equations presented in Chapter 4.5, it is possible to calculate the cone resistance curve corresponding to any desired relative density D_r for the investigated project.

7 Conclusion and outlook

In the last chapter of this thesis, a conclusion, summing up the main results, is drawn and an outlook for further research concerning the KIM is given.

7.1 Conclusion

The goal of the thesis at hand was to find out if the KIM is an adequate method to derive the relative density from CPT-results in calcareous sands and in what circumstances it is recommended to apply the Karlsruhe Interpretation Method.

By analyzing parameter sets of various calcareous sands found in literature it was found that these sands, in general, have higher void ratios e_{min} and e_{max}, higher critical friction angles φ_c and a higher grain density ρ_s. It is also shown that these parameters increase with an increasing carbonate content which is attributed to the mineralogical and granulometric properties of these sands.

On that basis, the procedure of determining the eight necessary parameters for the hypoplastic constitutive equation was investigated and it was found that, apart from the oedometer test, the procedure is the same as for silica sands. In the oedometer test, the maximum vertical pressure σ_v should be as high as 25 MPa in order to include the effects of potential crushing of the calcareous sand grains in the hypoplastic model. Compared to silica sands, the hypoplastic parameters representing the compressibility, granulate hardness h_s and exponent n, show the biggest differences. Presumably because of the different mineralogy of silica sands, h_s is usually lower whereas exponent n tends to be higher in calcareous sands implying that the compression curves are steeper in this material.

The parameters of the calcareous sand samples in the KELLER database were analyzed and it was shown how the initial soil parameters influence the result of the calculation of the mean effective pressure p'_0 and how their effect propagates to the final result of q_c. The effect of each input parameter can be explained with the respective equations and the resulting value of p'_0 can be predicted quite accurately. It was also tried to find the influence of the basic soil properties (e.g. e_{min}, e_{max}, φ etc.) on the KIM parameters a_i and b_i but, unfortunately, the connection between the soil properties and KIM parameters could not be resolved in a satisfactory way.

Another goal of this thesis was to find out which soil parameters significantly influence the results of the KIM. It was possible to show that the carbonate content can serve as an indicator for the magnitude of the resulting cone resistance q_c. By relating the

decisive parameters of each project in the database to the respective carbonate content, it was demonstrated that an increasing carbonate content correlates with a decrease of the mean effective pressure p'_0, the limit pressure p_{LS} and, ultimately, the cone resistance q_c.

The findings presented in this thesis indicate that the use of the Karlsruhe Interpretation Method is most beneficial for the contractor in calcareous sands with a high carbonate content as this, in general, guarantees low required cone resistances. Another advantage is that the KIM-parameters are derived anew for every site and therefore produce a site-specific q_c-requirement for every project taking into account the characteristics of the material present on site. The results of the KIM therefore display the actual material behavior. This is a strong argument against the use of other CPT interpretation methods like the equation by Schmertmann [1] or Jamiolkowski [2] which are based on calibration chamber tests on silica sands and do not incorporate the specific characteristics of calcareous sands.

7.2 Outlook

The work described in this thesis is a first step towards a deeper understanding of using the Karlsruhe Interpretation Method to derive a compaction criterion in calcareous sands. It has been shown that the KIM has certain advantages over other CPT interpretation methods when it comes to the realistic reproduction of the specific characteristics of calcareous sand. However, some unanswered questions still remain and further research concerning the KIM is necessary to substantiate the findings presented in this thesis. Based on the results and conclusions presented in this work, further development steps have to be investigated:

- **Expand database with samples from future projects**

  So far, the KELLER database is comprised of soil-, hypoplastic- and KIM-parameters of 11 sand samples from different projects. Following the process described in Chapter 6, additional sand samples should be taken from future vibro-compaction projects to expand the database and underpin the findings so far.

- **Perform thorough sensitivity analysis to find connection between soil properties and KIM-parameters**

  Throughout the thesis at hand, the influence of the basic soil properties (e.g. e_{min}, e_{max}, φ etc.) on the hypoplastic and KIM parameters was investigated. The relations between the soil and hypoplastic parameters are explained in Chapter 4.2 but, unfortunately, the connection between the soil properties and KIM parameters could not be resolved in a satisfactory way. By conducting a thorough sensitivity analysis, ambiguities concerning these connections could be cleared up.

  The sensitivity analysis could be based either on a new set of parameters or on one of the data-sets from the database. To understand the influence of each of

the initial soil properties on the KIM-parameters, it is essential that the whole calibration and simulation procedure is carried out. That means, for example, increase e_{min} within a reasonable range while all other parameters remain the same. Then, based on the modified data-set, calibrate the hypoplastic model parameters and perform the simulation of the spherical cavity expansion to obtain the corresponding values of a_i and b_i (with $i = 1, 2, 3$). This procedure has to be carried out for every variation of one of the initial parameters

The soil mechanics laboratory that was assigned to determine the relevant material and model parameters for the KIM in the past, uses a Finite-Element-code developed by Osinov [42] to perform a series of numerical simulations of the spherical cavity expansion problem and obtain the values of a_i and b_i. The sensitivity analysis described above should either be performed with the code from Dr. Osinov or a similar FE-application that is able to model the spherical cavity expansion with a hypoplastic constitutive equation.

- **Establish a new shape factor k_q for calcareous sands**

  As is explained in Chapter 4.4, the shape factor k_q was developed based on the results of CCTs performed on nine different sands of which only two (Quiou and Dogs Bay sand) were of carbonate origin. By gathering results from calibration chamber tests performed on calcareous sands (e.g. Meier [16], Wehr [22]) and solving the corresponding spherical cavity expansion problem to obtain the limit p_{LS}, a new shape factor specifically suited for calcareous sands could be developed. In addition to the CCT results from literature, a series of CCTs on calcareous sand samples from the Middle East could also be performed.

- **Apply other hypoplastic constitutive equation**

  The indestructibility of the sand grains is one of the premises of the hypoplastic model developed by von Wolffersdorff [25] (see Chapter 4.2). However, calcareous sands show a strong tendency to grain crushing (see Chapter 3.3). A hypoplastic model which incorporates the effects of grain crushing at high stress levels, like the one proposed by Engin and Jostad [51], could be applied to numerically investigate the effects of grain crushing on the KIM-parameters and the results of the KIM.

A Appendix for Chapter 3

Table A.1: Calcareous sands and their properties found in literature

Material	$CaCO_3$	φ_c	e_{min}	e_{max}	ρ_s	*source*
	[%]	[°]	[-]		[g/cm^3]	
M0 Karlsruhe	0	31	0.531	0.875	2.647	[16]
Al Zour LNG	9.73	31	0.365	0.747	2.663	KELLER
Jurong sand	11	33	0.690	1.030	-	[16]
M15	13.5	31.1	0.579	0.859	2.671	[16]
M30	27	31.6	0.618	0.948	2.694	[16]
Sheikh Jaber	28.6	31	0.385	1.015	2.650	KELLER
Al Zour Package 5	42.45	33	0.410	0.84	2.670	KELLER
M60	54	32.2	0.653	1.014	2.742	[16]
JAT4: island	60.9	34.5	0.680	0.977	2.749	KELLER
JAT4: south side	63.3	39.5	0.979	1.504	2.777	KELLER
Palm Jumeirah	73.6	35	0.583	0.922	2.741	KELLER
Quiou	77	36	0.831	1.281	2.662	[5]
M100 Dubai sand	90	37.7	0.762	1.223	2.805	[16]
Dogs Bay	90	40.3	0.981	1.827	2.750	[5]
Cabo Rojo	92.8	-	1.340	1.710	2.860	[52]
BAE	93	-	0.979	1.551	2.840	[52]
S1	95	-	0.741	1.278	2.840	[52]
Palm Deira	96.2	36	0.725	1.226	2.800	KELLER
Kenya sand	97	-	1.282	1.776	2.785	[52]
BAW	98	-	0.843	1.392	2.840	[52]
PLM - AZ28	100	36.3	0.740	1.261	2.791	KELLER
PLM - BC36	100	36.5	0.79	1.384	2.791	KELLER
Zakkum Island	100	34	0.831	1.338	2.833	KELLER

B Appendix for Chapter 4

B.1 Hypoplastic parameters for all projects in the KELLER-database

TABLE B.1: Comparison between the hypoplastic parameters of all projects in the KELLER-database

Material	$CaCO_3$	φ_c	e_{d0}	e_{c0}	e_{i0}	h_s	n	α	β
	[%]	[°]		[-]		[MPa]		[-]	
Al Zour LNG	9.73	31	0.365	0.747	0.859	102	0.542	0.095	1.43
Sheikh Jaber	28.6	31	0.385	1.015	1.167	40	0.375	0.140	1.40
Al Zour Package 5	42.45	33	0.41	0.84	0.966	175	0.483	0.130	1.74
JAT4: island	60.9	34.5	0.68	0.977	1.124	80	0.550	0.150	1.20
JAT4: south side	63.3	39.5	0.979	1.504	1.729	28	0.500	0.500	0.10
Palm Jumeirah	73.6	35	0.583	0.922	1.060	270	0.430	0.140	0.17
M100 Dubai sand	90	37.7	0.762	1.223	1.406	95	0.500	0.130	1.10
Palm Deira	96.2	36	0.725	1.226	1.410	80	0.480	0.230	0.70
PLM - AZ28	100	36.3	0.740	1.261	1.450	39	0.525	0.050	1.97
PLM - BC36	100	36.5	0.79	1.384	1.592	49	0.480	0.045	1.40
Zakkum Island	100	34	0.831	1.338	1.540	80	0.440	0.100	1.75

C Appendix for Chapter 5

C.1 Table of the a_i and b_i parameters for all projects in the database

TABLE C.1: Comparison of the KIM-parameters obtained from the SCE performed on the calcareous sands from the KELLER database [34]

Material	$CaCO_3$	a_1	a_2	a_3	b_1	b_2	b_3
Al Zour LNG	9.73	1.526	-6.299	-1.370	*0.826*	0.062	-1.232
Sheikh Jaber CW	28.6	*-25.082*	-215.493	-6.905	**1.183**	**0.716**	*-1.845*
Al Zour Package 5	42.45	0.185	-8.795	**-1.276**	0.879	0.103	-1.248
JAT4: Island	60.93	-0.246	-13.140	-1.996	0.871	0.136	-1.343
JAT4: South Side	63.3	-23.941	*-218.502*	*-7.384*	1.141	0.594	-1.742
Palm Jumeirah	73.6	2.227	-7.917	-1.615	0.876	0.082	-1.303
M100	90	0.772	-8.018	-1.901	0.867	0.196	-1.501
Palm Deira	96.2	-0.827	-12.483	-1.771	0.936	0.199	-1.375
PLM - AZ28	100	1.666	-6.152	-1.597	0.835	0.073	-1.395
PLM - BC36	100	**2.555**	**-4.477**	-1.544	0.841	*0.060*	-1.460
Zakkum Island	100	0.399	-8.528	-1.729	0.905	0.115	**-1.199**
minimum		-25.082	-218.502	-7.384	0.826	0.060	-1.845
maximum		2.555	-4.477	-1.276	1.183	0.716	-1.199
average		-3.706	-46.346	-2.644	0.924	0.212	-1.422
median		0.399	-8.528	-1.729	0.876	0.115	-1.375
std. deviation σ		10.341	84.413	2.237	0.122	0.226	0.207

C.2 Development of the a and b parameters with an increasing relative density D_r

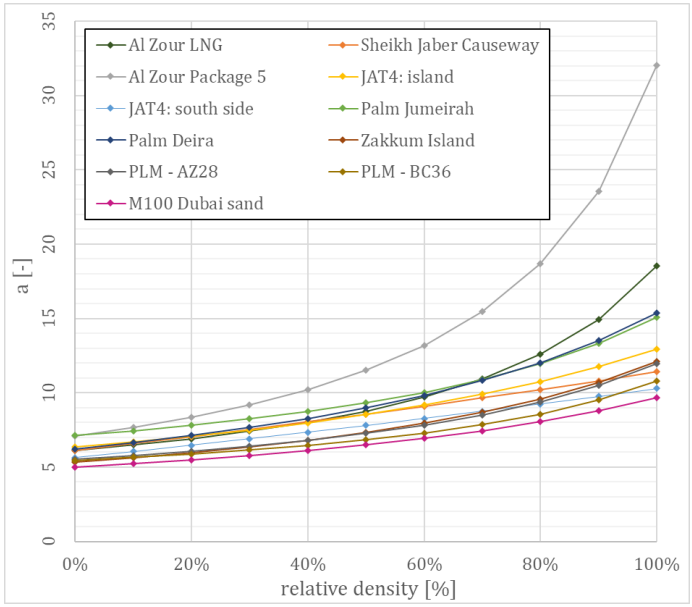

(A)

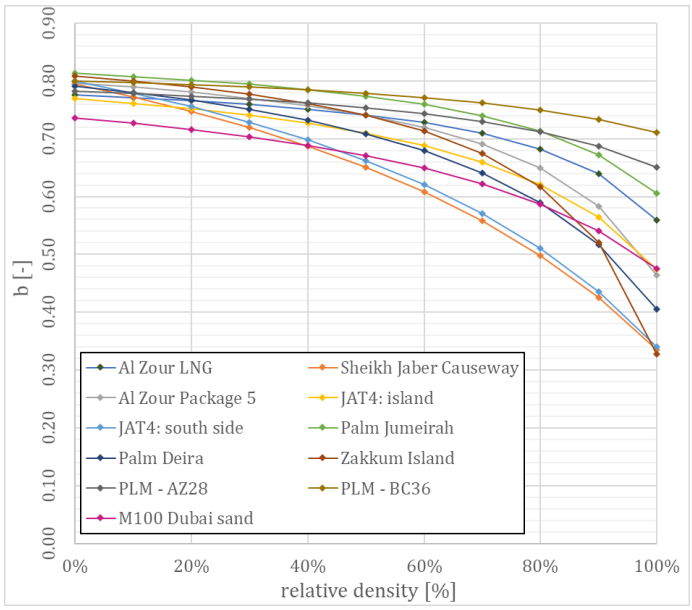

(B)

FIGURE C.1: The influence of the relative density on parameters a and b

C.3 Particle size distribution of the Sheikh Jaber CW sample

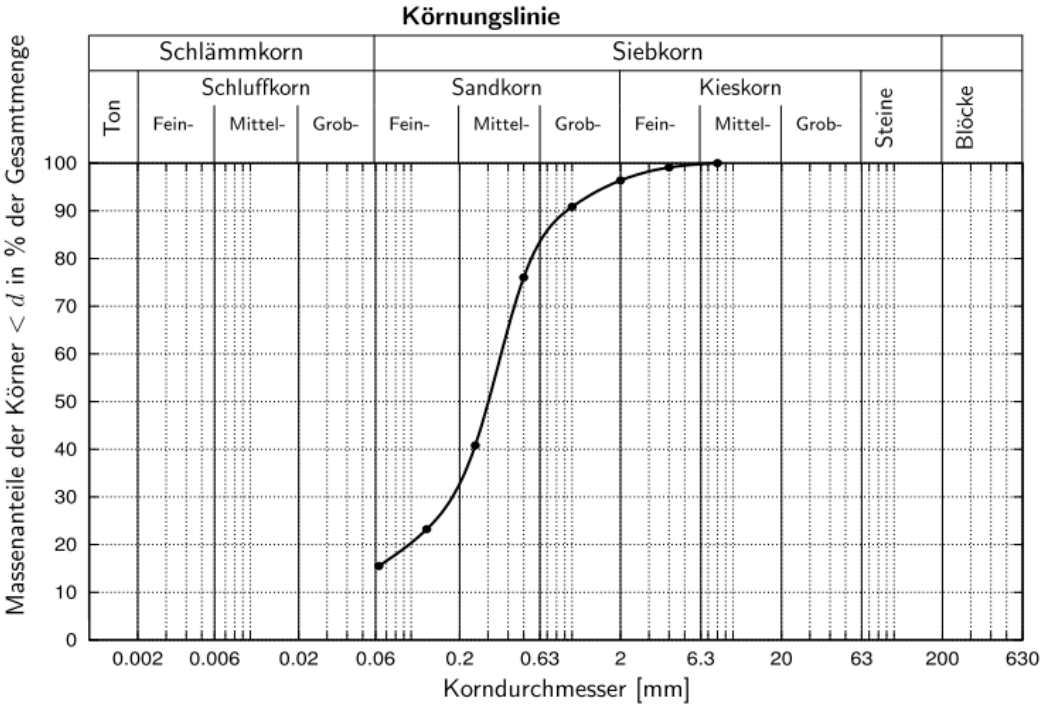

FIGURE C.2: Resulting graph of the particle size distribution of the Sheikh Jaber Causeway sample [34]

C.4 Comparison of the parameters of the M100 and the Palm Deira samples

TABLE C.2: Comparison of soil and hypoplastic parameters of the M100 and the Palm Deira samples

	M100	Palm Deira	Δ[%]
$CaCO_3$	90	96.2	6.89
e_{min}	0.762	0.725	-4.86
e_{max}	1.223	1.226	0.25
φ_c	37.7	36	-4.51
ρ_s [g/cm^3]	2.805	2.800	-0.18
d_{60} [mm]	0.530	0.630	18.87
d_{10} [mm]	0.130	0.143	10.00
e_{i0}	1.406	1.410	0.25
h_s [MPa]	95	80	-15.79
n	0.50	0.48	-4.00
α	0.13	0.23	76.92
β	1.10	0.70	-36.36

TABLE C.3: Comparison of KIM-parameters of the M100 and the Palm Deira samples. The q_c-value is calculated for a depth of 10 m

	M100	Palm Deira	Δ[%]
a_1	0.772	-0.827	-207.18
a_2	-8.018	-12.483	55.69
a_3	-1.901	-1.771	-6.82
b_1	0.867	0.936	8.01
b_2	0.196	0.199	1.63
b_3	-1.501	-1.375	-8.41
q_c [MPa]	9.387	12.734	35.66

C.5 Comparison of the incorrect and recalibrated parameters of the PLM AZ28 sample

TABLE C.4: Comparison of the incorrect and re-calibrated hypoplastic parameters of the PLM AZ28 sample

	incorrect	re-calibrated	Δ[%]
φ_c	36.3	36.3	0.0
e_{d0}	0.74	0.74	0.0
e_{c0}	1.261	1.261	0.0
e_{i0}	1.45	1.45	0.0
h_s [MPa]	39	39	0.0
n	0.525	0.525	0.0
α	0.23	0.05	-78.26
β	1.97	1.97	0.0

TABLE C.5: Comparison of the incorrect and re-calibrated KIM-parameters of the PLM AZ28 sample. The q_c-value is calculated for a depth of 10 m.

	incorrect	re-calibrated	Δ[%]
a_1	-0.587	1.666	383.82
a_2	-9.474	-6.152	35.06
a_3	-1.486	-1.597	-7.47
b_1	0.994	0.835	-16.00
b_2	0.301	0.073	-75.75
b_3	-1.459	-1.395	4.39
q_c [MPa]	14.00	8.66	-38.14

C.6 Resulting curves from the variation of the a_i-parameters of the Zakkum Island material

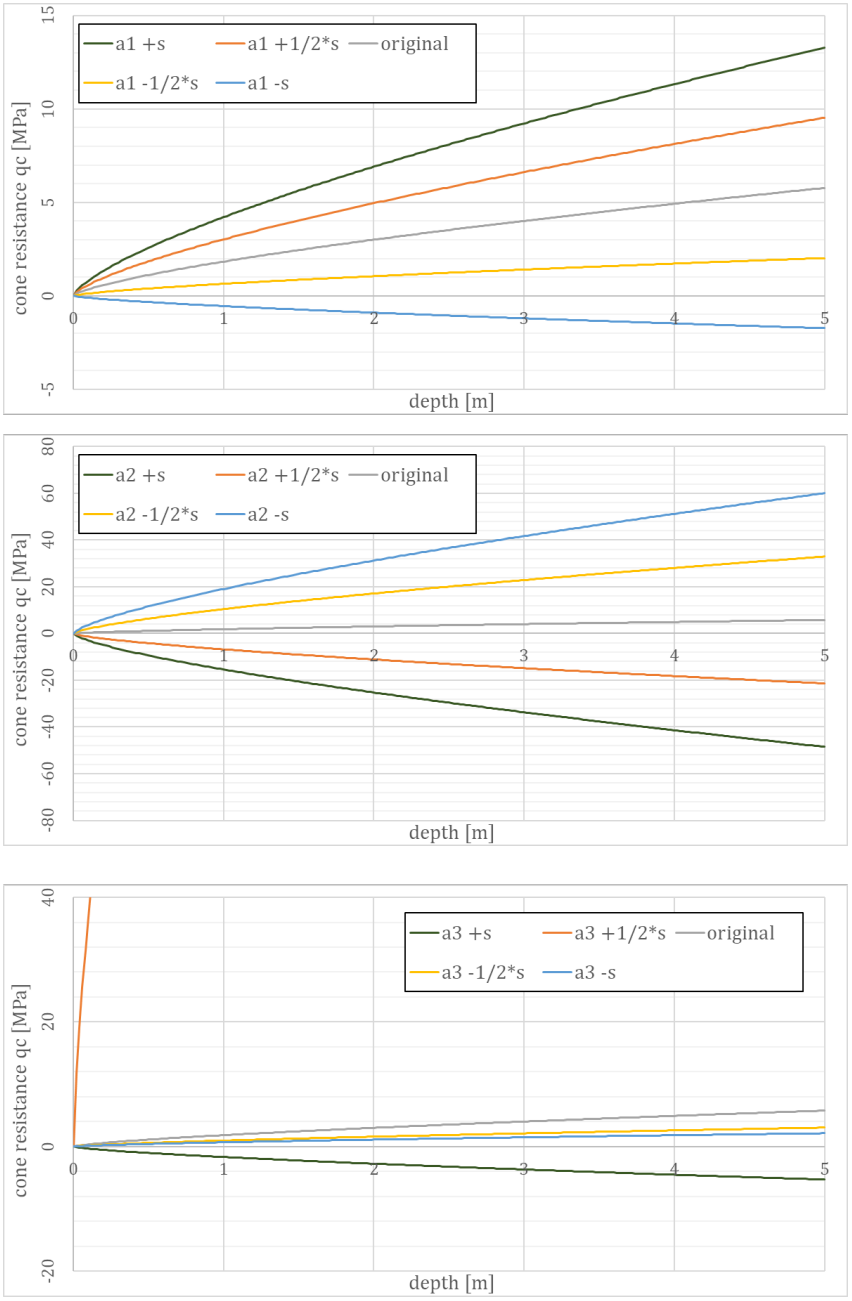

FIGURE C.3: q_c-curves resulting from the sensitivity analysis performed on the Zakkum Island sample

D Appendix for Chapter 6

D.1 Table of the basic laboratory test

TABLE D.1: Lab tests, resulting parameters and corresponding standards

test	*parameter*	*standard*
loosest and densest packing	e_{max} e_{min}	DIN 18126
grain size distribution	d_{60}, d_{30}, d_{10}	DIN 18123
grain density	ρ_s	DIN 18124
maximum dry density	ρ_{Pr}	DIN 18127
carbonate content	% of $CaCO_3$	DIN 18129
2 high-pressure one-dimensional compression tests	h_s, n, β	DIN 18135
4 consolidated-drained triaxial tests	α	DIN 18137-2

D.2 Results of the high-pressure oedometer and the triaxial tests

D.2.1 Results of high-pressure oedometer tests on sample AZ28

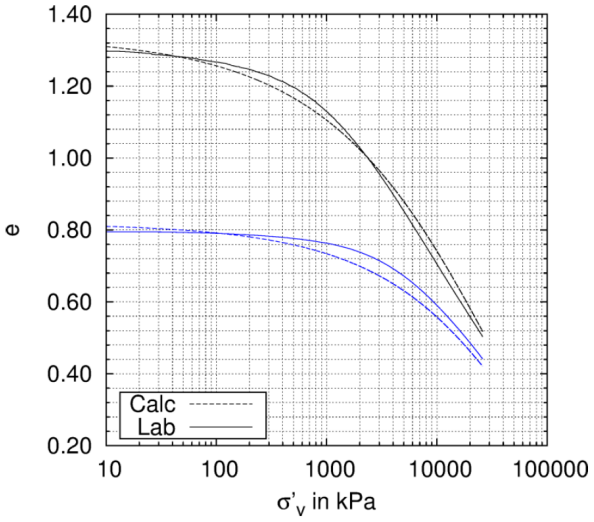

FIGURE D.1: Results of the 1D high-pressure compression test (lab) and the calibration (calc) for the sample from box AZ28 [34]

D.2.2 Results of consolidated-drained triaxial tests on sample BC36

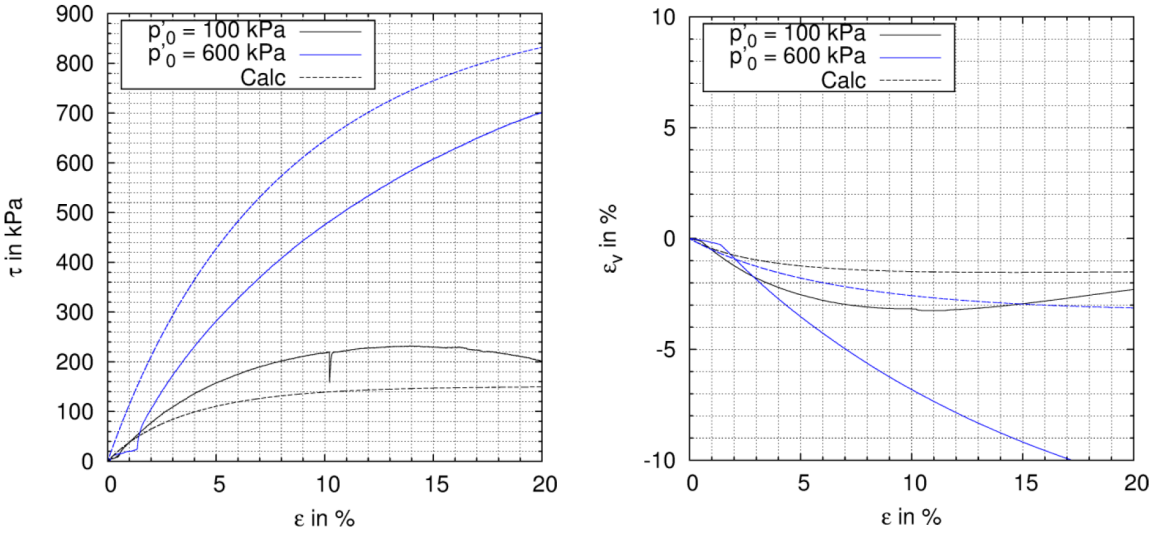

(A) (B)

FIGURE D.2: Results of the consolidated-drained triaxial test on a loose specimen (lab) and the calibration (calc) for the sample from box BC36 [34]

D.2.3 Results of consolidated-drained triaxial tests on sample AZ28

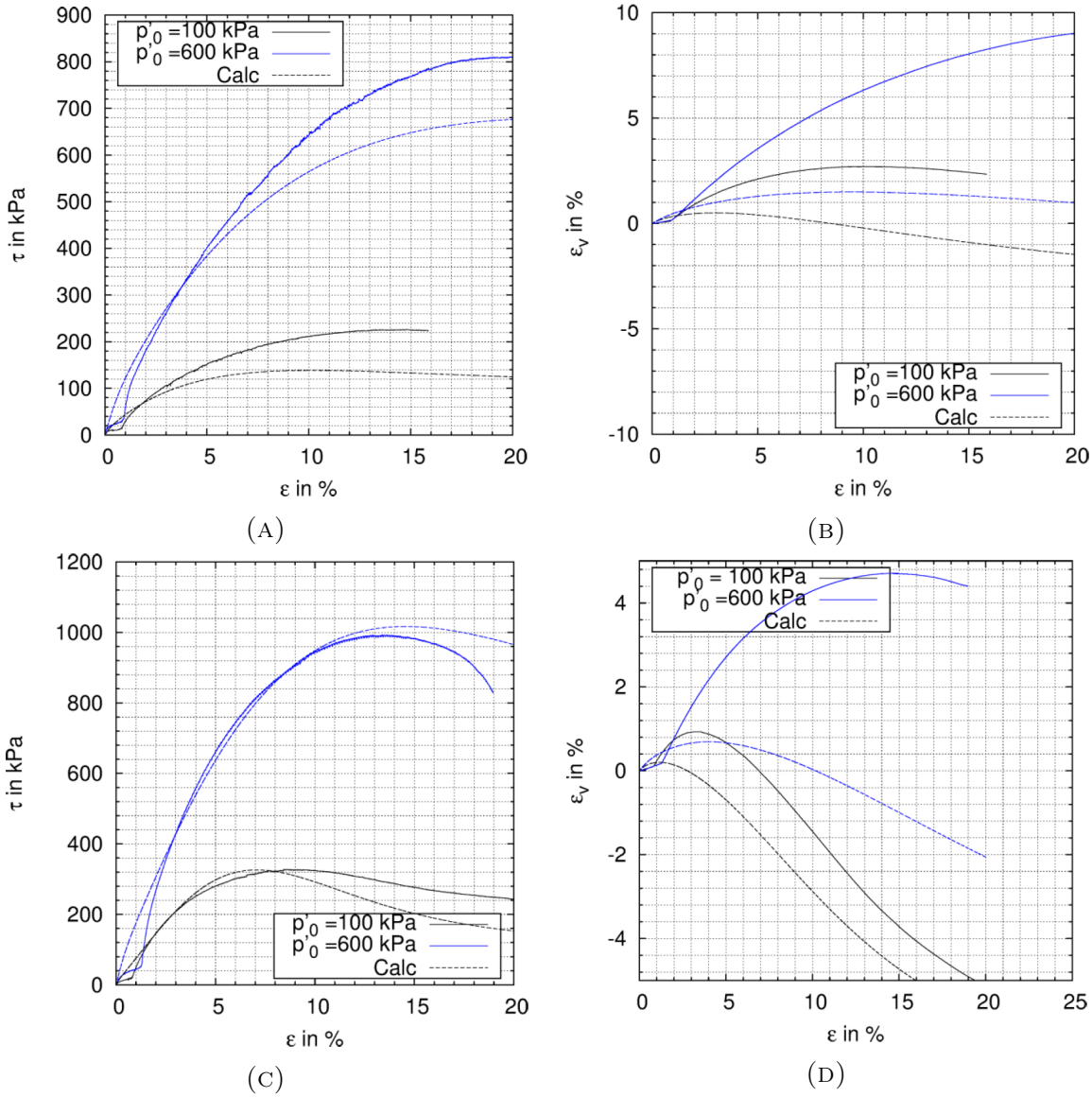

FIGURE D.3: Results of the consolidated-drained triaxial test on a loose ((A) and (B)) and dense ((C) and (D)) specimen (lab) and the calibration (calc) for the sample from box AZ28 [34]

D.3 Results of the simulations of the Spherical Cavity Expansion

D.3.1 Results of the Spherical Cavity Expansion simulations for sample AZ28

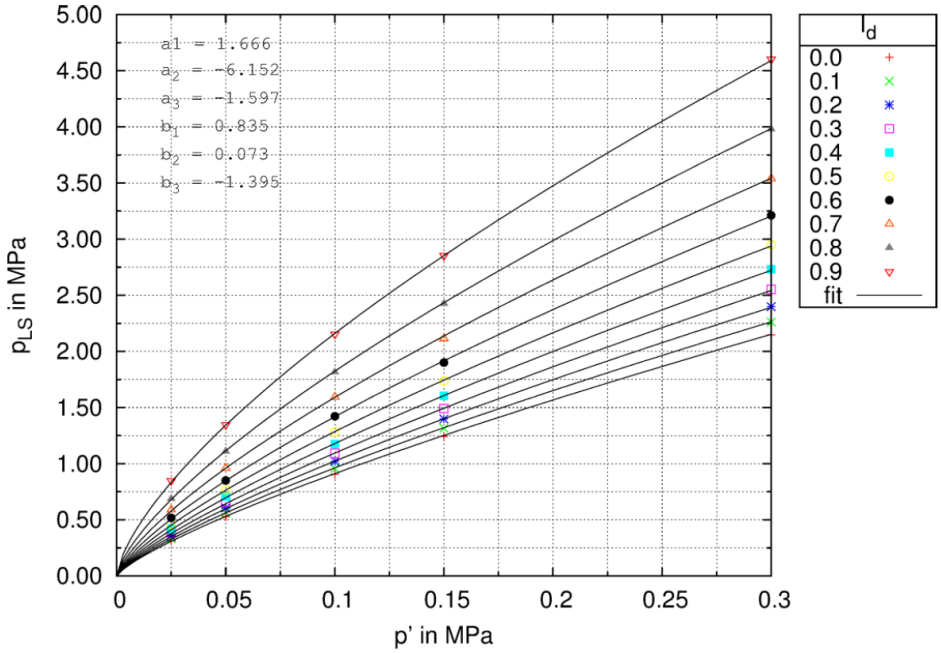

FIGURE D.4: Results of the simulations of the SCE for the sample from box AZ28 [34]

Bibliography

[1] J. Schmertmann, "An Updated Correlation between Relative Density Dr and Fugro-Type Electric Cone Bearing, qc", Contract Report DACW 39-76 M 6646 WES, Wicksburg, Mississippi, Tech. Rep., 1976.

[2] M. Jamiolkowski, D. C. F. Lo Presti, and M. Manassero, "Evaluation of relative density and shear strength of sands from CPT and DMT", *Geotechnical Special Publication*, no. 119, pp. 201–238, 2003.

[3] M. Almeida, M. Jamiolkowski, and R. Peterson, "Preliminary result of CPT tests in calcareous Quiou sand", in *Proceedings of the First International Symposium on Calibration Chamber Testing*, A.-B. Huang, Ed., Potsdam, New York: Elsevier Ltd., pp. 41 –53.

[4] N. Nutt, "Development of the Cone Pressuremeter", PhD thesis, 1993.

[5] R. Cudmani, "Statische, alternierende und dynamische Penetration in nichtbindigen Böden", PhD thesis, Universität Fridericiana in Karlsruhe, 2000.

[6] J. van't Hoff and A. N. van der Kolff, *Hydraulic Fill Manual*. CRC Press, 2013.

[7] M. R. Cohen and H. W. Poiesz, "Forty Years of Maritime Solutions that Changed the World", International Association of Dredging Companies, Tech. Rep. September, 2005.

[8] R. Ramsdell and S. Miedema, "Hydraulic Transport of Sand/Shell Mixtures", *Terra et Aqua*, vol. 122, no. March, 2011.

[9] K. Kirsch and F. Kirsch, *Ground Improvement by Deep Vibratory Methods*. 2010.

[10] "Deep Vibro Techniques - Brochure 10-02E", Keller Grundbau GmbH, Offenbach, Germany, Tech. Rep.

[11] P. Robertson and K. Cabal, *Guide to Cone Penetration Testing for Geotechnical Engineering*, 6th Editio. 2015, p. 143.

[12] P. Robertson, "Soil behaviour type from the CPT: an update", *2nd International Symposium on Cone Penetration Testing*, no. May, 8 p. 2010.

[13] P. W. Mayne, "Cone Penetration Testing: A Synthesis of Highway Practice", Transportation Research Board, Tech. Rep., 2007, p. 126.

[14] T. Lunne, P. K. Robertson, and J. J. M. Powell, *Cone Penetration Testing in Geoteehnical Practice Tom Lunne Peter K . Robertson.* 1997, p. 305.

[15] G. Baldi, R. Bellotti, N. Ghionna, M. Jamiolkowski, and E. Pasqualini, "Interpretation of CPTs and CPTUs, 2nd Part: drained penetration of sands", in *4th International Geo- technical Seminar, Field Instrumentation and In-Situ Measurements*, Singapore, 1986, pp. 143 –155.

[16] T. Meier, "Application of Hypoplastic and Viscohypoplastic Constitutive Models for Geotechnical Problems", PhD thesis, Universität Fridericiana in Karlsruhe, 2007.

[17] R. Salgado, J. K. Mitchell, and M. Jamiolkowski, "Calibration chamber size effects on penetration resistance in sand", *Journal of Geotechnical and Geoenvironmental Engineering*, vol. 124, no. 9, pp. 878–888, 1998.

[18] N. Ghionna and M. Jamiolkowski, "A critical appraisal of calibration chamber testing on sands", in *1st International Symposium on Calibration Chamber Testing*, Clarkson University, Potsdam, USA, 1991.

[19] J. Schmertmann, "The Mechanical Aging of Soils", *Journal of Geotechnical Engineering*, vol. 117, no. 9, 1991.

[20] J. Butlanska, "Cone penetration tests in a virtual calibration chamber", PhD Thesis, Universitat Politècnica de Catalunya BARCELONATECH, 2014.

[21] L. Wesley, "Geotechnical characteristics of a pumice sand", in *Characterisation and Engineering properties of Natural Soils*, T. Tan, K. Phoon, D. Hight, and S. Leroueil, Eds., London: Taylor & Francis, pp. 2449 –2473.

[22] J. Wehr, "Influence of the carbonate content of sand on Vibro Compaction", pp. 0–10,

[23] a. R. Clark and B. F. Walker, "A proposed scheme for the classification and nomemclature for use in the engineering description on Middle Eastern sedimentary rocks", *Géotechnique*, vol. 27, no. 1, pp. 93–99, 1977.

[24] A. C. Meigh, *Cone Penetration Testing.* 2002.

[25] P. A. von Wolffersdorff, "Hypoplastic relation for granular materials with a predefined limit state surface", *Mechanics of Cohesive-Frictional Materials*, vol. 1, no. 3, pp. 251–271, 1996.

[26] D. Kolymbas, "A rate-dependent constitutive equation for soils", *Mechanics Research Communications*, 1977.

[27] A Niemunis and I. Herle, "Hypoplastic model for cohesionless soils with elastic strain range", *Mechanics of Cohesive-frictional Materials*, vol. 2, no. 4, pp. 279–299, 1997.

[28] D. Mašín, "A hypoplastic constitutive model for clays", *International Journal for Numerical and Analytical Methods in Geomechanics*, vol. 29, no. 4, pp. 311–336, 2005.

[29] I. Herle, "Hypoplastizität und Granulometrie einfacher Korngerüste", *Veröffentlichungen des Institutes für Bodenmechanik und Felsmechaink der Universität Fridericiana in Karlsruhe*, vol. 142, p. 123, 1997.

[30] E. Bauer, "Calibration of a Comprehensive Hypoplastic Model for Granular Materials.", *Soils and Foundations*, vol. 36, no. 1, pp. 13–26, 1996.

[31] I. Herle and G. Gudehus, "Determination of parameters of a hypoplastic constitutive model from properties of grain assemblies", *Mechanics of Cohesive-frictional Materials*, vol. 4, no. 5, pp. 461–486, 1999.

[32] I. Herle, "Granulometric Limits of Hypoplastic Models", *TASK Quarterly: scientific bulletin of the Academic Computer Centre in Gdansk*, vol. 4, no. 3, pp. 389–408, 2000.

[33] B. O. Hardin, "Crushing of Soil Particles", *Journal of Geotechnical Engineering*, vol. 111, no. 10, 1985.

[34] T. Meier and S. T. Meybodi, "Report on Experimental and Numerical Investigations to Determine Parameters for the Karslruhe CPT Interpretation Method", Baugrund Dresden, Dresden, Germany, Tech. Rep., 2017.

[35] D. Mašín, "Hypoplasticity for Practical Applications", Tech. Rep., 2015.

[36] R. F. Bishop, R. Hill, and N. F. Mott, "The theory of indentation and hardness tests", *Proceedings of the Physical Society*, 1945.

[37] R. E. Gibson and W. F. Anderson, "In-situ measurement of soil properties with pressuremeter", *Civil Engineering (London)*, 1961.

[38] R. Salgado, J. K. Mitchell, and M. Jamiolkowski, "Cavity Expansion and Penetration Resistance in Sand", *Journal of Geotechnical and Geoenvironmental Engineering*, vol. 123, no. 4, pp. 382–388, 1997.

[39] H. S. Yu, *Cavity Expansion Methods in Geomechanics*. Dordrecht, Netherlands: Springer Netherlands, 2000.

[40] R. Cudmani and V. A. Osinov, "The cavity expansion problem for the interpretation of cone penetration and pressuremeter tests", *Canadian Geotechnical Journal*, vol. 38, no. 3, pp. 622–638, 2001.

[41] M. Uhlig and I. Herle, "Aktuelle Forschung in der Bodenmechanik 2015, Kapitel 5, Bestimmung der Porenzahl aus Drucksondierungen", in *Aktuelle Forschung in der Bodenmechanik 2015*, 2015, pp. 85 –100. arXiv: 1011.1669.

[42] V. A. Osinov and R. Cudmani, "Theoretical investigation of the cavity expansion problem based on a hypoplasticity model", *International Journal for Numerical and Analytical Methods in Geomechanics*, vol. 25, no. 5, pp. 473–495, 2001.

[43] F. Tavenas and P. La Rochelle, "Accuracy of the relative density measurements", *Géotechnique*, vol. 22, no. 4, pp. 549–562, 1972.

[44] M. Jefferies and K. Been, "Cone factors in sand", in *The International Symposium on Cone Penetration Testing*, Linköping, Sweden, 1995, pp. 187 –193.

[45] J. Jaky, "Pressure in silos", in *2nd International Conference on Soil Mechanics and Foundation Engineering*, 1948, pp. 103 –107.

[46] Projects Link Contracting CO. L.L.C, "Technical Note – Verification Of Ground Improvement Works", Tech. Rep., 2017.

[47] P. Menge, K. Vinck, M. Van Den Broeck, P. O. Van Impe, and W. F. Van Impe, "Evaluation of relative density and liquefaction potential with CPT in reclaimed calcareous sand", in *Geotechnical and Geophysical Site Characterisation 5*, 2016.

[48] C. Boley, *Handbuch Geotechnik*, 1. Auflage, C. Boley, Ed. Wiesbaden: Vieweg+Teubner Verlag, 2012.

[49] B. Hamidi, H. Nikraz, and S. Varaksin, "Relative density concept is not a reliable criterion", *Proceedings of the ICE - Ground Improvement*, vol. 166, no. 2, pp. 78–85, 2013.

[50] F. Tavenas and P. La Rochelle, "Accuracy of relative density measurements", *Géotechnique*, vol. 22, no. 4, pp. 549–562, 1972.

[51] H. Engin and H. Jostad, "On the modelling of grain crushing in hypoplasticity", in *Numerical Methods in Geotechnical Engineering*, 1996, M. Hicks, B. Brinkgreve, and A. Rohe, Eds., London: Taylor & Francis Group, 2014, pp. 33–38.

[52] P. O. Van Impe, W. F. Van Impe, A. Manzotti, and S. Marchetti, "Compaction control of land reclamations with calcareous sands. Some case studies.", *Geotechnical Conference Torino*, 2016.